Titre: Title:	Low velocity impact damage in carbon fiber/peek composite laminates
Auteur: Author:	Hao Wang
Date:	1993
Type:	Mémoire ou thèse / Dissertation or Thesis
Référence: Citation:	Wang, H. (1993). Low velocity impact damage in carbon fiber/peek composite laminates [Thèse de doctorat, Polytechnique Montréal]. PolyPublie. https://publications.polymtl.ca/57986/

UNIVERSITÉ DE MONTRÉAL

LOW VELOCITY IMPACT DAMAGE IN CARBON FIBER/PEEK COMPOSITE LAMINATES

par

Hao WANG

DÉPARTEMENT DE GÉNIE MÉCANIQUE

ÉCOLE POLYTECHNIQUE

THÈSE PRÉSENTÉE EN VUE DE L'OBTENTION

DU GRADE DE PHILOSOPHIAE DOCTOR (Ph.D.)

(GÉNIE MÉCANIQUE)

Mars 1993

ISBN 0-315-86546-6

UNIVERSITÉ DE MONTRÉAL

ÉCOLE POLYTECHNIQUE

Cette thèse intitulée:

LOW VELOCITY IMPACT DAMAGE IN CARBON FIBER/PEEK COMPOSITE LAMINATES

Présentée par: Hao WANG

en vue de l'obtention du grade de Philosopiae Doctor (Ph.D.)

a été dûment acceptée par le jury d'examen constitué de:

Mme. BERNARD, Marie , Ph.D., présidente

M. VU-KHANH, Toan , Ph.D., membre et directeur de recherche

M. GAUVIN, Raymond, Ph.D., membre

M. HOA, Suong V. , Ph.D., membre

Sommaire

Les stratifiés ou laminés en composites haute performance sont de plus en plus employés dans les structures en aéronautique en raison de leur attirante rigidité ou résistance par unité de poids. Toutefois, ces matériaux sont très sensibles à l'endommagement sous choc. Lorsque l'impact est de faible vitesse, les dommages sont essentiellement du type fissuration transversale et délaminage. Ces modes de dommage étant internes, ils ne peuvent être détectés par un simple examen visuel de la surface; ils peuvent cependant détériorer de façon significative la performance de la structure. Par conséquent l'étude de l'endommagement sous choc à faibles vitesses est très importante pour les applications des matériaux composites.

De nombreux chercheurs se sont efforcés à prédire le rapport entre la force de l'impact et l'importance des dommages créés. A l'heure actuelle, les méthodes de prédiction sont basées sur la théorie de la résistance des matériaux. La méthode classique consiste à calculer les contraintes dynamiques dans un stratifié en parfait état, l'importance des dommages étant évaluée en fonction de certains critères de défaillance sous contraintes. Or, lorsqu'on tient compte de l'aspect physique de la question, on doit reconnaître que la démarche est fort discutable puisque le champ de contraintes est redistribué dès la première phase de l'endommagement et il ne peut servir à prévoir la propagation des dommages. Actuellement, on ne connaît pas réellement les paramètres mécaniques ni les propriétés des matériaux qui déterminent l'ampleur des dommages subis sous un choc donné.

Cette thèse présente les recherches aussi bien expérimentales qu'analytiques sur les dommages subis par un composite thermoplastique PEEK/carbone (fibre de carbone/polyétherétherkétone) sous des chocs à faible vitesse. L'étude porte essentiellement sur les paramètres mécaniques et les propriétés du matériau susceptibles de gouverner l'ampleur du délaminage et de la fissuration transversale pour les stratifiés soumis aux chocs. On a évalué la démarche axée sur la résistance des matériaux afin de voir dans quelle mesure on pourrait l'appliquer pour prédire l'importance des dommages. Une méthode faisant appel à la mécanique de rupture a été proposée dans le but de caractériser le délaminage causé par l'impact. On a également étudié les influences des contraintes thermiques résiduelles, de la résistance des plis *in situ* et de la ténacité à la rupture interlaminaire du composite thermoplastique.

Dans le but de caractériser l'endommagement du composite PEEK/carbone, trois types de stratifié croisé (stratifiés à couches croisées dits "crossply"); $[0_5/90_5/0_5]$, $[0_3/90_3/0_3/90_3/0_3]$ et $[0/90, ..., 90/0]_{15t}$, ont été soumis aux essais de choc à poids tombant. Les éprouvettes sont des plaques carrées de dimension 152 mm x 152 mm. Encastrées aux quatre côtés, elles ont été alors soumises aux essais d'impact à des niveaux d'énergie allant de 1 à 20 joules. L'enregistrement de la force d'impact a été effectuée à l'aide d'un appareil de choc instrumenté. Les dommages subis par les plaques ont été examinés d'abord à l'oeil nu ensuite par un procédé de radiographie (rayons X) avec pénétrant opaque et finalement par une technique thermique de séparation des plis individuels du stratifié.

Il a été trouvé que le thermoplastique présente les mêmes modes d'endommagement que les composites époxy thermodurcissables. En particulier, le délaminage et la fissuration transversale prédominent dans le cas des stratifiés $[0_5/90_5/0_5]$ et $[0_3/90_3/0_3/90_3/0_3]$, tandis que pour le stratifié $[0/90,..., 90/0]_{15t}$, la

pénétration a lieu, due à la rupture des fibres. Le composite PEEK/carbone s'avère supérieur aux composites Kevlar/époxy et graphite/ époxy pour ce qui est de la résistance au délaminage par impact.

En ce qui concerne le délaminage, la surface de fracture a été observée à l'oeil nu ainsi qu'à l'aide d'un microscope électronique à balayage (MEB). Il a été observé que le délaminage est initié à partir des fissurations transversales dans la couche située au-dessus de l'interface, pour se propager, le long de la fibre du pli, en dessous de l'interface. L'aspect de la surface de rupture indique que le délaminage résulte d'un processus de rupture instable, essentiellement en Mode II.

Pour évaluer l'action des contraintes thermiques résiduelles, on a également mesuré la résistance *in situ* des plis dans les stratifiés croisés. Une méthode combinant l'essai de défaillance de la première couche (dit "first-ply failure test") et une analyse incrémentale du stratifié a été proposée. L'analyse tient compte des variations des propriétés du matériau, en dessous et au dessus de la température de transition vitreuse du composite. Il a été constaté que les contraintes résiduelles dans les stratifiés peuvent atteindre la moitié de la résistance transversale du composite unidirectionnel.

D'autre part, la résistance *in situ* dépend de l'épaisseur du pli. Pour une épaisseur modeste, la présence des plis adjacents accroît considérablement la résistance du pli individuel, qui devient nettement supérieure à celle du composite unidirectionnel.

A partir des données expérimentales, la méthode basée sur la résistance des matériaux pour la prévision des dommages causés par un impact a été vérifiée. Les contraintes dynamiques ont été calculées par la méthode des éléments finis; la fissuration transversale a été définie par un critère de rupture d'Harshin modifié, tenant compte des contraintes résiduelles et de l'effet de restriction de la fissuration par des plis adjacents. Il apparaît que la méthode basée sur la résistance des matériaux ne permet de prévoir

l'importance des fissurations. Cependant, il y a une corrélation qualitative entre les contours du champ de contraintes de cisaillement interlaminaire et la géométrie du délaminage.

Les observations expérimentales suggèrent que l'approche fondée sur la mécanique de rupture permet de prédire l'ampleur du délaminage. Selon un concept de la ténacité à l'arrêt de la fissuration, un critère d'arrêt du délaminage est proposé dans la présente étude: le délaminage prend fin lorsque le taux de restitution de l'énergie présente la même valeur que la ténacité à l'arrêt de la fissuration.

Pour la vérification du critère l'analyse du comportement au délaminage des stratifiés $[0_5/90_5/0_5]$ et $[0_3/90_3/0_3/90_3/0_3]$ a été effectuée. Le taux de restitution de l'énergie de déformation a été calculé selon la méthode énergétique de la mécanique de rupture, utilisant la méthode des éléments finis pour simuler le délaminage et la fissuration transversale dans les stratifiés. Comme la vitesse de propagation est, dans le cas de la fracture instable, bien supérieure à la vitesse de l'impact, la fracture a lieu sous une condition de déflexion contrôlée. La déflexion des plaques à l'arrêt du délaminage a été extrapolée à partir des mesures de charge et de déflexion fournies par l'appareil de choc instrumenté.

Les résultats de l'analyse effectuée selon les principes de la mécanique de rupture démontrent que le taux de restitution de l'énergie de déformation peut être considéré comme le paramètre contrôlant le délaminage causé par un impact. Lorsque le délaminage est amorcé à une énergie de choc critique, le taux de restitution augmente d'abord et ensuite décroît avec la propagation du délaminage; on est donc en présence d'un processus de propagation instable, qui sera suivi d'un arrêt de la fissure.

Lorsque la force de l'impact est plus élevée, ce processus croissance/arrêt peut être répété de manière à engendrer une progression du délaminage en plusieurs étapes.

On constate qu'il y a concordance entre le mécanisme de rupture et les observations de l'expérience. Les résultats démontrent que l'ampleur du délaminage est régi par un critère d'arrêt de fissure. Dans les deux stratifiés étudiés, le délaminage semble s'arrêter à une énergie constante de rupture interlaminaire qui est indépendant de la taille du délaminage. Il est donc possible de prédire de manière raisonnable l'ampleur du délaminage de ces stratifiés, en utilisant la démarche basée sur le taux de restitution de l'énergie et la ténacité à l'arrêt de la fissuration.

Le critère d'arrêt semble constituer une approche fort prometteuse pour ce qui est de la prédiction du délaminage causé par des impacts. Toutefois, un programme important de recherche devra encore être entrepris avant que cette démarche puisse être généralisée à des applications pratiques. Le critère d'arrêt doit être essayé sur divers types de stratifiés et systèmes de matériaux. Il faut également mettre au point des méthodes d'essai plus simples permettant de mesurer la ténacité à l'arrêt de la fissuration. (Au cours de cette étude, on s'est efforcé de mesurer la ténacité en Mode II du composite PEEK/carbone, à l'aide d'un essai de rupture ELS (c.-à-d. "End-Loaded Split"). La méthode d'essai a été optimisée pour inclure l'effet d'une large déflexion. Cependant, on devrait également mettre au point des méthodes permettant de calculer, de manière simple et efficace, le taux de restitution de l'énergie de déformation dans des stratifiés soumis à un impact.

Abstract

This dissertation presents both experimental and analytical investigations on the low velocity impact damage in Carbon Fiber/Polyetheretherketone (PEEK/Carbon) thermoplastic composite. Emphases of the study were focused on the material properties that may control the extension of impact-induced delamination and transverse crack. The Strength of Materials approach to predict the damage extension was evaluated by a dynamic finite element analysis. A fracture mechanics approach is proposed to characterize the crack growth behavior of impact-induced delamination. Prediction of the delamination size is discussed using the concept of crack arrest toughness.

In the crossply laminates studied, it has been found that the thermoplastic material exhibits the same damage modes as that observed in thermoset epoxy composites. Considering the thermal residual stress and the crack constraining mechanism, extension of transverse cracks could not be predicted by the Strength of Materials approach. On the other hand, the impact-induced delamination results from a Mode II dominated unstable fracture and also cannot be described by a Strength of Materials criterion. The delamination occurs under a displacement controlled condition and seems to be arrested at a constant interlaminar fracture energy. The strain energy release rate and delamination arrest toughness of the material control the delamination extension.

In addition, the end-loaded-split (ELS) fracture test was conducted to measure

the Mode II delamination toughness of PEEK/Carbon composite. Large deflection effect on toughness measurement was studied by nonlinear beam theory. Using this test to measure the Mode II crack arrest toughness of the material is also discussed.

Acknowledgment

I would like to express my sincere gratitude to my research advisor Dr. Toan Vu-Khanh for his guidance, suggestions, encouragement, and continuous support from the inception to the present form of this Thesis.

I thank Dr. Raymond Gauvin for his help at the beginning of my study at Ecole Polytechnique. I also thank Dr. Marie Bernard and Dr. Suong V. Hoa for serving on my committee.

Many thanks go to the Industrial Materials Institute (IMI), National Research Council of Canada, for accepting me as a visiting research assistant and allowing me to use the facilities at IMI to carry out this work. The technical assistance from Mr. Jacques Dufour and the other technicians in the Industrial Polymers Group is gratefully appreciated. Thanks also extend to Miss Isabelle Paris for her assistance in preparing part of the test specimens and in obtaining Figure 5.6.

I am also indebted to Prof S. F. Sun for his help and encouragement.

The financial support from CRIM is gratefully acknowledged.

I thank my mother and father, and especially my wife. Without their love, understanding and full support over the years, I could not have completed this work.

Table of Contents

List of Figures

List of Tables

List of Appendix

Nomenclature

a	crack length
A	delamination area
α, φ	angle of slope of a deflected beam
α_L, α_T	thermal expansion coefficients
b	width of a beam
C	compliance
D	width of a transverse crack area
δ	deflection
E_L, E_T	Young's moduli of a lamina
E_f	flexural modulus of a beam
$\{\varepsilon\}$	strain vector
$\{\varepsilon^0\}$	midplane strain vector
F_P, F_δ	large deflection correction factors
G	strain energy release rate
G_{cr}	fracture initiation toughness
G_{arr}	crack arrest toughness
G_{LT}	shear modulus of a lamina
h	thickness of a beam or a plate
H	length of a transverse crack area

I	inertia moment of a cross section
I, II, III	fracture modes
$\{k\}$	curvature of a laminate
L	delamination length, or length of a beam
l	half length of a delamination, or horizontal distance from load line to crack tip in a cracked beam specimen
M	bending moment
ν_{LT}	Poisson's ratio
P	load
$[Q]$	lamina stiffness matrix
θ_x, θ_y	angles of rotation
R	radius of curvature
R_m	strength ratio of transverse matrix failure
ρ	mass density
S	curvilinear coordinate
$\{\sigma\}$	in-plane stress vector
σ_T	transverse strength
T	temperature
T_g	glass transition temperature
τ_{xz}, τ_{yz}	interlaminar shear stress components
τ_{LT}, τ_T	shear strengths
U	strain energy
u, v, w	displacements
W	width of a delamination
x, y, z	Cartesian coordinates

Chapter 1

Introduction

Laminated composites made of advanced fiber reinforced plastics, such as the graphite fiber reinforced epoxy or PEEK (polyetheretherketone) matrices, have been increasingly used in aircraft structures (1, 2). The major advantages of these materials are the high stiffness- and strength-to-weight ratios, which offer significant weight-saving potentials for building lighter and more efficient aircraft. The materials also exhibit improved fatigue properties, better corrosion resistance and, as important, an easier formability (2).

However, application of composites to the load-bearing aircraft components such as the fuselage and wing structures is still very limited. The strain allowable used in the present design is about 0.4% (2), considerably lower than the strain to failure of about 1.5% of some new fiber systems (2). The conservative design level significantly limits the efficient use of composite materials (3). Among the many causes for the situation, it is generally believed that the structural degradation due to impact damage is one of the most critical design limitations (1-5).

During manufacturing and in service, aircraft components are subjected to a wide variety of accidental impact by foreign objects (5). Typical examples include the dropped tools, runway debris, small arm fires, etc. Due to the lack of through-the-

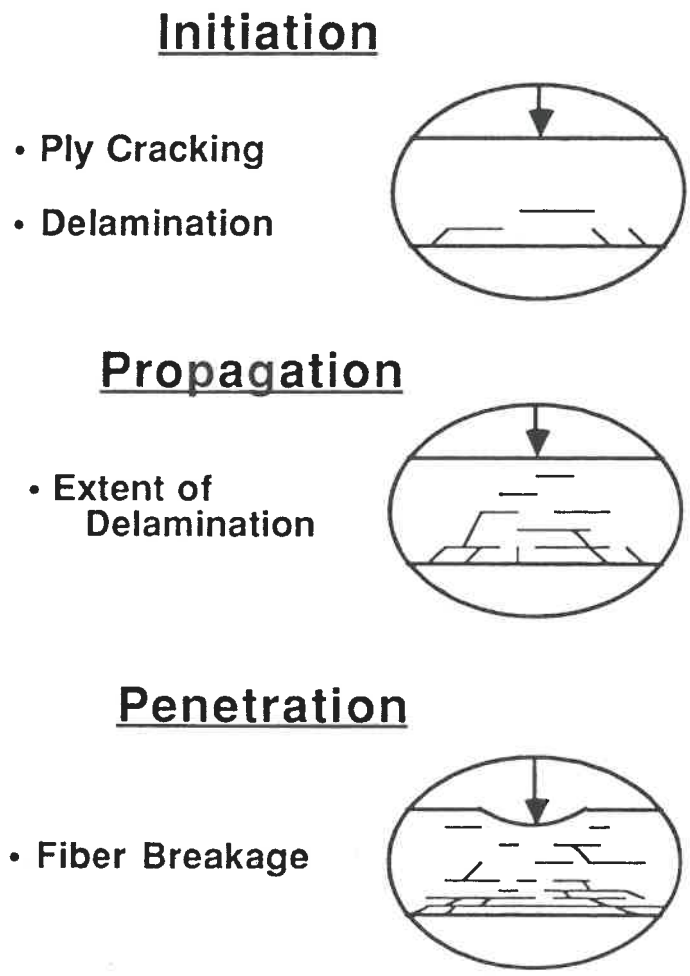

Figure 1.1 A typical damage process in composite laminates under transverse impact.

thickness reinforcement, the laminated structures are very susceptible to damage under the impact load. Fig. 1.1 illustrates the typical damage process during impact (4). The major damage modes include the transverse crack, delamination and fiber breakage. The integrated damage state can be very complex and generally depends on the type of impact and the material considered.

Among the various impact events and the damages produced, the potentially most dangerous case is perhaps the subpenetration damage caused by a low velocity and low energy impact (5). This is because the impact event has a high probability of occurrence in practice, and the damage may degrade the laminate performance without being detected. The damage consists mainly of the matrix-controlled failure modes (i.e. the transverse crack and delamination). It may be quite extensive in the laminate but, in many cases, the only indication at the impacted surface is a small dent that is hard to detect by naked eyes. Such a damage is often referred to as the "barely visible impact damage", the BVID in short (5). In practice, nondestructive inspection (NDI) techniques such as the C-scan are used for detecting the BVID. However, the routine NDI is often limited to the damage-prone components, and frequent NDI is time-consuming and expensive (5). A small delamination that escapes the inspection may grow into a critical size under cyclic loading conditions (6).

In spite of less fiber breakage than penetrated damage, the BVID can be very detrimental to the structure in terms of reduced stiffness, strength and fatigue life (2). A typical case is the compression-after-impact (CAI) behavior (7, 8). Fig. 1.2a shows a CAI test on the $[0_2/90_2/\pm45_2]_s$ Graphite/Bismaleimide laminates (8). Damage in the laminate is the BVID type, and extensive delaminations have been detected by penetrant-enhanced X-radiography. Under compression, the delaminated plies may buckle to cause a Mode I dominated fracture (9) (Fig. 1.2b). Due to the low Mode I

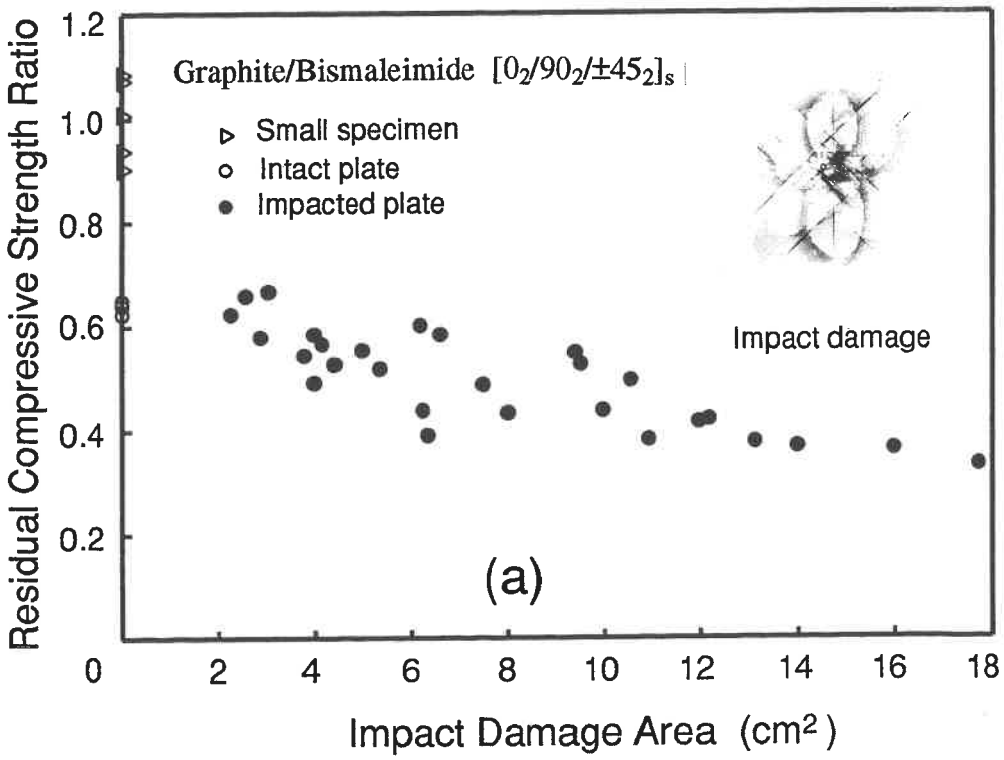

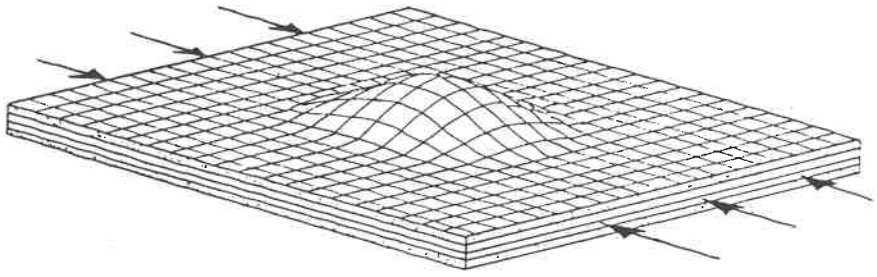

(b)

Figure 1.2 Effect of impact damage on compressive strength of composite laminates: (a) compression-after-impact test [8]; (b) local buckling of delaminated plies under compressive load [9].

toughness of the composite (8), the fracture occurs at a reduced load, which may be only 60% of the compressive strength of the damage-free laminate. Similar observations have also been reported in many other studies as summarized in (5). Consequently, the study of low-velocity impact damage, especially the impact-induced delamination, is of critical importance to the damage tolerance design and in-service maintenance of composite aircraft structures.

Since the 1970's, extensive research works have been devoted to studying the low velocity impact damage in laminated composites (10, 11). Most of the studies are by testing. It is found that the damage generally depends on the structural response and the material behavior under impact. Many test parameters may significantly affect the damage behavior. As summarized in (11), these include the test method, fiber/matrix selection, laminate stacking sequence, specimen geometry, the nose shape and velocity of the impactor, etc. It appears that large and costly efforts would be required to cover the various combinations of the test parameters (12). Therefore, the current interest in the field is to model the damage by analytical or numerical means (12-25), by which effects of the above parameters could be readily considered.

One of the objectives in modeling impact damage is to predict the damage extent that an impact event can produce in a given laminate (16-25). The prerequisite for achieving this objective is to understand what mechanics parameters and material properties actually control the damage extension during impact. Due to the extremely complex damage process, the present knowledge in these aspects is still not clear. For example, the dynamic stresses in damage-free laminates have been considered to characterize the damage size (16-21). However, such stresses should have been redistributed at onset of the progressive damage process.

This dissertation studies the damage growth mechanisms in Carbon Fiber

/Polyetheretherketone (PEEK/Carbon) composite under low velocity impact. Ten chapters and two appendices are included in this dissertation. Chapter 2 consists of two parts which review respectively the experimental studies and modeling of impact damage. Chapter 3 explains the research program. A preliminary study on measuring the thermal residual stress and *in situ* lamina strength of PEEK/Carbon composite is presented in Chapter 4. Experimental characterization of impact damage behavior in the material is reported in Chapter 5. Chapter 6 evaluates the Strength of Materials approach for predicting the damage extension. In Chapter 7, the crack growth mechanism of impact-induced delamination is studied by fracture mechanics approach. Chapter 8 deals with the measurement of Mode II delamination toughness of the composite. Chapter 9 presents the summary and conclusions of this dissertation. Some recommendations for further research are included in Chapter 10. In Appendix A, the end-loaded-split (ELS) fracture test is analyzed by nonlinear beam theory. Large deflection correction factors for measuring the Mode II delamination toughness are given in Appendix B.

Chapter 2

Literature Review

2.1 Experimental Studies on Impact Damage

2.1.1 Low Velocity Impact Response

As discussed in (26), a low velocity impact refers to the impact event in which the dynamic effect on target response is insignificant. In other words, the structural response is dominated by quasi-static response. Typical examples in practice include the structure being impacted by dropped tools or ground service vehicles. The impact velocity ranges from the order of cm/s to that of tens of m/s, depending on the mass, stiffness and end support of the structure. The type of impactor should also be considered (26). The low velocity impact condition is often simulated by swaying pendulum or drop weight impact tests (11, 26). Comparison studies by test (26-29) and analysis (30) have shown that the sample response to drop weight impact is close to that in an equivalent static indentation case.

Impact damage in laminated composites depends on both the structural response and the material behavior under impact. Under a transverse impact load, the laminate undergoes the combination of a local contact deformation near the impact site

and a global bending deformation in the far-field region (12-14, 18). Such deformations produce a complex and non-uniform stress field in the laminate because of the inhomogenous and anisotropic material properties (12-14, 18). Advanced composites are generally considered as brittle materials because plastic deformation is significantly limited by the fiber reinforcement (11). Therefore the material responds to impact load in terms of elastic deformation and multiple failures in its constituents. The major damage modes, as shown in Fig. 1.1, include the transverse crack, delamination and fiber breakage. The matrix-controlled damage modes, the transverse crack and delamination, typically occur under low velocity impact load because low fracture energies are involved in such damages (11). In addition, the fracture energies may further decrease at the loading rate due to impact (see Section 2.3), so an extensive damage may result from a low impact energy.

Fiber breakage may also occur under low velocity impact if a large energy or a sharp impactor is used (31). However, fiber breakage is the controlling damage mode in penetration failure, which is mostly concerned under high velocity impact conditions (32-34). For the reasons discussed in Chapter 1, the matrix-controlled damage modes, particularly the impact-induced delamination, will be the major concerns of the present study.

2.1.2 Transverse Crack

Transverse cracking is the matrix fracture within a layer to form a crack (or a group of cracks) along the fiber direction of the layer. The transverse crack is a secondary damage mode in terms of the small energy absorption during impact and its

effect on structural performance. Nevertheless, it plays an important role in the damage process. It may initiate delamination and fiber breakage, and it interacts with the delamination growth.

Takeda, et al (35) used a velocity gage made of a silver paint on the laminate surface to measure the transverse crack velocity during impact. The association of transverse cracking with flexural waves was also studied by the authors using surface and embedded strain gage technique (36). Test results indicate that transverse cracks are the initial damage mode during impact (37, 38).

The effects of transverse cracks in initiating other damage modes have been revealed by microscopic examination of the cross section of impacted laminates (13, 39-41). Fig. 2.1 shows the fracture patterns in a $[0_5/90_5/0_5]$ Graphite/Epoxy laminate at the impact site (13). The delamination at each interface seems to be initiated from a few transverse cracks in the layer above the interface. These cracks are inclined with an angle to the interface and located near, but a certain distance away from, the impact center. Stress analysis (13) showed that such cracks are produced by the transverse shear stress concentration below the edge of contact area. They are therefore defined as the transverse shear cracks (13). When the shear crack propagates up to the interface, a stress concentration occurs at the crack tip (14) (Fig. 2.2). The increased interlaminar stresses are responsible for initiating the delamination. The stress concentration also exists in the adjacent layer around the crack tip. In testing composites with a tough interface (40, 41), the stress concentration may cause fiber breakage in the layer instead of delamination at the interface. The damage initiation mechanisms have also been observed in laminates with complex stacking sequences (38, 41).

Away from the impact site, another set of cracks may extend over a large area (13, 29, 42). These cracks are defined as the transverse bending cracks because they

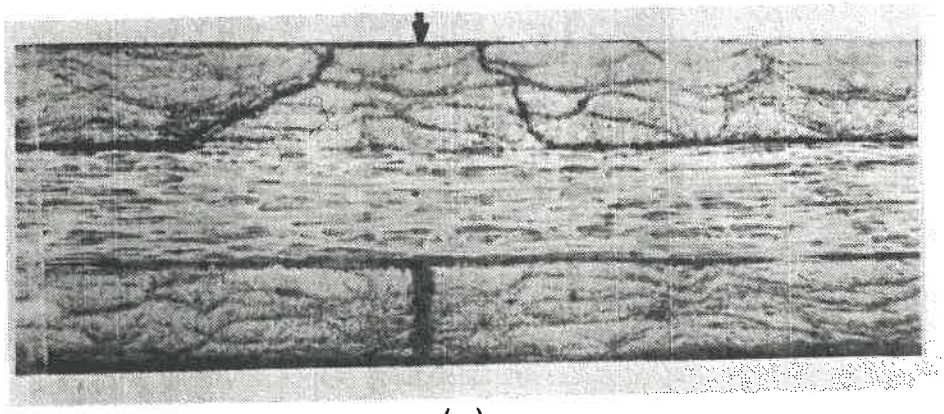

(a)

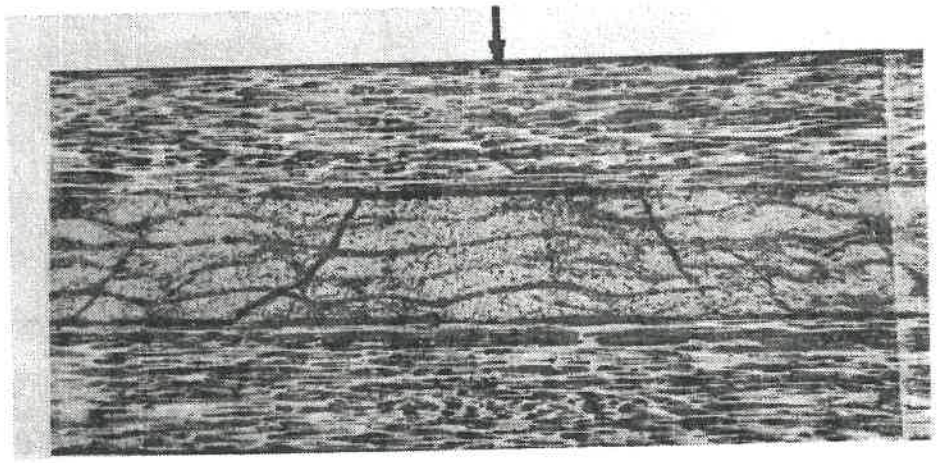

(b)

Figure 2.1 Transverse cracks in [$0_5/90_5/0_5$] Graphite/Epoxy laminates near the impact site: (a) cracks in the 0-degree plies; (b) cracks in the 90-degree ply [13].

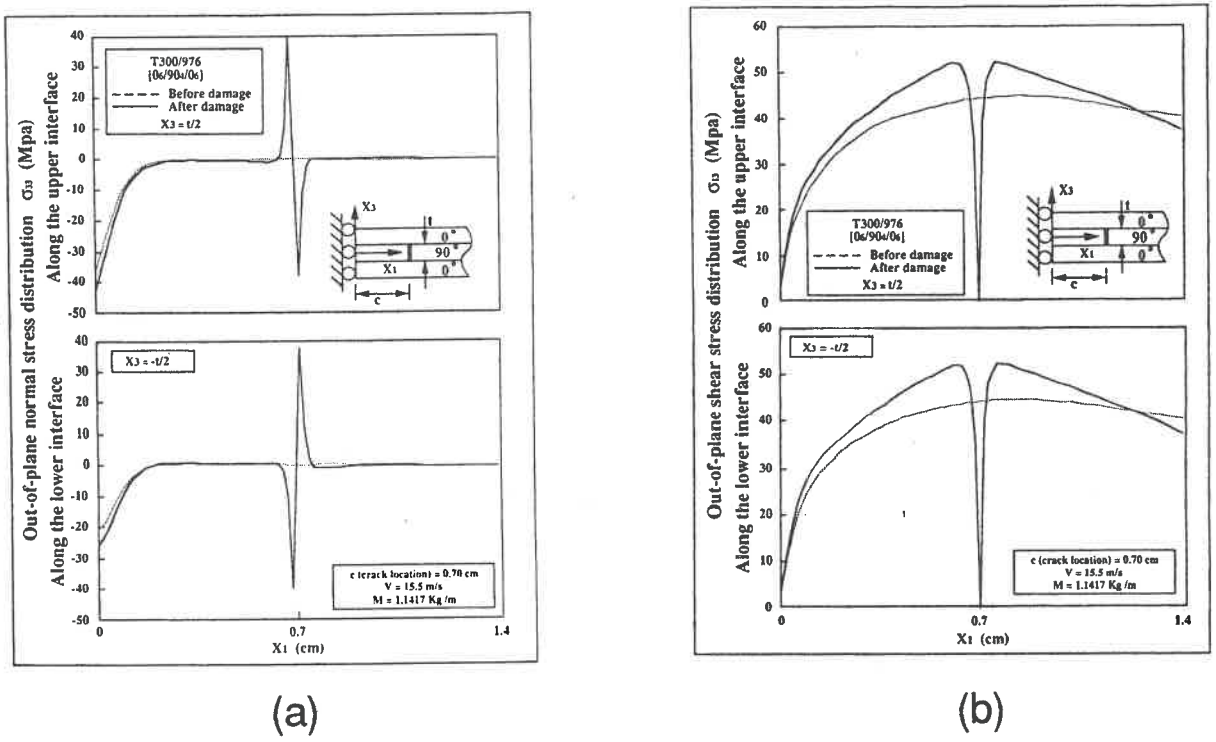

Figure 2.2 Interlaminar stresses in $[0_6/90_2]_s$ Graphite/Epoxy laminate before and after transverse cracking in the 90-degree ply :
(a) out-of-plane normal stress; (b) interlaminar shear stress [14].

are produced by the flexural stresses during plate deflection (13). The bending cracks are perpendicular to the interface and almost evenly distributed in the layer (29, 42). The crack pattern implies a similar failure mechanism to that in the off-axis ply of a laminate coupon under tensile load (43). It is found that the crack density increases with impact velocity (42). And the crack distribution exhibits a close association with the propagation of flexural waves during impact (29). Interactions between the transverse crack and delamination are also observed (29).

2.1.3 Delamination

Impact-induced delamination appears as the planar crack embedding at the interface between two layers of different fiber orientations. Since the delamination is potentially detrimental to laminate performance, its fracture mechanism has been the topic of extensive studies (2). Most of the studies are by testing. The laminate is impacted at a certain energy and is inspected to determine the size and location of delaminations in the plate. The test apparatus include the pendulum and drop weight impact machines and the air-gun test setup (11). The damage inspection methods, such as the C-Scan (2), X-radiography (6), edge replication (13) and the thermal deplying technique (44), are very effective in detecting the delamination. Many important features of the delamination have been observed.

As discussed in the previous section, the delamination is initiated from the transverse shear cracks in the layer above the interface. It then propagates along the fiber direction of the layer below the interface (45-47). Therefore the delamination area depends in some way on the two fiber directions below and above the interface. At the

interface between perpendicular fiber directions (e.g. at the 0/90 or +45/-45 interfaces), the delamination is a symmetric "peanut shape" area. Otherwise, it has a distorted "peanut shape" and may not be symmetric. At the same impact conditions, the delamination area seems to increase with the difference between the two fiber orientations (47). The delamination area also increases with the thickness of the adjacent plies (48, 49).

Through the plate thickness, the delamination area distributes in a growing sequence in the impact direction. The largest delamination tends to occur at the last interface from the impacted surface. The total delamination area, which is the summation of the delamination at each interface, varies approximately linearly with impact energy (47-49).

High speed photography has been used to study the delamination process during impact (35, 50, 51). Takeda, et al (35) recorded the damage development in $[0_5/90_5/0_5]$ Glass/Epoxy laminate under projectile impact. It was found that the delamination is a dynamic fracture process with crack initiation at a high velocity (200-500 m/s), followed by a decrease in crack velocity, and then by crack arrest. The fracture behavior also depends on the interface position with respect to the impacted surface. The delaminations at the first interface (near the impacted surface) was initiated almost simultaneously as the second interface delamination, but it propagated somewhat slower and stopped earlier. The second interface delamination was arrested at or within half of the contact duration. The unstable crack growth was little affected by the impactor types and the impact velocities considered (35).

In another work (50), the delamination growth in pre-cracked Graphite/Epoxy beams under projectile impact was studied. The crack growth also occurred at high velocities and seemed to be associated with the propagation of flexural waves. Again,

the delamination position in the thickness direction was found to affect the crack growth mechanism. The midplane delamination experiences a primarily Mode II fracture. While for the off-midplane delamination, when the near-surface delaminated region is under flexural compressive stress during the beam vibration, the delaminated plies may buckle locally and cause a Mode I dominated extension of the delamination.

Unstable delamination growth has also been observed in swaying pendulum and drop weight impact tests (21, 26, 27). The delamination does not occur until a critical energy level is reached, at which the delamination is suddenly initiated and pops into a definite size. Such a fracture behavior has been observed in both thermoset and thermoplastic composites. It is also observed in the delamination caused by static indentation load (26, 27).

2.2 Modeling Impact Damage

2.2.1 Damage Prediction

Experimental studies provide physical insight into the damage process. Empirical relations between damage extent and impact level may also be established from the test data. But such relations are limited to the test condition determined by numerous test parameters (11). In order to characterize the damage for design purposes, there exists a need for the approach by which the damage could be predicted by analysis.

Test observations show that the damage is initiated at a critical impact level, above which the damage extends to a definite size depending on the level of impact.

Therefore, from the viewpoint of damage resistance design, predicting the damage initiation determines the threshold energy that the structure can withstand without incurring damage. While the damage tolerance design may require predictions of the damage type and extent that a given impact can produce in the laminate. In the case of low velocity impact, the predictions concerning impact-induced delamination are of primary importance.

2.2.2 Damage Initiation

In principle, damage initiation may be predicted by the Strength of Materials approach (12). The approach consists of studying the impact stress field in intact laminate and applying a stress (or strain) failure criterion. It is important to identify the initial failure mode and the stress (strain) components that control the failure. The material strength related to the failure should also be determined. In low velocity impact on relatively thin laminates, transverse crack is the first damage mode. Consequently, onset of transverse cracking defines the threshold impact level below which no damage would occur.

The stresses in laminates under transverse impact may be studied using the global/local approach (18). The dynamic flexural response of the laminate is studied in the global analysis, in which the local contact deformation is simulated by a nonlinear spring at the impact point (14-18, 52). The spring obeys the contact law which relates the impact force to the depth of indentation (52, 53). The impact force history and laminate flexural deformation can be calculated in terms of the impact parameters and laminate properties. Subsequently, in the local analysis, the contact stress field is

calculated from the impact force using the classical Herzian approach (12, 13, 18, 53).

Grezuzczuk (12) studied the impact stresses and failure modes in a half-space made of quasi-isotropic composite. The analysis seems to be applicable to very thick laminates (28). For thin laminates, Joshi and Sun (13) reported a two-dimensional finite element analysis of $[0_5/90_5/0_5]$ and $[90_5/0_5/90_5]$ laminate beams under projectile impact. Numerical results showed that the stress field approximately consists of two parts: the local contact stresses under the impactor and the plate bending stresses outside of the contact area. The basic feature of the contact stress field is a transverse shear stress concentration under the edge of contact area. Locus of the stress concentration qualitatively agrees with the inclined transverse crack in Fig. 2.1, verifying the primary transverse shear effect in producing such cracks. Just outside of the contact area, the plate bending stress field, featuring a layerwise linear variation of the flexural stresses through the plate thickness, a parabolic variation of the transverse shear stress and the zero transverse normal stress, is rapidly recovered. Similar stress distributions have also been observed in static indentation cases (53, 54).

Based on the impact stresses calculated by finite element method, Choi, et al could predict the initial transverse cracks in laminate beams (14, 15) and plates (17) under projectile impact. Harshin's matrix failure criterion (55) was applied to each layer in the laminate. It was found that the transverse shear stress and the flexural tensile stress in the matrix direction (i.e. perpendicular to the fiber direction of the layer) are responsible for initiating the cracks. The thermal residual stress resulting from fabrication (56) and the crack constraining mechanism (57) in the laminate should also be considered. The predictions agree with the test observations (14, 15, 17).

2.2.3 Damage Extension

The Strength of Materials approach is also used to predict the damage extent in many studies (16-19). Based on the impact stress field and a stress (or strain) failure criterion, the damage extent is mapped out from the points where the stress state has satisfied the failure criterion. Various ply failure criteria have been used to predict the extent of transverse crack and fiber breakage (18, 19). Some interface failure criteria were also proposed (16-18) to predict the size, location and geometry of the delamination. Although the predictions seem to agree with the test measurements, it is noted that some empirical constants exist in the failure criteria which must be determined by correlating with the test data (16, 17).

It is not clear if the Strength of Materials approach could be applied for predicting the progressive damage process. The damage-free stress field is redistributed at onset of damage. Disturbance to the stress field due to transverse crack has been shown in Fig. 2.2. The stress distribution in a composite beam under three point bending, e.g. in a short beam shear specimen (30), is also essentially altered by the presence of a delamination, such as in the end-notched-flexure (ENF) test specimen (58). The existing defect introduces a local stress field which is mathematically singular at the crack tip and it may control the subsequent damage process. In other words, with the damage initiation controlled by finite stress concentration and material strength, the damage extension should be controlled by the fracture mechanics parameters such as the stress intensity factor or the strain energy release rate, and, on the part of material, by the fracture resistance of the composite.

Fracture mechanics approach has been applied to deal with the crack growth in isotropic materials (59). In composites, the heterogeneous and anisotropic material

properties lead to very complex fracture process, for which it is often difficult to define a suitable fracture parameter (60). In the case of delamination fracture, many studies (57) seem to show that the crack behavior may be characterized by the strain energy release rate (61). This is because the fracture is confined at the interface to undergo a coplanar crack growth, and the interlaminar fracture toughness could be measured by relatively simple tests. However, in modeling the impact-induced delamination, it is extremely difficult to simulate the dynamic fracture process in order to calculate the fracture parameter. The material resistance to unstable delamination growth is also little understood. Consequently, simplified models are often used to understand the delamination growth behavior and its controlling parameters.

Previous studies (26-29) show that drop weight impact and static indentation tests produce similar mechanical response and damage pattern in laminated composites. This may suggest the similar fracture mechanisms in both loading cases. Lu and Liu (62) considered a circular delamination in the [0/90] square plate subjected to central indentation load. The strain energy release rates, concerning different fracture modes, were calculated from a three dimensional finite element model. Numerical results showed that the strain energy release rate consists of the shear fracture modes, i.e. G_{II} and G_{III} for Mode II and Mode III respectively. No Mode I contribution was observed. Along the delamination front, G_{II} is significantly higher than G_{III}, and the locus of maximum G_{II} coincides with the fiber direction of the layer below the interface. Therefore, if the impact-induced delamination possesses the similar features in strain energy release rate, the delamination in the laminate (47) should be a Mode II dominated fracture.

In another work (63), Chatterjee, et al studied the three point bending fracture of thick laminate plates containing circular or elliptical delaminations at the midplane.

Analytical results for strain energy release rate indicated again that the delamination is subjected to a Mixed-Mode II/III shear fracture. The relative magnitudes of G_{II} and G_{III} vary along the delamination front and the variation depends on the shape of the delamination. Fracture tests on $[0_4/\pm45_2/\pm45_2/0_4]_s$ and $[0_4/\pm45_2/\pm45_2/0_8/\pm45_2/0_8]$ Graphite/Epoxy laminates showed that the delamination was initiated in a Mode II dominated fashion. It was also found that the point failure criterion for Mode II fracture, $G_{II}(\max) = G_{IIc}$, underestimated the failure load (G_{IIc} is the Mode II fracture toughness.). The total energy release rate calculated from the realistic delamination growth pattern seemed to give reasonable predictions.

Delamination fracture under transverse impact has also been studied on pre-cracked beam specimens (64-67). Dynamic strain energy release rate is calculated by beam theory analysis or by finite element method. The midplane delamination is under a primarily Mode II fracture condition (64, 66, 67), while the off-midplane delamination may undergo a Mode I dominated fracture if local buckling of the delaminated plies occurs during impact (65). Under drop weight impact conditions, the strain energy release rate is dominated by quasi-static response and the effect of kinetic energy is negligibly small (66). Most of the studies concern the dynamic initiation of delamination growth (64-66), which seems to be governed by the dynamic initiation toughness of the material.

The delamination extension may depend upon the whole fracture process with crack initiation, propagation and arrest. Simulation of such a process is extremely difficult because the delamination propagates at very high crack velocities and the fracture resistance is hard to measure as a function of the crack speed. Sankar and Hu (67) modeled the unstable delamination growth in composite beams subjected to transverse impact. The dynamic strain energy release rate G was computed by a beam

finite element model. The crack propagation was controlled by $G = G_c$, where the toughness G_c was assumed to be constant and equal to the dynamic initiation toughness. The crack arrest was defined when $G < G_c$. With the measured impact force history, the model seemed to be able to predict the delamination extension. Application of the approach to delamination growth in plate specimens has not been considered.

2.3 Interlaminar Fracture Toughness

At a given impact, the delamination growth is governed by the material resistance to interlaminar fracture. Therefore characterization of the delamination extension requires measuring the interlaminar fracture toughness. This is a difficult task because the fracture energy generally depends on the material type, the mode of fracture, and the rate of load application (60, 64, 66, 68-71), etc. The delamination toughness under static and cyclic loading conditions have been studied extensively (60, 61), while for dynamic fracture process, the delamination toughness is little understood. In this section, the current studies on delamination toughness is briefly reviewed. Loading rate effects on Mode II toughness is primarily concerned.

Initiation toughness of Mode II delamination has been studied by various researchers (66, 68). The fracture energy is found to be sensitive to loading rate. The typical variation of G_{IIc} as a function of the crack tip displacement rate is shown in Fig. 2.3. For both the thermoset Graphite/Epoxy and thermoplastic PEEK/Carbon composites, G_{IIc} remains fairly constant over the range of low loading rates but substantially decreases at the relatively high loading rates. Significant drop in G_{IIc} has also been observed in drop weight impact test on such materials (66). Similar loading

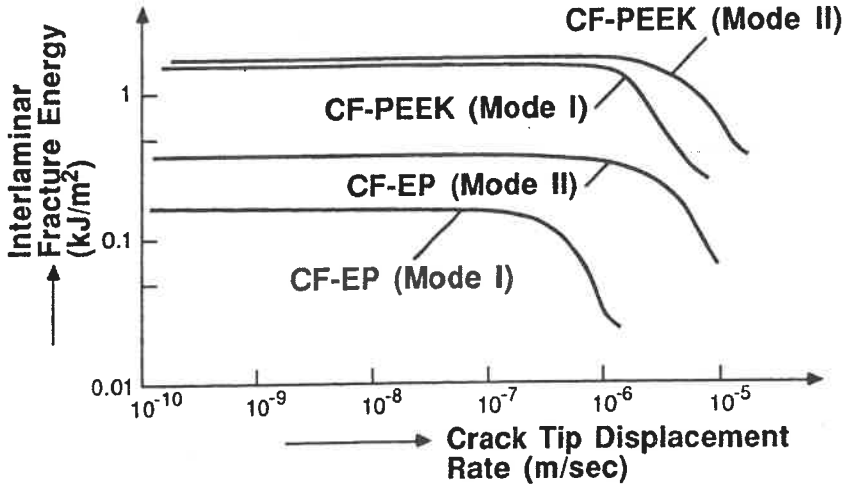

Figure 2.3 Rate sensitivity of interlaminar fracture energies in PEEK/Carbon and Graphite/Epoxy composites [68, 69] (figure from [60]). The displacement rate is defined as the rate of relative opening (Mode I) or sliding (Mode II) displacement between the crack surfaces near the crack tip

rate effects also exist in the Mode I toughness (69) (Fig. 2.3), and in the Mode III toughness (70) of composite materials.

The Mode II toughness during unstable delamination has been considered in (66, 71). A very high loading rate exists at the fast running crack tip. The variation of fracture energy as a function of crack speed could hardly be measured by the conventional test methods. As a rough estimate, the average propagation toughness is determined by the area method, i.e. by dividing the absorbed energy during delamination propagation with the resulted delamination area. Under drop weight impact conditions (66), the average Mode II propagation toughness is found to be close to the dynamic initiation toughness in Graphite/Epoxy composite, but is lower than the initiation toughness in PEEK/Carbon composite.

Measurement of the Mode II toughness at delamination arrest after unstable growth has been studied in (72). It was found that the end-loaded-split (ELS) specimen, which is a cantilever beam with a midplane crack at the loaded end, exhibits an initially unstable and subsequently stable crack growth behavior. This fracture behavior may be used to measure the Mode II crack arrest toughness if the crack could be arrested within the specimen. For Glass/Epoxy composite, the Mode II arrest toughness was found to coincide with the initiation toughness of the material (72). The ELS fracture test is recently improved to take into account the large deflection effect on toughness measurement (73).

2.4 Discussion

In summary, the impact-induced delamination in association with transverse

cracks is the major damage mode in laminated composites under low velocity impact. The damage initiation in terms of initial transverse cracking may be predicted by the Strength of Materials approach. However, using the same approach to predict the damage extent remains debatable because the damage growth is a dynamic fracture process. The fracture mechanism of the unstable delamination growth and subsequent arrest is still unknown. The material resistance to unstable interlaminar fracture is little understood.

In another respect, most of the studies in low velocity impact damage are on thermoset epoxy composites. In recent years, high performance thermoplastic composites such as PEEK/Carbon are favorably considered for structural applications (74). The materials have higher interlaminar fracture toughness which is also more sensitive to loading rate (66, 68, 69). The materials require higher processing temperatures which result in increased thermal residual stresses in the laminate (56). These matrix-controlled properties may significantly affect the impact-induced delamination and transverse cracks. Compared to thermoset composites, the study of impact damage in thermoplastic composites is still in its early stages (21-26, 34, 66).

Chapter 3

Research Program

The present study is to investigate the low velocity impact damage in Carbon Fiber/Polyetheretherketone (PEEK/Carbon) thermoplastic composite APC-2. Emphases of the study are focused on the material properties that may control the damage extension of impact-induced delamination and transverse crack. The study consists of five parts:

1) Measurement of the thermal residual stresses and *in situ* lamina strength in the PEEK/Carbon composite laminates;

2) Experimental characterization of the damage behavior in PEEK/Carbon crossply laminates by drop weight impact test;

3) Evaluation of the Strength of Materials approach for its applicability in characterizing the damage extension in impacted laminates;

4) Characterization of the crack growth behavior of impact-induced delamination by fracture mechanics approach. Identify the material properties that may control the delamination extension;

5) Measurement of the Mode II delamination toughness of PEEK/Carbon composite.

Chapter 4

Measurement of Thermal Residual Stress and *In Situ* Lamina Strength

4.1 Objective

It has been shown (14) that the thermal residual stress and crack constraining mechanism affect the initiation of transverse cracks in epoxy composite laminates under impact. Such effects may also be significant in thermoplastic laminates because of the increased residual stresses and enhanced fracture toughness. In order to evaluate such effects on transverse crack extension during impact, the residual stress and *in situ* lamina strength in PEEK/Carbon laminates are measured in this preliminary study.

4.2 Material and Processing

The thermoplastic APC-2 composite is used in the present study. The material is provided in the form of unidirectional prepreg tape by Imperial Chemical Industries (ICI). It consists of AS4 carbon fiber impregnated with polyetheretherketone (PEEK) thermoplastic matrix. Table 4.1 gives the mechanical properties of the material cited

from the ICI document (75).

Table 4.1 Mechanical properties of APC-2 composite.

Moduli (GPa)		
Longitudinal tensile modulus	E_L	134
Transverse tensile modulus	E_T	8.9
In-plane shear modulus	G_{LT}	5.1
Longitudinal flexural modulus		121
Transverse flexural modulus		8.9
In-plane longitudinal Poisson's ratio	ν_{LT}	0.29
Mass density	ρ (kg/m^3)	1600
Strength (MPa)		
Longitudinal tensile strength	σ_L	2130
Longitudinal compressive strength		1100
Transverse tensile strength	σ_T	80
Longitudinal shear strength	τ_{LT}	150
Transverse shear strength	τ_T	150 *

* estimated value.

In the present study, 152.4 by 152.4 mm flat panels were fabricated from the prepreg tape using a matched steel mold and a Wabash heat press. The recommended processing procedure (76) consists of three steps (Fig. 4.1):

1) heating the material to about 400°C within about 25 minute under the contact pressure of 0.4 MPa;
2) holding the temperature for 5 minute and applying a consolidation pressure of 0.8 MPa;
3) cooling the mold at the rate of about 20°C/min. with the consolidation pressure applied.

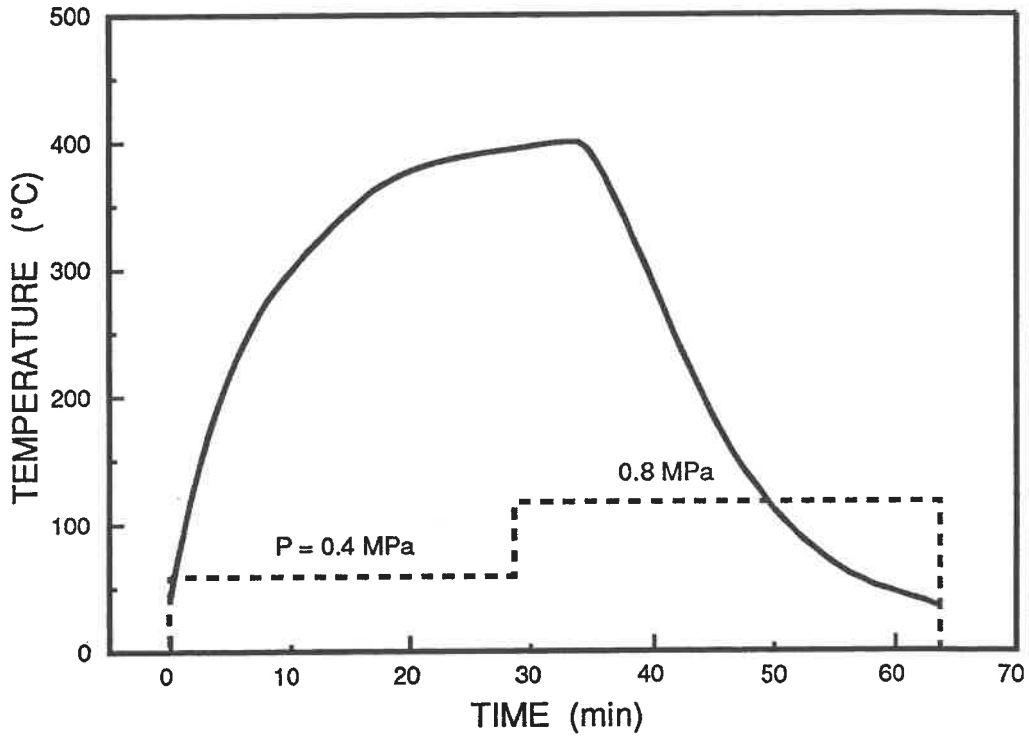

Figure 4.1 Processing procedure for PEEK/Carbon (APC-2) composite.

The rapid cooling was achieved by passing a mixture of air and water through the coolant passages incorporated in the platens of the press. The temperature was monitored by a thermocouple located in the mold. The procedure resulted in a crystallinity of about 31% in the PEEK matrix. Mechanical tests conducted in (76) and in the present study showed that the material properties achieved by the present processing procedure are very close to that in Table 4.1.

4.3 Static Test Procedure

In order to evaluate the thermal residual stress and the *in situ* lamina strength in crossply laminates, static tensile tests were conducted on the following specimens: $[90_5/0_5/90_5]$ (Laminate AT), $[90_3/0_3/90_3/0_3/90_3]$ (Laminate BT), $[90/0/ \ldots /0/90]_{15t}$ (Laminate CT) and $[0_5/90_{5n}/0_5]$ (n = 1, 2, 3, 4, 6). Tensile samples were cut from the molded plates using a diamond coated saw. Water was continuously sprayed on to the specimen to prevent excessive local heating during the cutting process. The samples had a test section length of 80 mm. The sample width was 20 mm for AT, BT and CT specimens and 12 mm for the $[0_5/90_{5n}/0_5]$ series. The side edges of the samples were polished using silicone carbide abrasive papers of #400 and #800 in succession, in order to minimize the effect of surface defects on lamina failure. Aluminum tabs were provided to the $[0_5/90_{5n}/0_5]$ specimens while it is not necessary for the AT, BT and CT specimens as discussed in (56).

During testing, tensile load was applied in the 0-degree fiber direction. So the 90-degree ply was loaded primarily in the transverse direction. Due to the lower transverse strength of the material, the 90-degree ply might fail before the final fracture

occurred. Such a ply cracking, the "first-ply-failure" (FPF) as it is termed, could be monitored by the crack appearance in the 90-degree ply which was always accompanied by an audible acoustic emission (56). The load at FPF could thus be determined. For a better detection of the FPF, the surfaces of AT, BT and CT specimens and the side edges of the $[0_5/90_{5n}/0_5]$ series were painted white before testing. At least four specimens were tested for each laminate type. The measured FPF loads are shown in Table 4.2.

In addition, a group of $[90_{15}]$ samples were also tested. The transverse strength of unidirectional APC-2 composite was found to be 80 MPa, which agrees with the value reported by ICI (75). All the tensile tests were performed on an Instron-1125 tester at a crosshead speed of 2 mm/min.

Table 4.2 Results of static tensile test.

Specimen		No. of samples	FPF load (kN/m)	Residual stress in 90° ply(MPa)	In-situ strength in 90° ply(MPa)
AT	$[90_5/0_5/90_5]$	6	479.5 (329.6-560.1)	40	——
BT	$[90_3/0_3/90_3/0_3/90_3]$	6	537.9 (455.2-690.9)	41	——
CT	$[90/0/.../0/90]_{15T}$	6	1644.0 (1422.3-1747.9)*	41.5**	——
AN1	$[0_5/90_5/0_5]$	6	2813.5 (2791.9-3095.2)*	42**	170
AN2	$[0_5/90_{10}/0_5]$	4	2103.2 (2064.0-2162.5)	42**	142
AN3	$[0_5/90_{15}/0_5]$	4	1463.3 (1306.7-1526.6)	41**	107.5
AN4	$[0_5/90_{20}/0_5]$	4	1239.0 (1153.4-1329.4)	40**	85.5
AN6	$[0_5/90_{30}/0_5]$	4	998.7 (830.8-1091.8)	39**	81

* "First-ply-failure" did not occur.

** calculated by incremental laminate analysis.

4.4 Thermal Residual Stresses

In the present study, the thermal residual stresses were determined using a similar method as proposed in (56). The method is based on the classical laminate theory and an incremental analysis procedure which takes into account the changes with temperature of the thermal expansion coefficients and elastic properties of the material. As measured in (56) for APC-2 composite (Fig. 4.2a), the fiber-controlled longitudinal modulus (E_L) remains constant with increasing temperature. The transverse modulus (E_T) is found to decrease slightly below the glass transition temperature (T_g) but to drop rapidly above T_g. The transverse thermal expansion coefficient also changes at around T_g (Fig. 4.2b). Therefore two steps are considered in the incremental analysis, i.e. from the stress-free temperature (T_{sf}) to T_g, and then from T_g to the room temperature (T_r). It is found in (56) that a constant value of 1 GPa could be used to average the rapidly decreasing E_T from T_g to T_{sf}, and the predicted residual stresses agree very well with test measurements (56). Although the same material is considered in this study, the average modulus cannot be used because the cooling rate in (56) is 3°C/min. and is about 20°C/min. in the present work. The cooling rate may affect the material properties (77). Therefore, a modified procedure is considered in this study, i.e. the residual stress measured by the "first-ply-failure" method (56) is used in association with the incremental laminate analysis to determine the average transverse modulus $\bar{\bar{E}}_T$ at above T_g.

The "first-ply-failure" (FPF) in the AT, BT and CT specimens corresponds to transverse cracking in the 90-degree surface plies. At onset of such cracks, the following relation exists in the transverse direction of the surface ply:

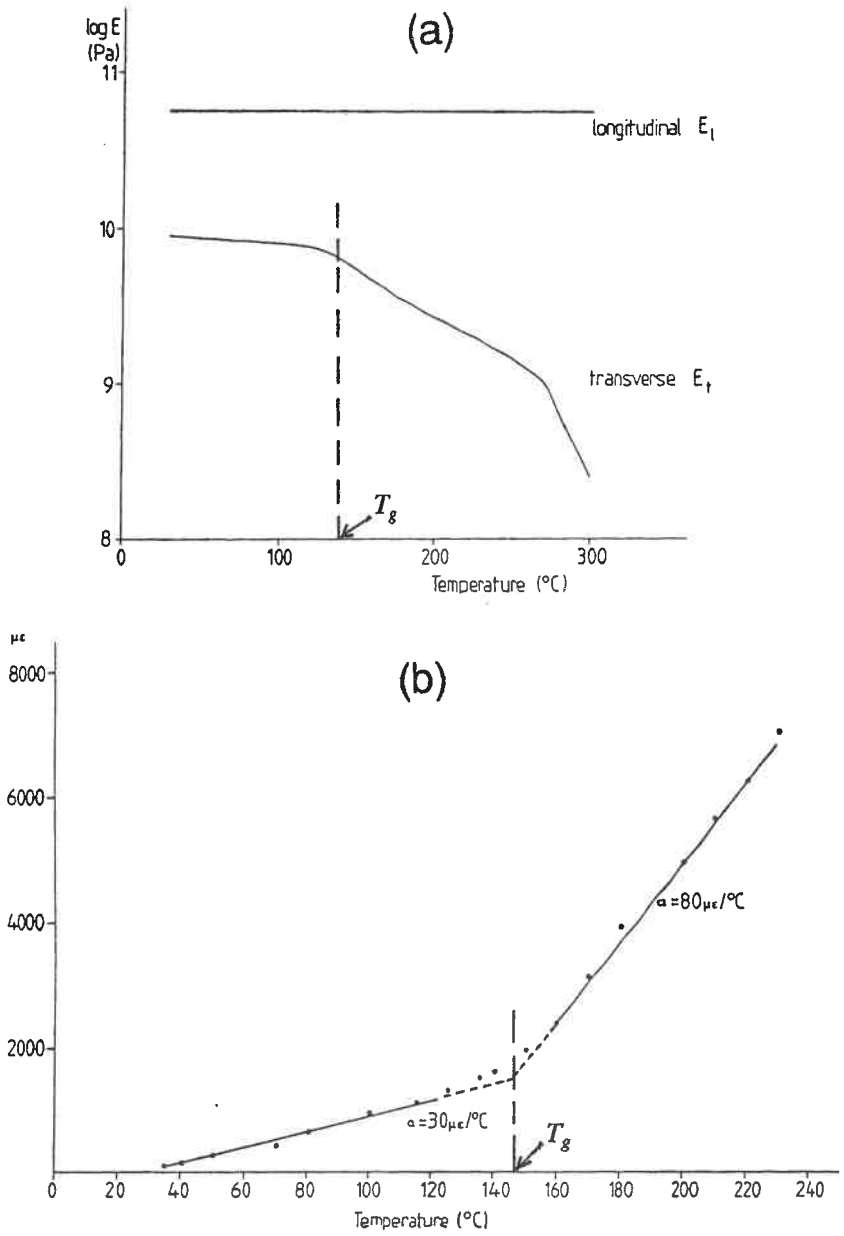

Figure 4.2 Temperature dependence of APC-2 material properties: (a) longitudinal modulus E_L and transverse modulus E_T; (b) transverse thermal expansion showing the variation of α_T at about T_g [56].

$$\sigma_m + \sigma_r = \sigma_T \tag{4.1}$$

where σ_m is the mechanical stress caused by FPF load, σ_r is the transverse residual stress, and σ_T is the transverse tensile strength of the lamina. σ_m may be calculated by laminate theory from the FPF load. As discussed in (56), the crack constraining effect may be negligible in the surface plies, so the unidirectional strength of 80 MPa reference can be substituted for σ_T in Eq. 4.1 to determine the residual stress. Although transverse cracks are always observed in (56) for laminates with different surface ply thickness, they cannot be detected in Laminate CT in the present study. This implies that the crack constraining effect is still significant when the surface ply thickness is very small. It can be expected that the thicker the surface ply, the less significant the crack constraining effect. From the FPF load of AT and BT specimens, σ_r can be determined by assuming σ_T = 80 MPa in Eq. 4.1. The residual stress for the two laminates is given in Table 4.2 and is subsequently used to identify the average modulus $\overline{E}_T$ by the incremental analysis. The material properties used in the calculation are shown in Table 4.3. Most of the material constants are taken from the ICI document (75) because the tests in (76) give similar material property values. The glass transition temperature T_g = 143°C is also from (75), while the stress-free temperature T_{sf} was determined by the same method as that in (56). A group of $[0_3/90_3]$ beam specimens were heated and T_{sf} was measured as the temperature at which the specimen flattened. T_{sf} is about 290°C in the present study. It is found that $\overline{E}_T$ is 1.23 GPa in the AT specimen and 1.29 GPa in the BT specimen. These values are higher than 1 GPa used in (56). The average $\overline{E}_T$ is subsequently included in Table 4.3 to predict the residual stress in the other laminates.

Table 4.3 Material properties of APC-2 used for residual stress calculation.

Constant		Below T_g (23°C-143°C)	Above Tg (143°C-290°C)
Longitudinal tensile modulus	E_L (GPa)	134	134
Transverse tensile modulus	E_T (GPa)	8.9	1.23
In-plane shear modulus	G_{LT} (GPa)	5	--- *
Longitudinal Poisson's ratio	ν_{LT}	0.29	0.5**
Longitudinal thermal expansion coefficient	α_L	0.5	1
Transverse thermal expansion coefficient	α_T	30	75

* Shear modulus does not affect the residual stress in crossply laminates [56].

** estimated value [56].

4.5 *In Situ* Lamina Strength

Transverse cracking of a lamina in a laminate depends upon the layer thickness and the constraint from adjacent layers. The *in situ* strength of the lamina (57) is typically higher than the strength measured on specimens made of unidirectional composite (57). To evaluate the crack constraining effect on impact damage, the *in situ* strength of the lamina in crossply laminates was measured in the present study by the "first-ply-failure" test on $[0_5/90_{5n}/0_5]$ laminate family, where n = 1, 2, 3, 4, 6. The test results are shown in Table 4.2. Again, Eq. 4.1 holds in the central 90-degree layer at FPF, and σ_T is the *in situ* lamina strength. The mechanical stress σ_m can be calculated from the FPF load by laminate theory, and the residual stress σ_r is evaluated by the incremental laminate analysis. The *in situ* strength is given in Table 4.2 and is plotted in Fig. 4.3 as a function of the layer thickness. Also shown in Fig. 4.3 is the transverse residual stress in the 90-degree layer.

The *in situ* strength of APC-2 composite shows the same variation as that of epoxy composites (57), i.e., the thinner the layer, the more significant the crack

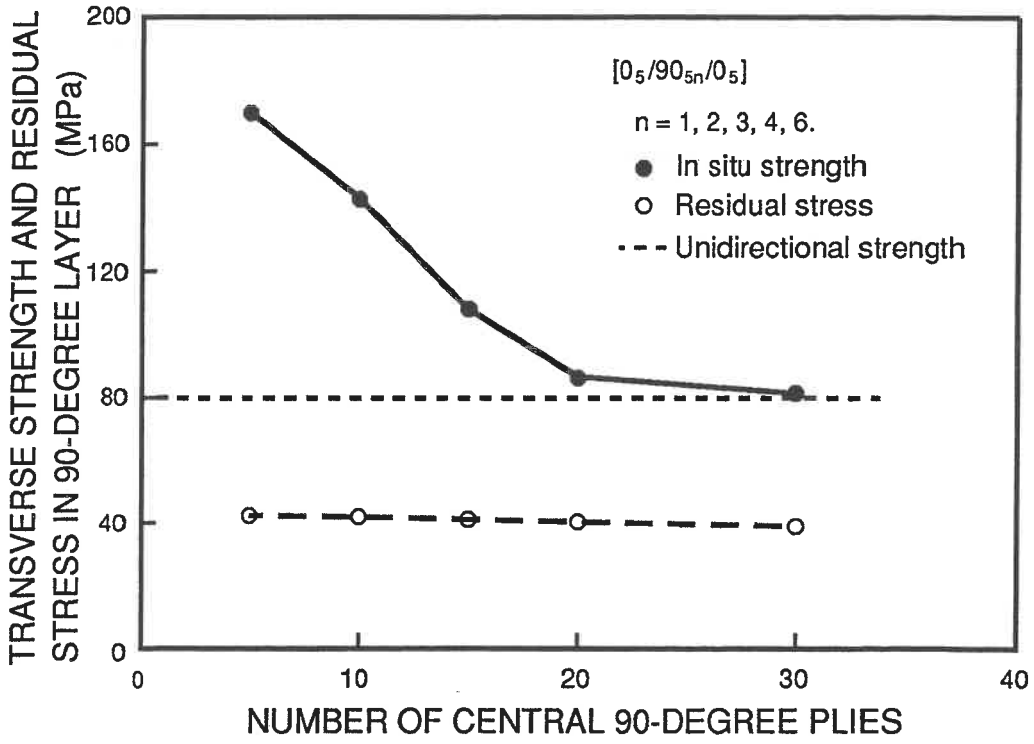

Figure 4.3 Transverse *in situ* strength and thermal residual stress in the 90-degree lamina of PEEK/Carbon laminates $[0_5/90_{5n}/0_5]$ (n = 1, 2, 3, 4, 6).

constraining effect. In the $[0_5/90_5/0_5]$ specimen, transverse cracking of the 90-degree layer could not be observed before the ultimate failure occurred. The *in situ* strength of this laminate was calculated from the ultimate failure load and might have been underestimated. Fig. 4.3 suggests that, at n = 6, the *in situ* strength is very close to the unidirectional strength. This agreement verifies the residual stress calculation because, as the 90-degree layer becomes thicker, the constraining effect decreases rapidly while the residual stress varies only slightly. Therefore, if the residual stress is not accurately estimated, the *in situ* strength cannot converge to the unidirectional value.

In the AT, BT and CT specimens discussed earlier, the *in situ* strength of the surface ply should follow a similar variation to that in Fig. 4.3, but a more rapid drop to the unidirectional value may be expected because the constraining effect exists at only one side of the ply. The assumption of σ_T = 80 MPa for the surface plies of AT and BT specimens seems to be acceptable in the sense that reasonable prediction of the residual stress has been made in the $[0_5/90_{5n}/0_5]$ laminate family.

Chapter 5

Experimental Characterization of Low Velocity Impact Damage

5.1 Objective

The objective of this part of the study is to establish the damage behavior of PEEK/Carbon composite under low velocity impact. The damage behavior is characterized in both qualitative and quantitative manners, so as to provide a physical insight into the damage process and a solid test data base for the analyses in Chapters 6 and 7.

5.2 Impact Test Procedure

5.2.1 Specimen Preparation

Square plates 152.4 by 152.4 mm were fabricated following the procedure in Section 4.2. Three crossply laminates were selected for impact testing, i.e. $[0_5/90_5/0_5]$ (Laminate A), $[0_3/90_3/0_3/90_3/0_3]$ (Laminate B) and $[0/90/.../90/0]_{15t}$ (Laminate C).

These laminate types have been studied in (33, 48) for impact damage mechanisms of epoxy composites, and in (34) for the penetration resistance of the thermoplastic polyphenylene sulfide (PPS) composite.

In order to study the fracture surfaces of the Mode I and Mode II interlaminar fracture under impact load, end-notched beam specimens with $[0_{13}/90/0_{13}]$ lay-up were prepared with the dimensions 152 by 25.4 by 3.8 mm. A strip of Kapton film, 25 μm thick, was inserted between one of the 0/90 interfaces during laying up to provide a 35 mm precrack at one end.

5.2.2 Drop Weight Impact Test

The impact tests were conducted on a Dynatup-8200 drop weight tester, as shown in Fig. 5.1. The instrumented impact tester can provide a digitized record of the impact force history. Since the impactor mass of the tester, 3.1 kg in minimum, is not suitable for testing the laminates in a low energy range, an aluminum crosshead was built to which the Dynatup load cell could be attached. The modified impactor is 12.7 kg in mass and has a steel hemispherical nose of 12.7 mm in diameter.

A fixture was designed to hold the plate specimen during testing (Fig. 5.2). It could be adjusted according to the plate thickness so as to provided a tight and uniform clamp at the plate edges. The test section was 128 by 128 mm. In order to exclude the possibility of buckling-related delamination growth (50), reverse bending of the plate was suppressed during impact test. A grid-shaped steel frame was attached to the top holder of the fixture, and eight screws were placed in the frame to provide local constraints to the impacted plate surface. Actually, each screw was adjusted to leave

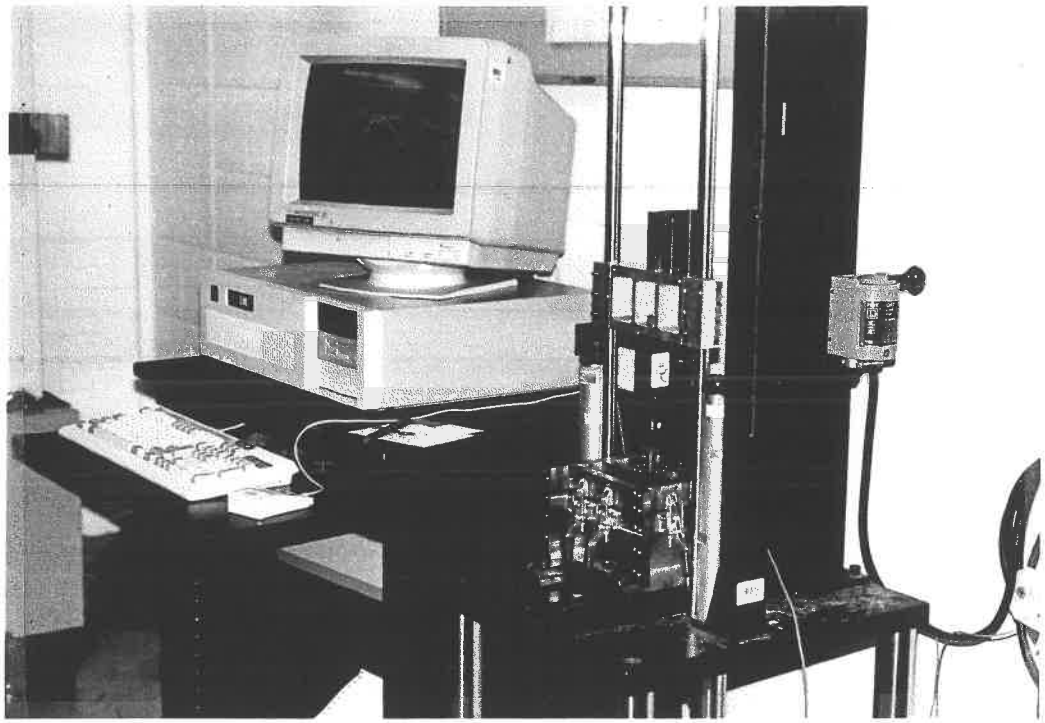

Figure 5.1 Drop weight impact test setup.

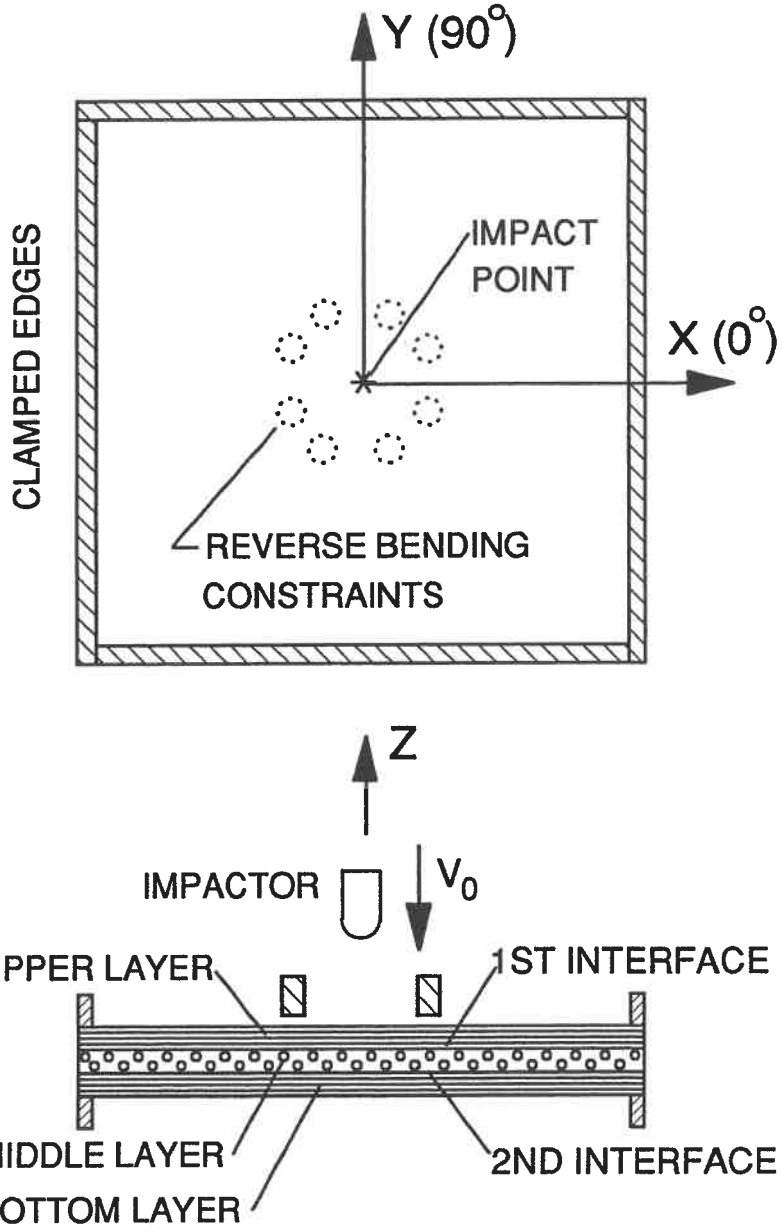

Figure 5.2 Impact test of a $[0_5/90_5/0_5]$ PEEK/Carbon (APC-2) laminate.

about 0.5 mm spacing before touching the plate surface, because a small reverse bending may occur at the beginning of impact (36).

During testing, the impactor was released at a given height to strike the plate center. In the case of subpenetration damage, the impactor rebounded. By capturing the impactor at its first rebound, only a single strike was allowed. The impact velocity varied between 1.25 m/s and 5.61 m/s, resulting in an energy range from 1 to 20 J.

5.2.3 Indentation Test

After impact, the first half of the specimens (the first set) were subjected to damage detection. For the other half (the second set), before damage detection, a static indentation test was conducted to measure the flexural compliance of the damaged plates. In such cases, the plate was clamped as in impact test and the same intender nose as the impactor was used. A central indentation load of 0.3 kN was applied with an Instron-1125 tester at the crosshead speed of 5 mm/min. The low load level did not cause further damage to the plate.

5.2.4 Damage Detection

Three methods were used to detect the damage extent in impacted plates, i.e., visual inspection, penetrant-enhanced X-radiography and the thermal deplying technique (44).

Visual inspection reveals the damage in the surface layers of the laminate. To

visualize the delamination surface inside the laminate, a few A type plates were cut along the 0-degree fiber direction into beam samples containing the delamination area. Away from the damage area, a surface notch was cut across the beam width with a depth into the middle layer. The beam was then subjected to a static peeling test similar to that as shown in Fig. 5.3a. A stable Mode I delamination was initiated from the surface notch and the delamination surface was gradually exposed. The Mode I fracture surface provided a distinct background to that of the impact-induced delamination.

Internal damage in the laminates could be detected by the penetrant-enhanced X-radiography. Tetrabromoethane (TBE) agent was used as the X-ray opaque penetrant. At first, some small holes (0.5 or 1.0 mm in diameter) were drilled at and around the impact site to help penetration of the TBE agent into the damaged area. It was later found that the TBE agent could penetrate into the plate from the transverse cracks in the surface layer, giving the same results as from the holes. The X-ray exposure at 100 kV for 10 second, with the focus-sample distance of 80 mm, was found to give the best damage image on the Dupon NTT30 film. After X-radiography, the plates were ventilated to volatilize the TBE agent and were prepared for the thermal deplying examination.

Based on the damage image from X-radiography, the plates with extensive delaminations were unstacked by the thermal deplying technique (44). Though invented for thermoset composites, the technique was found to be applicable to the thermoplastic APC-2 composite as well. Ether solution of gold chloride was used to penetrate the damage area. The sample was then heated in an oven to about 550°C for a duration of about 30 to 50 minute (depending on the laminate type). The sample was then taken out of the oven and cooled down for deplying. Size and location of the

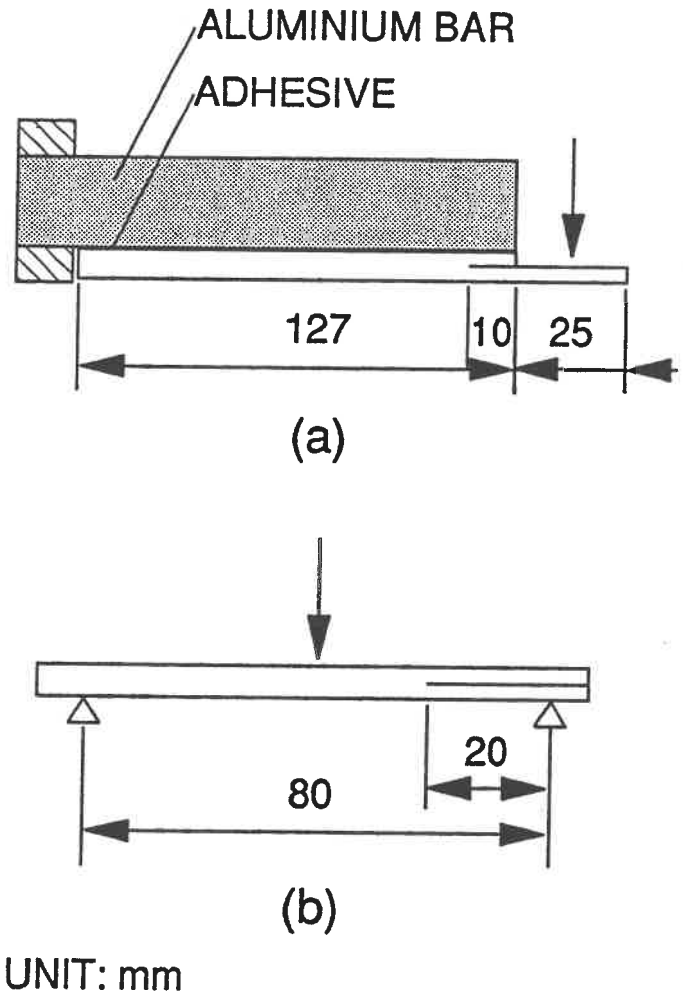

Figure 5.3 Impact fracture tests of end-notched beams: (a) Mode I; (b) Mode II.

delamination at each interface could be determined from the damage area marked by gold. The extent of fiber breakage could also be found in the deplied layers.

5.2.5 Scanning Electron Microscope (SEM) Examination

To identify the failure mechanism, fractography of impact-induced delamination was examined using SEM and was compared to that of the pure Mode I and Mode II impact fracture surfaces. The Mode I and Mode II fracture surfaces were produced by the impact tests on the pre-cracked beam specimens as shown in Fig. 5.3. 10 to 12 J impact energy was used to initiate the delamination in both modes. The beam was then opened and the fracture surface examined under SEM.

5.3 Results and Discussion

5.3.1 Damage Modes and Impact Energy

Figs. 5.4 shows the typical damage states in the APC-2 laminates. The same damage modes as in thermoset epoxy composites occur in succession with increasing impact energy: the transverse crack, delamination and fiber breakage. The dominant damage modes differ from one laminate type to the other. Therefore, in the preliminary phase of testing, the impact energy was varied to cover the range from damage initiation to final penetration.

It was found that, in Laminates A and B, the transverse cracks occur at a very

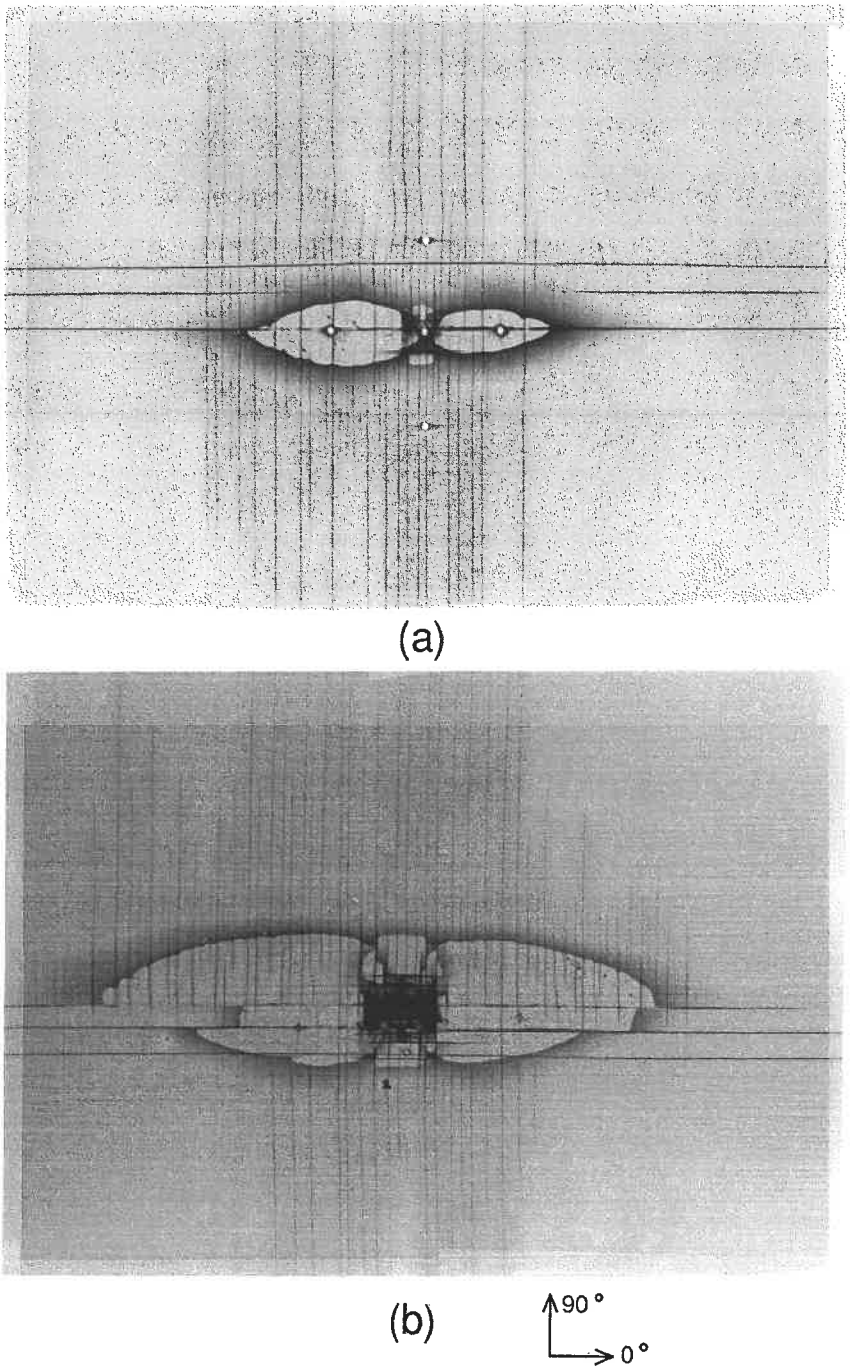

Figure 5.4 Low velocity impact damage in PEEK/Carbon (APC-2) crossply laminates, Laminate A: (a) 5 J; (b) 10 J.

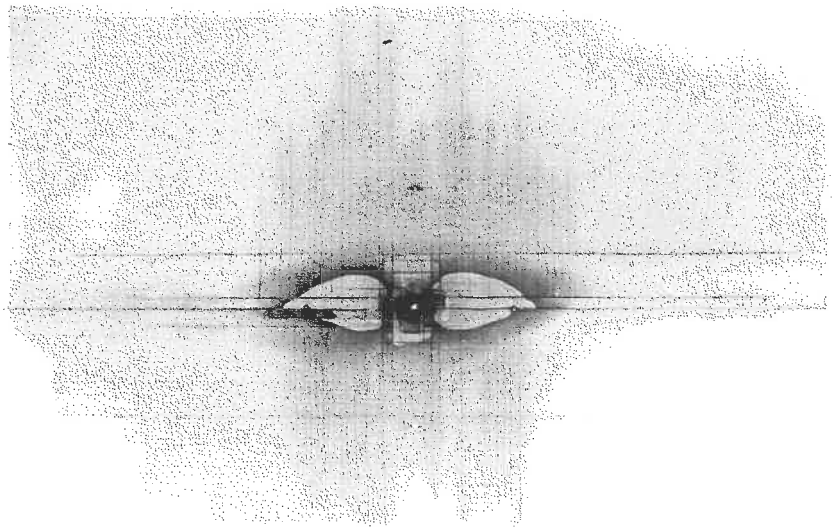

(c)

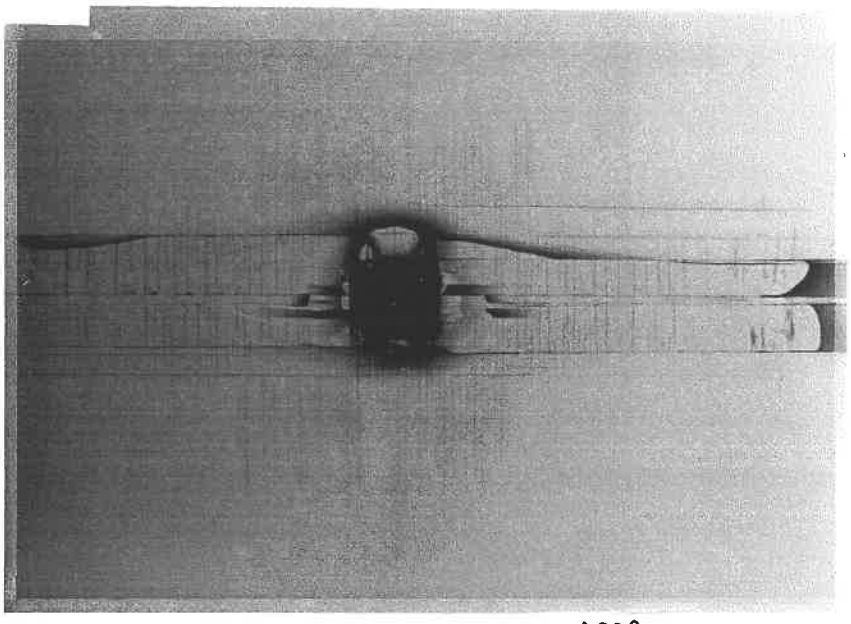

(d)

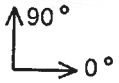

Figure 5.4 (Continued) Laminate B: (c) 10 J; (d) 15 J.

(e)

(f)

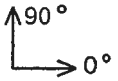

Figure 5.4 (Continued) Laminate C: (e) 10 J; (f) 13 J.

low energy level (about 0.5 to 1 J) while the delamination suddenly initiated at about 3 J. These two matrix-controlled damage modes predominate the damage state under the impact of below 10 J, and no apparent fiber breakage was produced. A shallow impression due to impactor indentation was observed at the impact site. Local indentation crash and fiber breakage began to occur in both laminates at around 10 J impact. In Laminate A, the delamination area could extend nearly up to the clamped edges at 10 J impact but penetration did not occur. Partial penetration occurred at about 15 J impact in Laminate B.

In contrast to Laminates A and B, very limited transverse crack and delamination were observed in Laminate C until penetration occurred. At about 10 J impact (Fig. 5.4e), a "cross crack" through the plate thickness was formed by the overlapped transverse cracks in the 0 and 90-degree layers. This "cross crack" confined itself near the contact area, and the fibers in each layer began to be cut along this "cross crack" due to the stress concentration at the transverse crack tips. Such a "cross crack" was the first sign of the penetration process. Complete penetration occurred at about 13 J impact but, as can be seen in Fig. 5.4f, little delamination and fewer transverse cracks extended beyond the penetrated area.

It is worth noting that, though the impact energy of about 10 J seemed to be the threshold for fiber breakage in the three laminates, a distinctly different failure process existed in Laminates A and B compared to that in Laminate C. At 10 J impact, the residual contact impressions in Laminates A and B were about 10 mm and 8 mm in diameter respectively, while only 5 mm in Laminate C. The larger contact area associated with extensive transverse crack and delamination in Laminates A and B seemed to prevent the immediate localization of damage process as that in Laminate C, and the penetration was also retarded.

Preliminary tests showed that transverse crack and delamination dominate the damage state in Laminates A and B, while fiber breakage controls the penetration failure in Laminate C. Since the primary objective of the present work is to study the matrix-controlled damage modes, the delamination in particular, additional tests were conducted on Laminates A and B in order to characterize the damage behavior. Accordingly, the impact energy was carefully selected to generate different delamination sizes without causing significant fiber breakage. The energy range was between 3 and 10 J for both A and B type laminates. As can be seen in Figs. 5.4a and 5.4c, the delaminations are always associated with transverse cracks. So the two damage modes were characterized respectively in the following sections.

5.3.2 Delamination Area

Similar to epoxy composites (45-47), impact-induced delamination in the APC-2 crossply laminates is a "peanut shape" area at the interface. The delamination geometry may be defined by its length (L) and width (W) along and perpendicular to the fiber direction of the layer below the interface, respectively (21, 45). Fig. 5.5 shows the delamination at the second interface in an A type laminate after 5 J impact. The delamination was initiated from the transverse cracks in the 90-degree middle layer and propagated in the fiber direction of the 0-degree bottom layer. The delamination width, W_2, seems to involve a sequential crack initiation process from the transverse cracks along the delamination path. After initiation, the delamination edges which define W_2 were under a Mixed-Mode II/III loading (62) and did not seem to have a significant growth. This is probably because the strain energy release rate at such

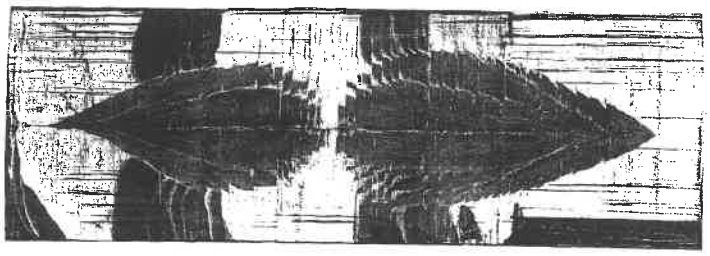

Figure 5.5 Delamination surface at the second interface of an A type laminate after 5 J impact.

locations is lower (62) while the mixed mode shear toughness is comparable to the pure Mode II toughness in the APC-2 composite (78). The delamination propagated in the 0-degree fiber direction in which the strain energy release rate may be higher and be Mode II dominated (62). The delamination length, L_2, seems to be controlled by an unstable fracture and subsequent crack arrest process (21, 35). Such mechanisms can be seen in Fig. 5.5 by the zigzag geometry at the delamination edges which define W_2. Each zig corresponds to a transverse crack in the middle layer. And the crack front becomes smooth at the delamination edges which define L_2, where the crack arrest occurred.

The delamination surface was also studied by scanning electron microscope (SEM). Figs. 5.6a and 5.6b present, respectively, the typical morphologies of the Mode I and Mode II impact fracture surfaces; Fig. 5.6c shows the fracture surface of the impact-induced delamination in plate specimens. These photographs were taken on the 0-degree ply surface. The crack propagation direction was from the top to the bottom. An obvious comment is that the impact-induced delamination surface resembles that of the Mode II fracture, which may possibly be the dominant failure mechanism. In both cases, the delamination surface exhibited significant shear deformation of the matrix, with no distinct hackles such as observed in epoxy-based composites (79). However, in the Mode I delamination surface, an irregular hackle pattern was observed, which seems to be formed from the resin rich region between the fibers. The above observations seem to suggest that the impact-induced delamination is mainly governed by a shear Mode II fracture.

Fig. 5.7 shows the ply-by-ply delaminations in the typical laminates. The delamination at each interface is initiated from the transverse shear cracks in the upper layer and propagates in the fiber direction of the lower layer of the interface. The

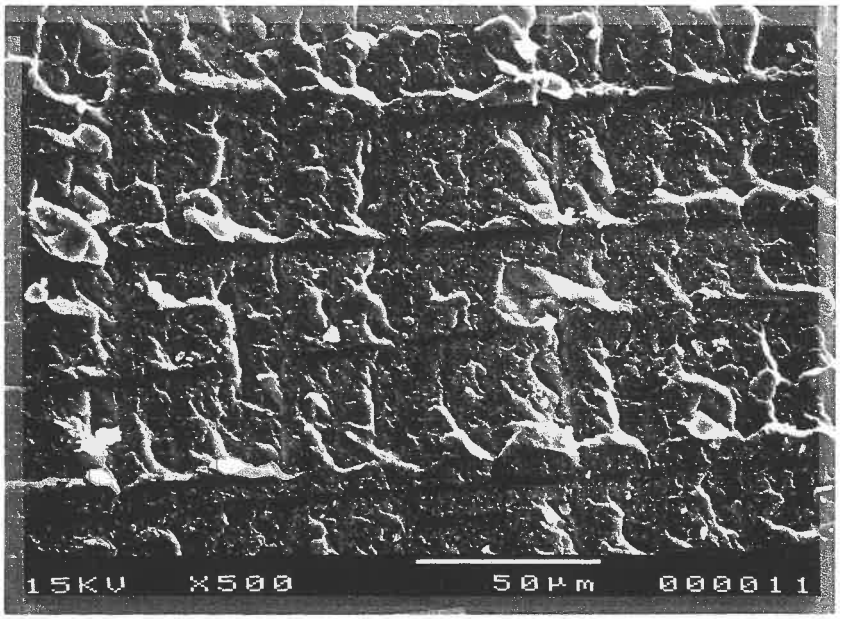

(a)

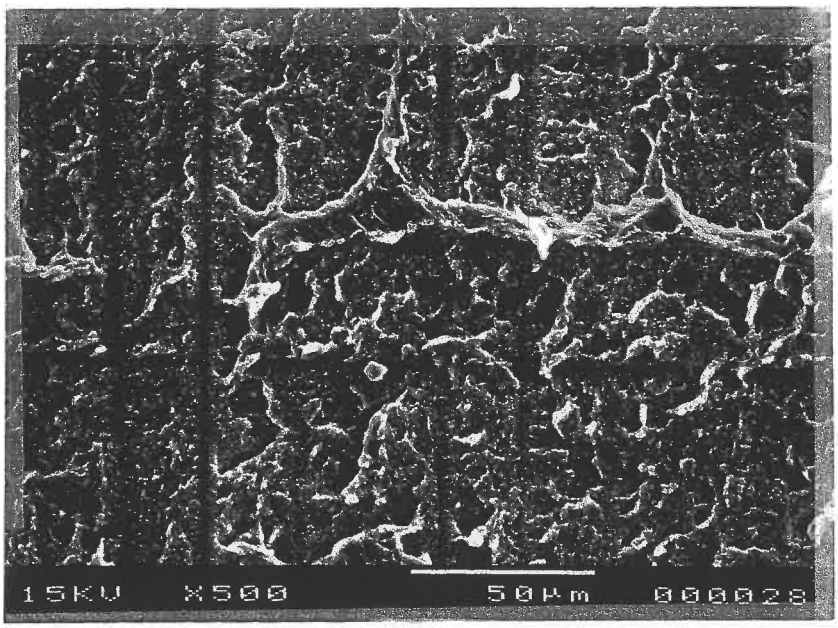

(b)

Figure 5.6 Fracture morphologies of 0/90 interface delamination produced by impact load: (a) Mode I; (b) Mode II.

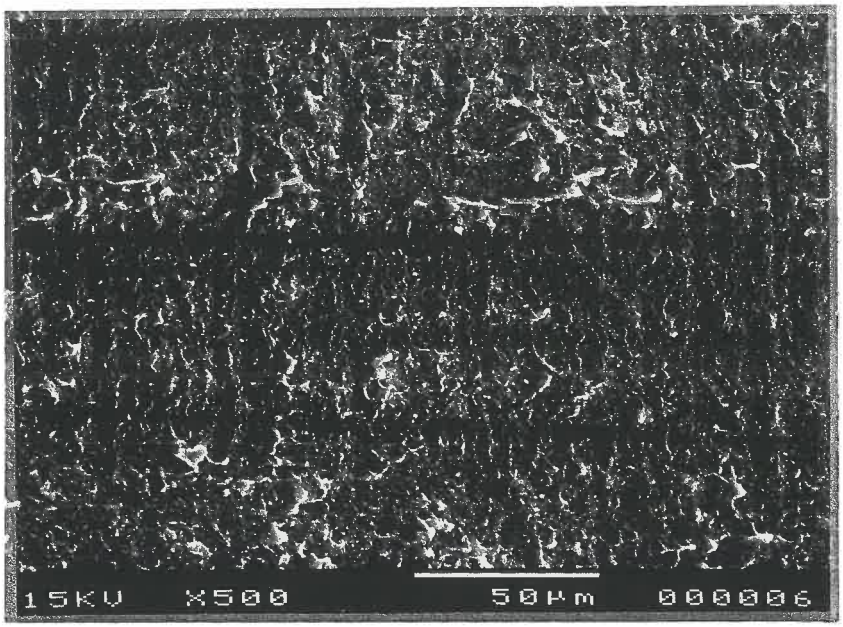

(c)

Figure 5.6 (Continued): (c) impact-induced delamination.

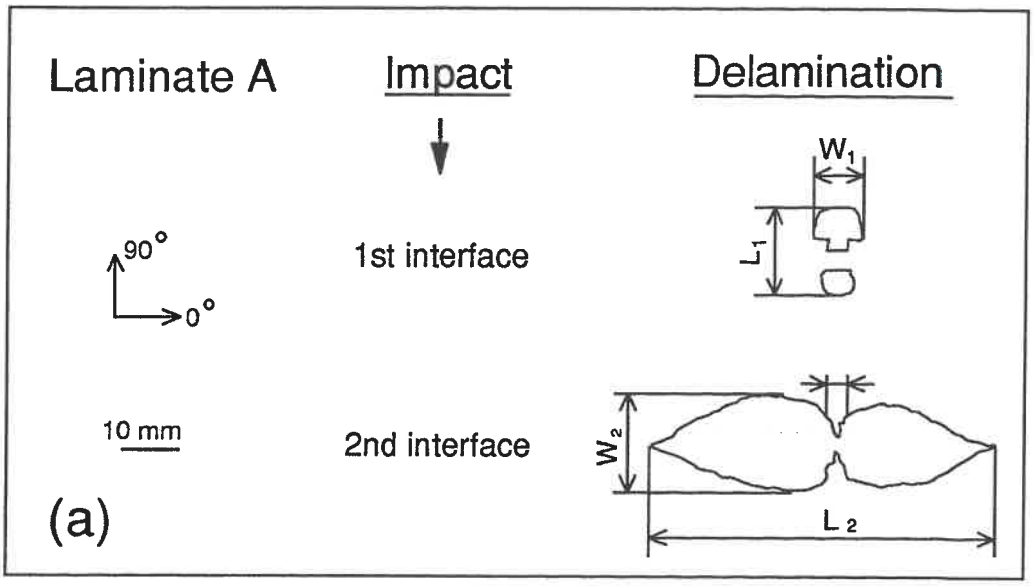

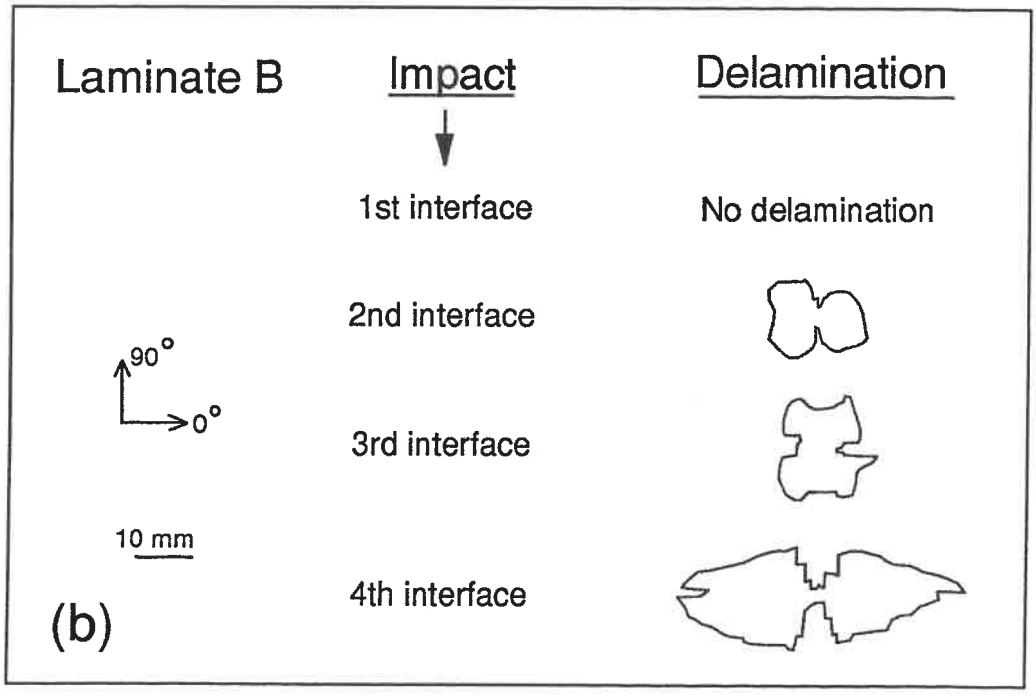

Figure 5.7 Delamination geometry and distribution in impacted laminates: (a) Laminate A; (b) Laminate B.

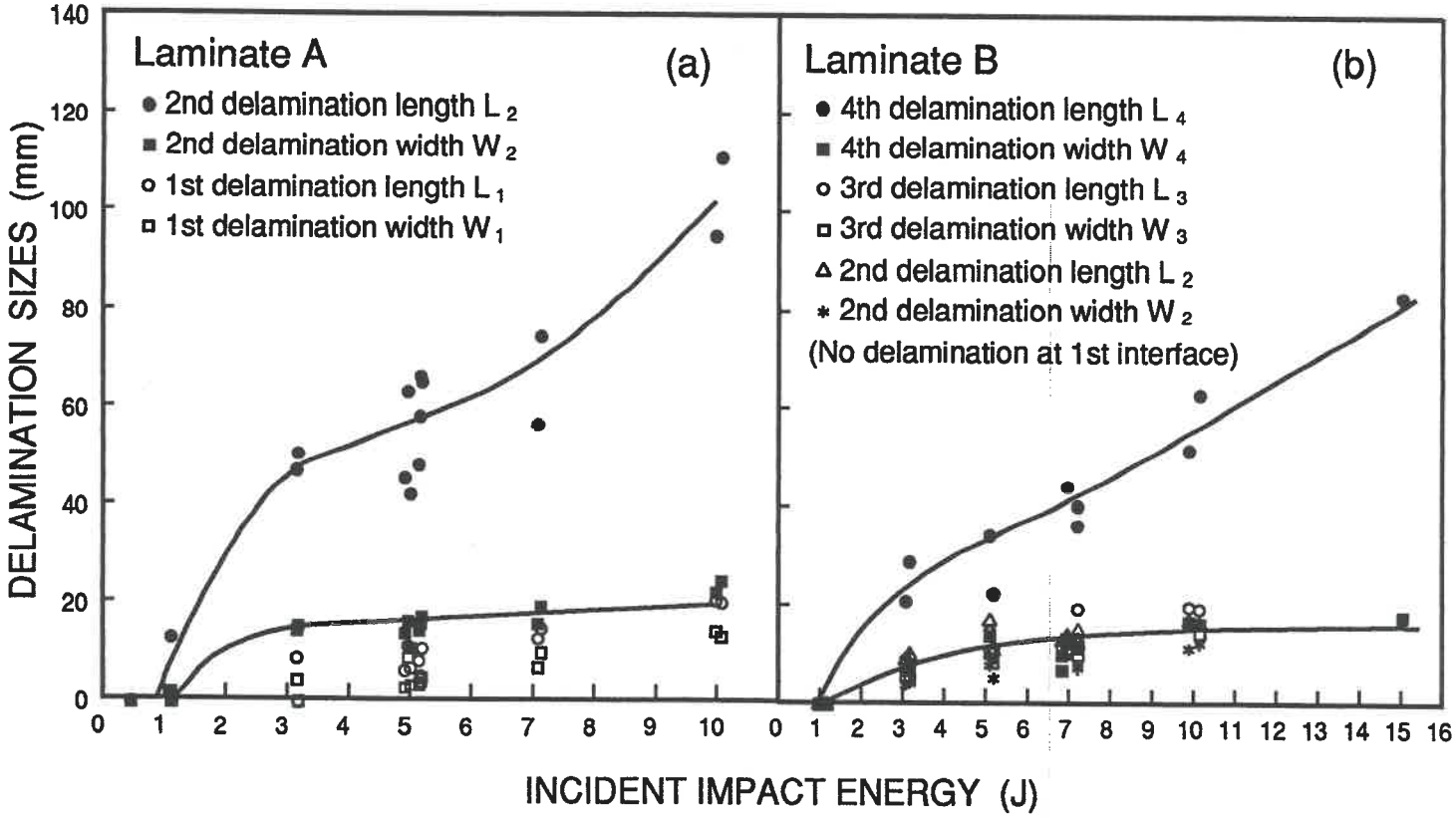

Figure 5.8 Sizes of delamination versus incident impact energy: (a) Laminate A; (b) Laminate B.

delaminations are distributed in a growing sequence if viewed in the impact direction. The largest delamination occurs at the 2nd interface of Laminate A and the 4th interface of Laminate B, always the last interface near the non-impacted surface of the plate. Variations of the delamination sizes are plotted in Fig. 5.8 against the impact energy.

To compare with the delamination resistance of epoxy composites, the total delamination area in Laminate A is plotted in Fig. 5.9 against the imparted impact energy. The total delamination area is the summation of the delamination area at every interface. The previously reported linear dependence (47-49) was found to be valid. Results for the same laminate type but for epoxy composites were taken from (47, 49) for comparison. Considering the difference in plate dimensions, the APC-2 composite seems to be more resistant to impact-induced delamination than the Kevlar/Epoxy and Graphite/Epoxy composites. It is seen that the delamination resistance depends not only on the matrix systems but also on the fiber systems. The low resistance in Kevlar/Epoxy composite is due to the relatively poor fiber/matrix adhesion in the material (49). The Glass/Epoxy composite exhibits a good resistance because the lower modulus of glass fiber reduces the stiffness mismatch between the layers and thus the interlaminar stresses are reduced as well (49).

5.3.3 Transverse Crack Distribution

Transverse cracks in the surface layers can be found by inspection of the plate surfaces. In the A and B type laminates, some short cracks are observed in the impacted layer near the contact area. A few cracks occur in the non-impacted surface

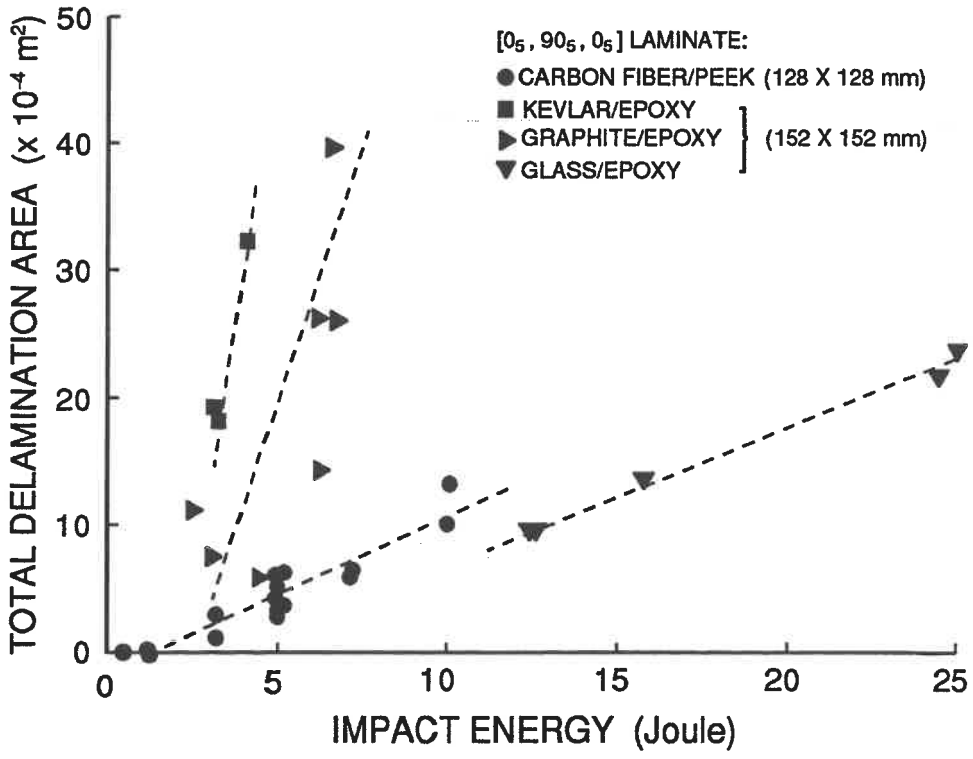

Figure 5.9 Total delamination area versus imparted impact energy for $[0_5/90_5/0_5]$ laminates.

layer which extend over the whole span of the plate. Such cracks began to occur at the low energy level at which the delamination was not initiated, and the crack distribution did not change significantly from one energy level to the other.

The cracks in the internal layer(s) can be identified in the X-ray pictures. In both A and B type laminates, a set of evenly distributed extensive 90-degree cracks is observed. Some short cracks are also found around the delamination area, which are evidently associated with the delamination growth (29). Distribution of the extensive 90-degree cracks can be characterized by the area of crack distribution and the average crack spacing, which are shown respectively in Figs. 5.10 and 5.11. It is seen that the extensive transverse cracks began to occur at the low energy level before delamination initiation, and only slight variations in crack distribution could be observed over the interested energy range.

It is worth noting that the extensive 90-degree cracks in Laminate B refer to the cracks in the 4th layer of the laminate. This is confirmed by the observation that the 0-degree cracks in the 3rd layer, which can be identified in Fig. 5.4c, distribute in a much smaller area than the extensive 90-degree cracks. Even smaller cracking area can be expected in the 2nd layer which is at the compressive side of the bending deformation. Therefore, the extensive 90-degree cracks cannot be in the 2nd layer and must be in the 4th layer of the laminate.

5.3.4 Impact Force and Deflection

Fig. 5.12a shows the load-time history of an A type laminate subjected to 5 J impact. A relatively high frequency oscillation is found to superimpose on the basic

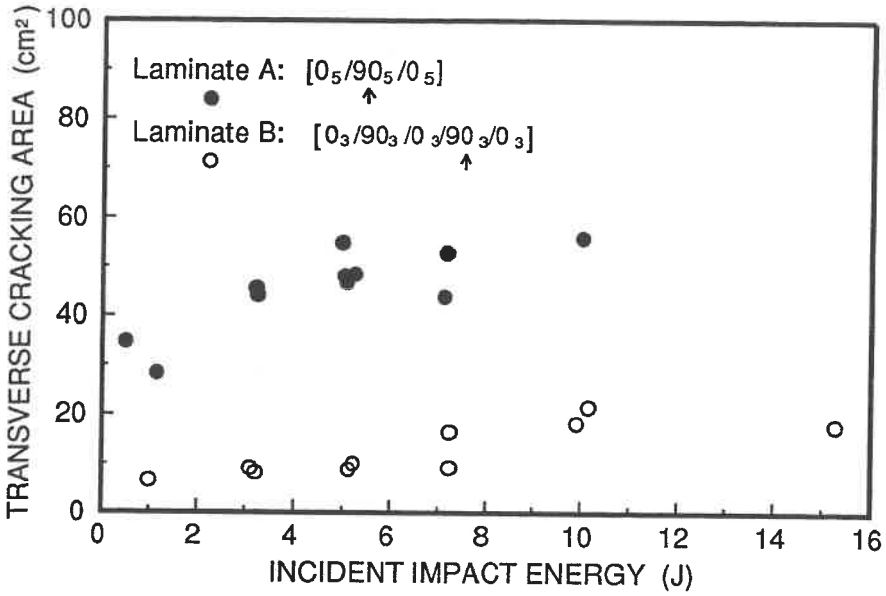

Figure 5.10 Area of transverse crack distribution versus impact energy:

(a) Laminate A, the 2nd layer; (b) Laminate B, the 4th layer.

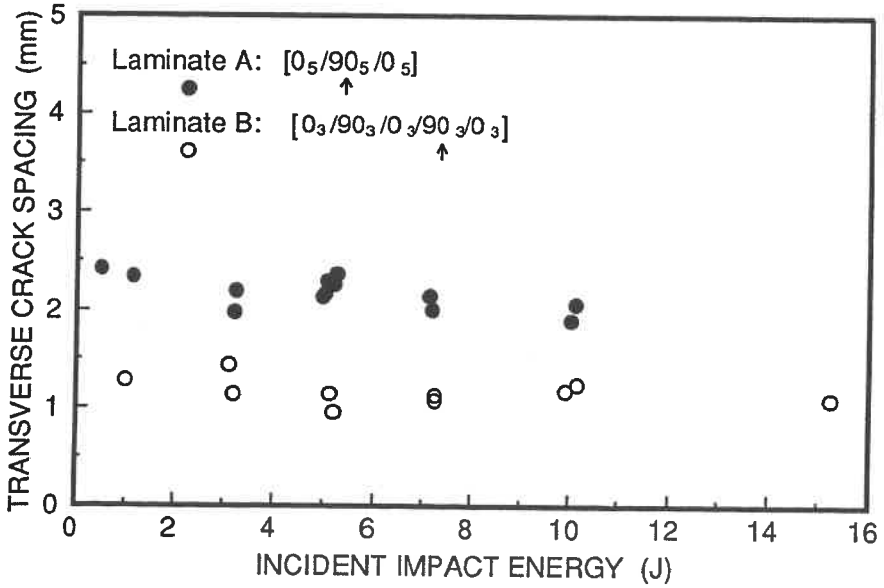

Figure 5.11 Spacing of transverse cracks versus impact energy:

(a) Laminate A, the 2nd layer; (b) Laminate B, the 4th layer.

load-time curve. This oscillating signal seems to be related to the damage growth during impact (26, 27, 37). It occurred and lasted during the loading period, and ceased when unloading began, possibly implying that the damage growth finished around the time of maximum impact load. As a verification, the same plate was impacted again at a slightly lower energy level. The response in Fig. 5.12b shows no oscillations like those in Fig. 5.12a and the subsequent damage detection indicated no apparent further damage from the second strike.

It is noted that the noise on the impact load may also be caused by the inertia effect at collision between the impactor and the specimen, or by friction of the crack surfaces. Such noise, however, seems to be smaller in amplitude than that induced by damage growth, as can be seen in Fig. 5.12b. It is worth noting that Fig. 5.12a is representative of the tests in which the laminate did not incur extensive fiber breakage during impact. When significant fiber failure occurred, the noise on the load-time signal was more pronounced and could last after the time of maximum load. A similar observation was also reported in (27).

Also shown in Fig. 5.12 is the plate deflection at impact point. It is seen in Fig. 5.12a that the impact event had finished before reverse bending of the plate began. Thus suppressing the reverse bending did not affect the impact event, and it can be assumed that the damage was produced only during impact. In addition, comparing Figs. 5.12a and 5.12b, it is observed that the maximum load remains basically the same for the first and second strikes, but the maximum deflection at the second strike shows a slight increase. The result suggests that the compliance change due to the matrix-controlled damages is relatively small.

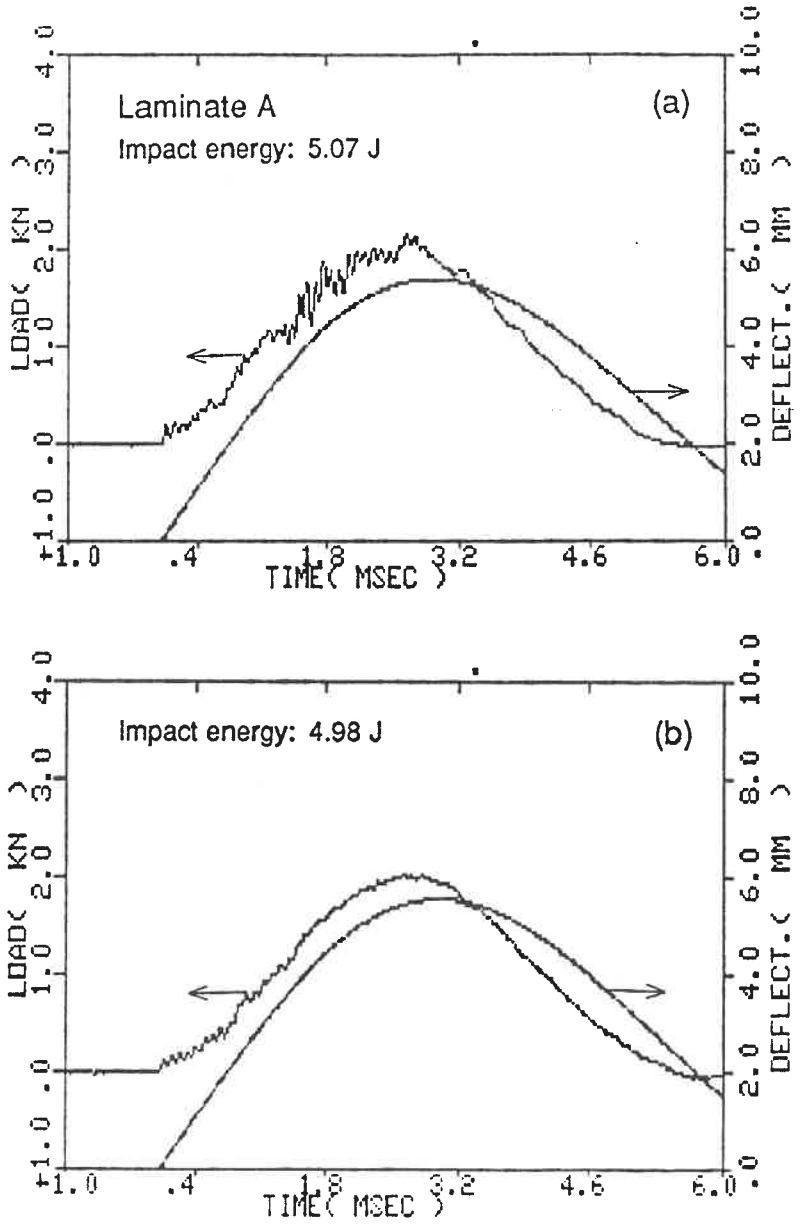

Figure 5.12 Impact force and central deflection of a $[0_5/90_5/0_5]$ PEEK/Carbon (APC-2) laminate: (a) first strike; (b) second strike.

Chapter 6

Impact Stresses and Damage Extension

6.1 Objective

Experimental studies show that impact damage in laminated composites is a dynamic fracture process with multiple damage modes interacting with one another. Simulation of the damage process seems to be inaccessible by the available analysis procedures. Therefore, instead of modeling the damage details, two simple approaches are used in this study to understand the damage growth behavior and its controlling parameters.

In this chapter, the dynamic stress response in intact laminates is considered. The stress field is redistributed at the onset of damage, but it may help to explain the basic features of damage growth. The extension of transverse crack and delamination has been shown to be related to the flexural deformation of the laminate (29, 41). And, in general terms, the damage growth occurs in the region where the nominal stresses are high. However, in principle, only qualitative studies can be made through such analyses.

Later in Chapter 7, the fracture behavior of impact-induced delamination is studied from the view point of fracture mechanics.

6.2 Numerical Model

The impact stress field consists of two parts: the local contact stresses which control the damage initiation, and the plate bending stresses which act in the area of damage growth. For the purpose of the present study, the plate bending stress field was calculated by finite element method. The problem was simulated as a square plate being impacted at its center by a concentrated force. The 9-node shear deformable shell element with reduced integration scheme was used to model the plate. Only the first quadrant of the plate was considered because of symmetry conditions. The measured impact force history was used in the calculation. Linear dynamic stress analysis was performed using the finite element code ABAQUS (80).

In ABAQUS code (version 4.7), the stress or strain output for shell elements is only available at the top and bottom surfaces of the shell. In the present study, a post-processing procedure was developed to determine the stress and strain inside the laminate. According to the laminate theory (81), the in-plane stress and strain can be obtained as

$$\{\sigma\} = [Q]\{\varepsilon\} \tag{6.1}$$

and

$$\{\varepsilon\} = \{\varepsilon^0\} + z\ \{k\} \tag{6.2}$$

where $\{\sigma\} = \{\sigma_x, \sigma_y, \tau_{xy}\}^T$ and $\{\varepsilon\} = \{\varepsilon_x, \varepsilon_y, \gamma_{xy}\}^T$ are the stress and strain vectors respectively. The coordinate system has been defined in Fig. 5.2. $[Q]$ is the lamina stiffness matrix which can be determined from the elastic moduli and Poisson's ratio of the unidirectional composite (81). The midplane strain $\{\varepsilon^0\} = \{\varepsilon_x^0, \varepsilon_y^0, \gamma_{xy}^0\}^T$ and

curvature $\{k\} = \{k_x, k_y, k_{xy}\}^T$ are calculated from the strain components in the top surface $\{\varepsilon^t\}$ and in the bottom surface $\{\varepsilon^b\}$, i.e.

$$\{\varepsilon^0\} = \frac{\{\varepsilon^t\} + \{\varepsilon^b\}}{2} \tag{6.3}$$

$$\{k\} = \frac{\{\varepsilon^t\} - \{\varepsilon^b\}}{h} \tag{6.4}$$

where h is the plate thickness. Although the transverse shear stresses are not included in the formulation of laminate theory, their values can be approximately estimated by integrating the local equilibrium equations through the layer thickness (82). These are

$$\frac{\partial \tau_{xz}}{\partial z} = -\left(\frac{\partial \sigma_x}{\partial x} + \frac{\partial \tau_{xy}}{\partial y}\right) \tag{6.5}$$

$$\frac{\partial \tau_{yz}}{\partial z} = -\left(\frac{\partial \sigma_y}{\partial y} + \frac{\partial \tau_{xy}}{\partial x}\right) \tag{6.6}$$

where τ_{xz} and τ_{yz} are the transverse shear stresses. Since Eqs. 6.5 and 6.6 represent the in-plane equilibrium of a material point which undergoes negligible in-plane movement, both gravity and inertia forces have been dropped in the equations.

Fig. 6.1 shows the 8 by 8 finite element mesh used to model a quarter of the plate. This non-uniform mesh and the stress calculation procedure have been verified against the elasticity solution of Pagano and Hatfield (83). In (83), a simply supported square crossply laminate under sinusoidally distributed static load is considered. The problem was analyzed by the finite element method and the numerical results are compared with the elasticity values. For the A type laminate, as shown in Fig. 6.2,

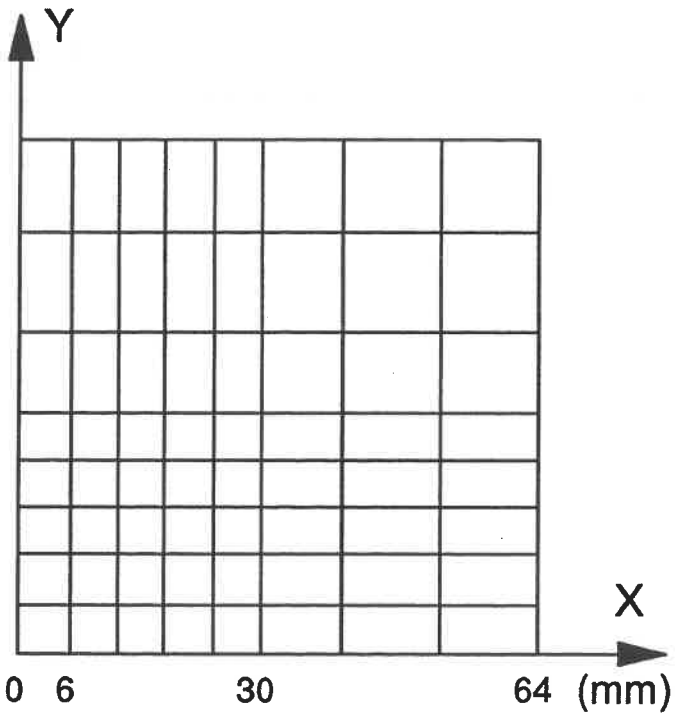

Figure 6.1 Finite element mesh for a quarter of the damage-free laminates.

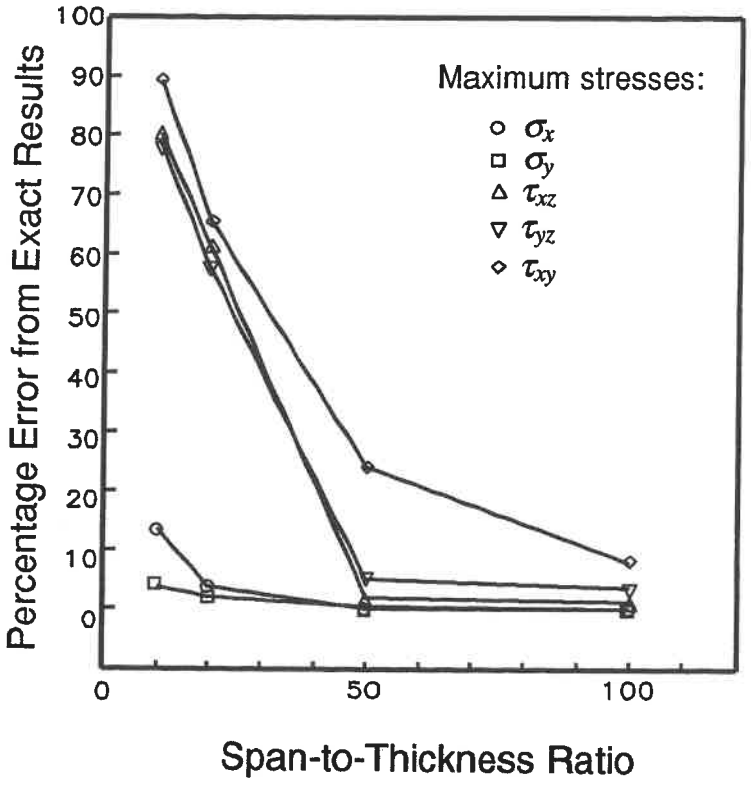

Figure 6.2 Percentage error of finite element analyses compared with elasticity solutions to a three-layer crossply laminate under sinusoid distributed load [83].

precision of the finite element analysis increases with the span-to-thickness ratio of the laminate. At the span-to-thickness ratio of 50, the maximum stresses are within 5% from the elasticity values, except the in-plane shear stress τ_{xy}. While τ_{xy} is a secondary stress in the laminate (83). In the present study, the span-to-thickness ratio is 61. And better accuracy can be achieved in laminates with more than three layers (83), such as in Laminates B and C. Consequently, the 8 by 8 mesh was used to analyze the plate response under local impact load.

The APC-2 composite was assumed to be linear elastic. The material properties in Table 4.1 were used in the dynamic analysis. The thermal residual stresses were calculated using the approach discussed in Chapter 4. As given in Table 6.1, the residual transverse stress in the three crossply laminates is as high as half of the transverse tensile strength of the unidirectional material. The *in situ* lamina strength may be interpolated in Fig. 4.3 from the layer thickness.

Table 6.1 Transverse residual stress in APC-2 crossply laminates.

	Laminate A	Laminate B	Laminate C
0° layer	40	41	41.5
90° layer	42	42	42

6.3 Dynamic Stresses and Transverse Cracking

As discussed in (14), both intralaminar and interlaminar stresses may contribute to producing transverse cracks. Therefore, Harshin's matrix failure criterion (55) was used to define the strength ratio of transverse matrix failure, R_m, in each layer, that is

$$R_m^2 = \frac{\sigma_{22}^2}{\sigma_T^2} + \frac{\tau_{23}^2}{\tau_T^2} + \frac{(\tau_{12}^2 + \tau_{13}^2)}{\tau_{LT}^2} \tag{6.7}$$

where σ_{22}, τ_{12}, τ_{13} and τ_{23} are the stress components, while σ_T, τ_T and τ_{LT} are the lamina strengths, all defined in the material symmetry axes with 1 being the longitudinal fiber direction (L), and 2 and 3 being the in-plane and out-of-plane transverse directions (T) respectively. The material symmetry axes vary from layer to layer with respect to the Cartesian coordinate system defined in Fig. 5.2. The transverse normal stress, σ_{33}, has been omitted in Eq. 6.7 because it rapidly drops to zero away from the contact zone (13, 85). The matrix failure is defined as $R_m = 1.0$.

Consider the extensive 90-degree cracks in Fig. 5.4a (the 2nd layer in Laminate A) and in Fig. 5.4c (the 4th layer in Laminate B). Results of the analyses show that, considering the residual stress and crack constraining effect, no matrix failure would occur in such layers according to Eq. 6.7. The results suggest therefore that the Strength of Material analysis is not an appropriate approach. If the *in situ* lamina strength is arbitrarily reduced to the unidirectional strength of 80 MPa, simulating the loading rate effect on transverse strength (84), the failure region as shown in Fig. 6.3 qualitatively describes the crack distribution in Laminate B but not in Laminate A. Therefore, as expected, the point failure criterion cannot be used to predict the transverse crack extension. In fact, it has been suggested that the crack extension is rather controlled by a dynamic fracture process (35).

6.4 Interlaminar Shear Stresses and Delamination Growth

Away from the impact point, interlaminar shear stresses are the only stresses

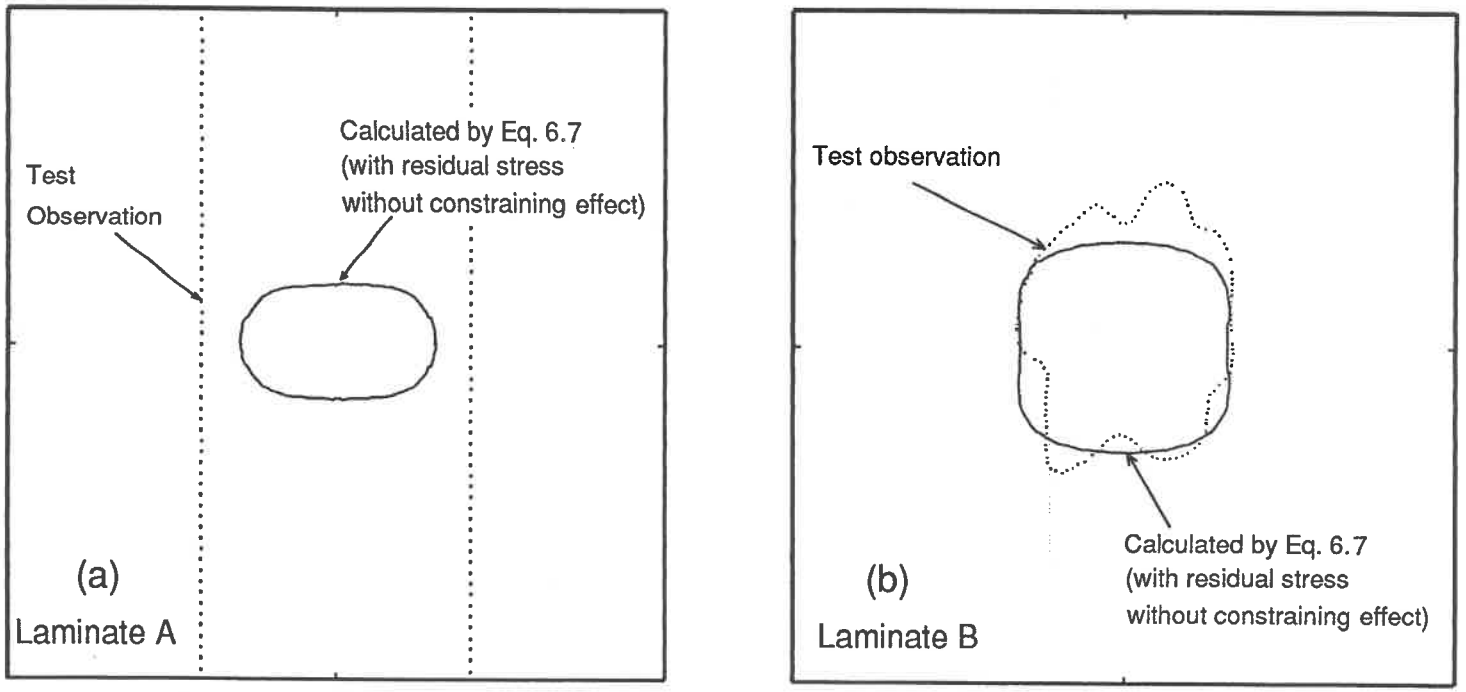

Figure 6.3 Comparison of transverse crack distribution with matrix failure region predicted by the Strength of Materials approach:
(a) 2nd layer, Laminate A, 5 J; (b) 4th layer, Laminate B, 10 J.

acting at the interface(13, 85). The stress distribution may explain some features of the delamination growth. The A type laminate is considered first because of its simple construction. Fig. 6.4 shows the interlaminar shear stress as a vector field at the interface of an A type laminate. The stress field is identical at both interfaces since the contact deformation has been neglected (85). It is seen that the stress field is non-uniform and with a strong directionality. A stress concentration occurs near the impact point. In the region around the x-axis, where $\tau_{yz} = 0$, the stress vectors are more inclined to the x-axis, showing a forward shearing in the x-direction. A similar region with forward shearing in the y-direction exists around the y-axis, where $\tau_{xz} = 0$. Referring to the test observation in Fig. 5.7a, the delaminations at the 2nd and 1st interfaces occurred within these two regions, as well as in the forward shearing directions, respectively. It is thus believed that the delaminations resulted from a Mode II dominated fracture process. This is in agreement with the fractography of the delamination surface as shown in Fig. 5.6.

Fig. 6.5 shows the contour plots of the shear stress components τ_{xz} and τ_{yz} at the time of maximum impact load, for different impact energies respectively. It is found that τ_{xz} possesses much higher values than τ_{yz} over most of the plate area. The high value stress contours of τ_{xz} and τ_{yz} exhibit "peanut shapes" which resemble the delaminations at the 2nd and 1st interfaces respectively. The 1st delamination was initiated from the transverse cracks in the 0-degree upper layer. It propagated in the 90-degree direction under the nominal stress τ_{yz}. Since τ_{yz} decreases rapidly along the crack path, the first delamination was arrested after a short growth. The 2nd delamination, on the other hand, was initiated from the transverse cracks in the middle layer. It propagated in the 0-degree direction, along which τ_{xz} predominates and keeps higher values over a large extension. So a large delamination occurred at the interface.

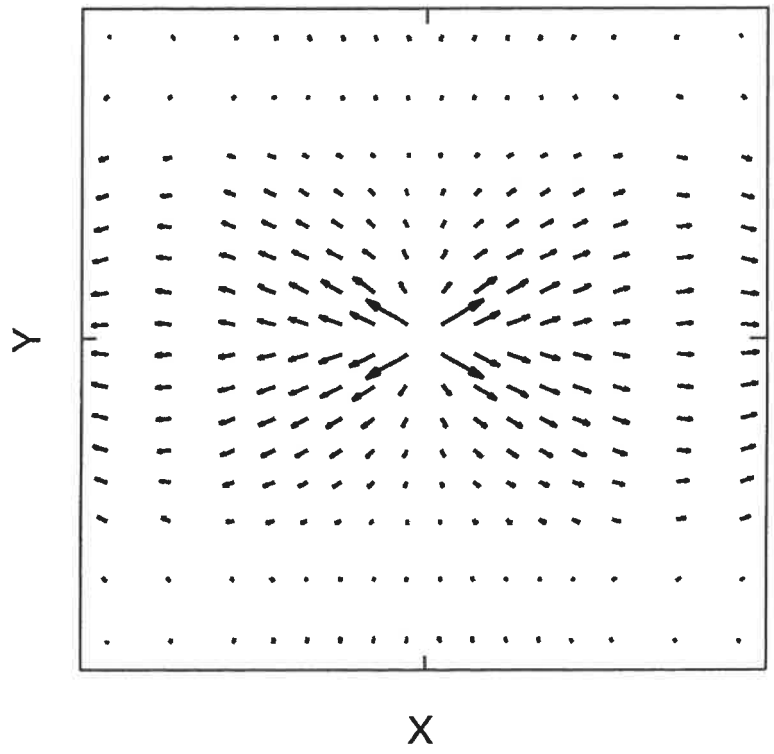

Figure 6.4 Instant distribution of interlaminar shear stress as a vector field. The length of the vector in the plot is scaled by multiplying a factor of: $f = \sqrt{\tau_{max}/\tau}$, where τ is the length of a shear stress vector and τ_{max} is the maximum length among all the vectors.

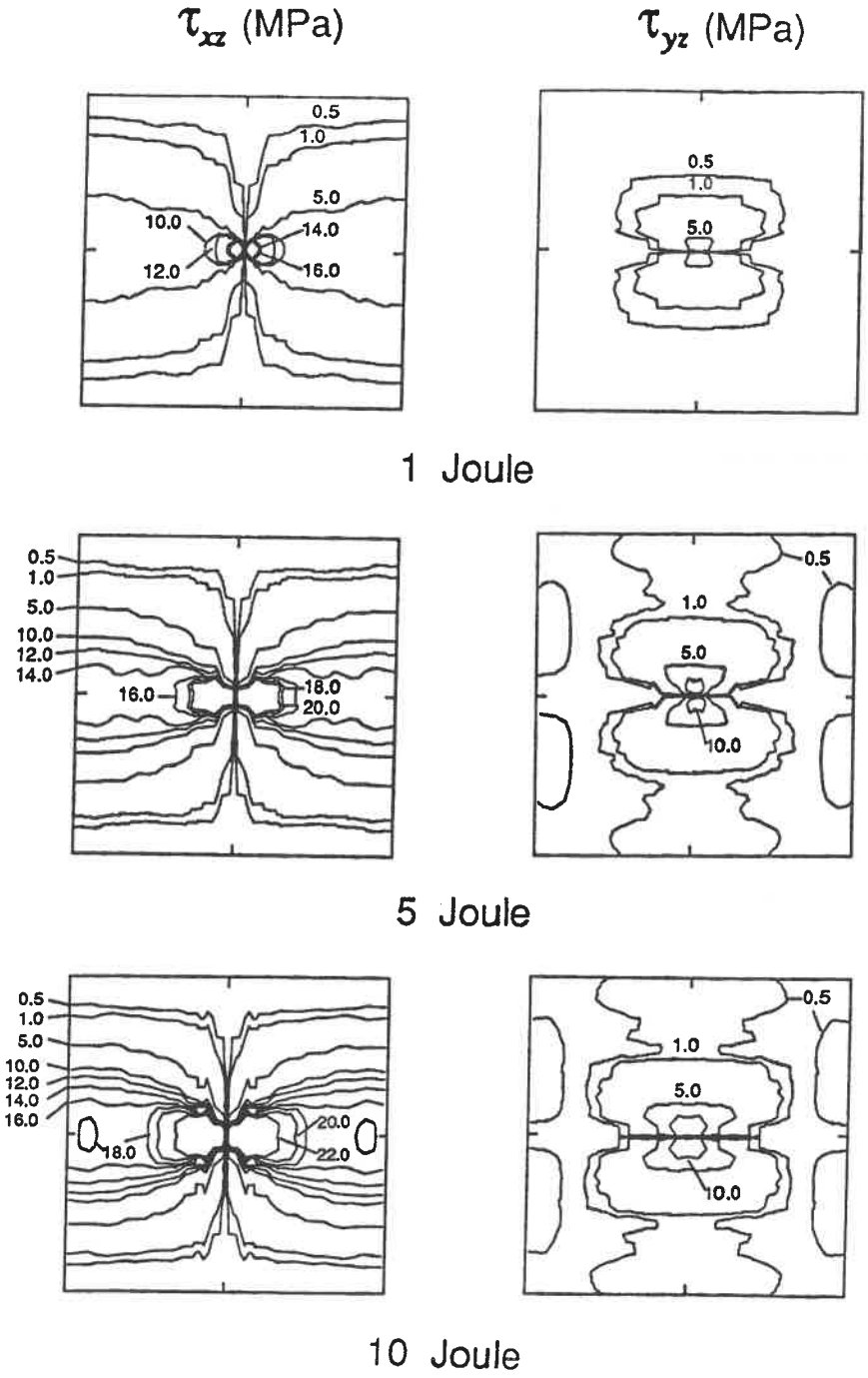

Figure 6.5 Interlaminar shear stress contours in Laminate A at the instant of maximum impact load: (a) 1 J; (b) 5 J; (c) 10 J.

Therefore, the delamination growth depends not only on the interlaminar shear stresses but also on the transverse cracks in the layer above the interface.

It is noted that, in Fig. 5.4a, the 90-degree transverse cracks extended far beyond the width of the second delamination. This means that the delamination was not initiated along the full length of such cracks. Referring to Fig. 6.5b, it seems that the transverse cracks initiated delamination only in the section where τ_{xz} is sufficiently high. This explains the test observation that the delamination width was basically controlled by a crack initiation process.

Based on the discussions in Section 5.3.4, the delamination arrest is assumed to occur at around the maximum impact load. Thus, for comparison purposes only, the 2nd delamination in Laminate A is correlated with the shear stress τ_{xz} contours in Fig. 6.5. The results are presented in Figs. 6.6a and 6.6b for the length L_2 and width W_2 respectively. Within the scatter of test measurements, the arrested delamination sizes appear to correspond to a constant interlaminar shear stress, although the stress values associated with W_2 are somewhat higher than that with L_2. As plotted in Fig. 6.7, the nominal shear stress at delamination arrest seems to be independent of the delamination length. Such observations may possibly explain why some interface failure criteria (16-18) could be used to correlate the measured delamination size. However, as discussed in Chapter 2, the correlation is essentially qualitative, because the interlaminar shear stress field has been redistributed at initiation of the delamination.

Similar analyses have also been conducted for Laminates B and C. The results demonstrate again that the delamination depends on the combination of interlaminar shear stresses and the transverse cracking in the layer above the interface. Figs. 6.8 and 6.9 show the shear stress contours in Laminates B and C at the last interface from the

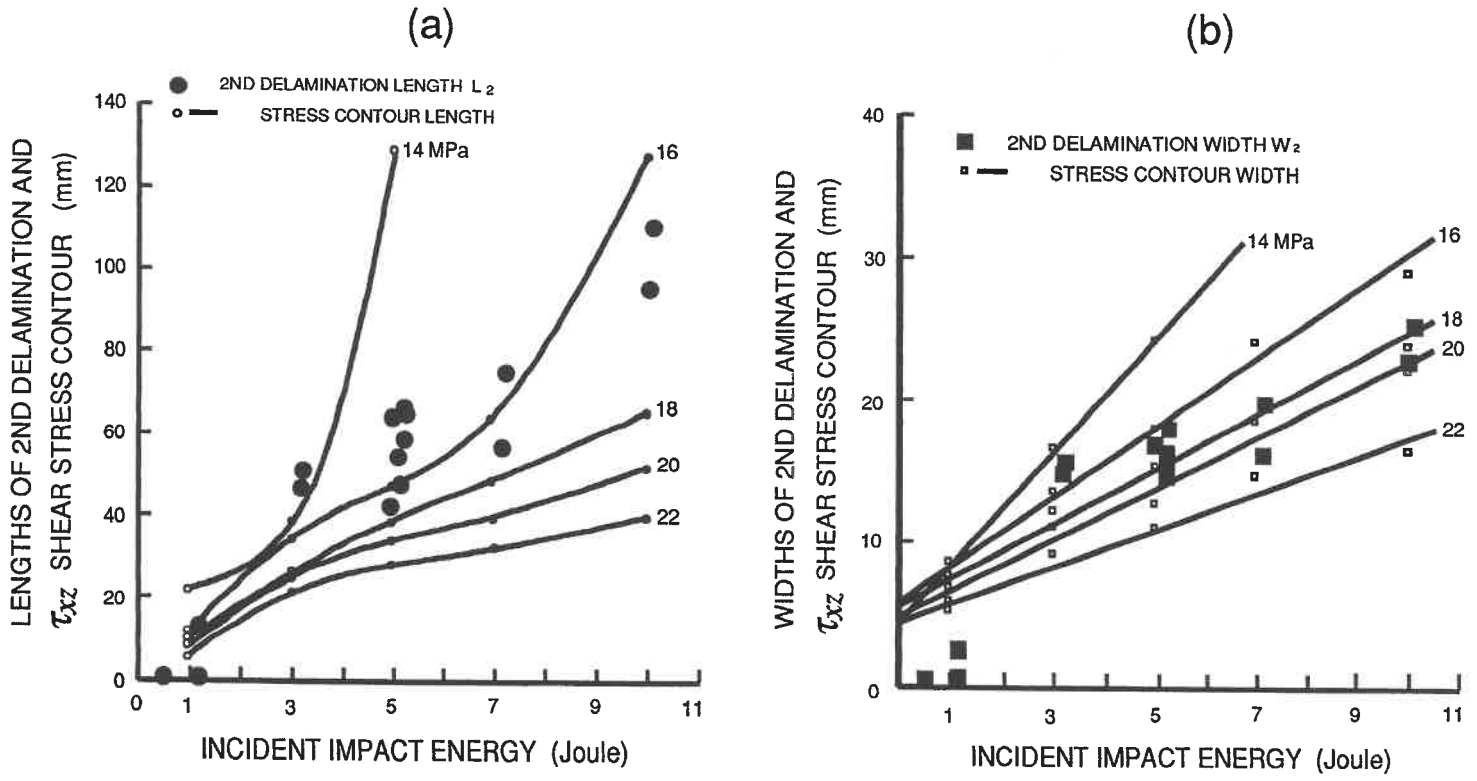

Figure 6.6 Correlation between τ_{xz} stress contour and second interface delamination in Laminate A: (a) length L_2; (b) width W_2.

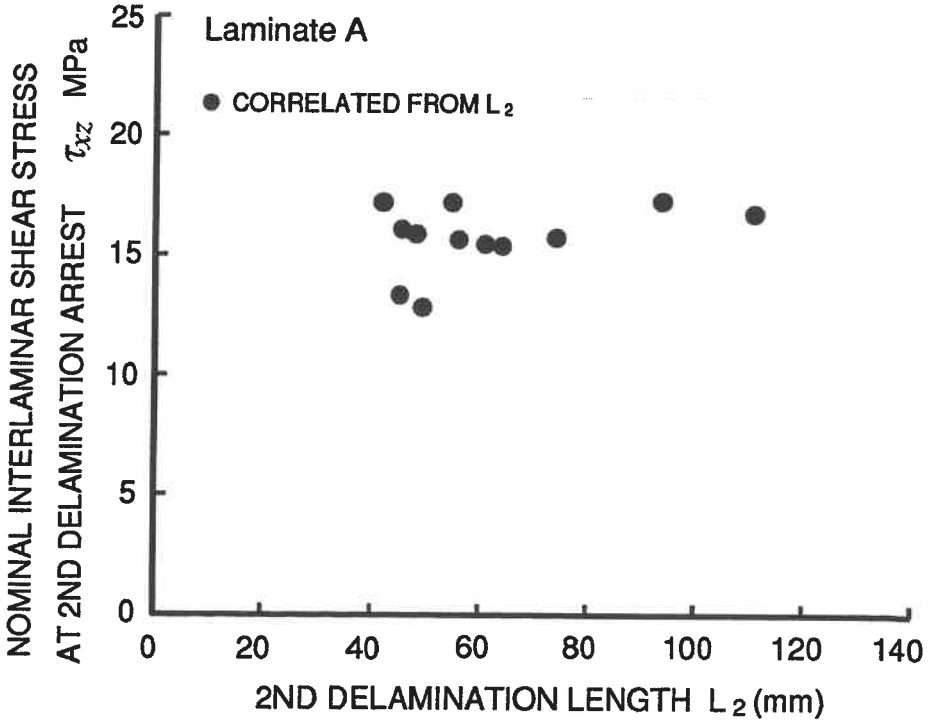

Figure 6.7 Nominal interlaminar shear stress τ_{xz} at the arrested crack front of the second interface delamination in laminate A.

impacted surface. In Laminate B, under 10 J impact, extensive transverse cracks occurred in the 90-degree 4th layer (Fig. 5.4c), so a large delamination resulted from the high τ_{xz} at the last interface. In Laminate C, however, the 10 J impact caused a small amount of matrix failure in the 14th layer, and only a limited delamination occurred due to the low shear stress at the last interface. Higher shear stresses existed near the midplane of the plate but the matrix failure did not occur to initiate the delamination. This combination of crack initiation and crack growth mechanisms explains why delamination is very limited in Laminate C. In fact, the impact produced the "cross crack" in the contact area and the plate began to be penetrated by fiber breakage. The competition between the damage modes is evident in Fig. 5.4e.

It should be noted that, although the correlation between the interlaminar shear stress contours and the delamination geometry verifies the test observation (Fig. 5.6) that the delamination is a Mode II dominated fracture, contributions from other fracture modes may also present. A unique mechanism of mode change has been observed in (50): when the near-surface delaminated region is under flexural compressive stresses during impact, the delaminated plies may buckle locally and cause a Mode I dominated extension of the delamination. Such a mechanism, however, did not act in the present study because reverse bending of the plate has been prevented. However, the Mode I contribution may come from other sources. Previous work (86) has shown that the off-midplane delamination in a flexural beam does not result in a pure Mode II fracture but Mode I is also present. The transverse cracks, on the other hand, may also give rise to a local peeling stress at the crack tips (14). Fig. 6.10 shows the through-the-thickness distribution of the transverse matrix failure region in Laminate B calculated by Eq. 6.7. Since the transverse compressive strength is generally higher than the tensile strength in composite materials (14, 41), little matrix failure occurs above the midplane (on the

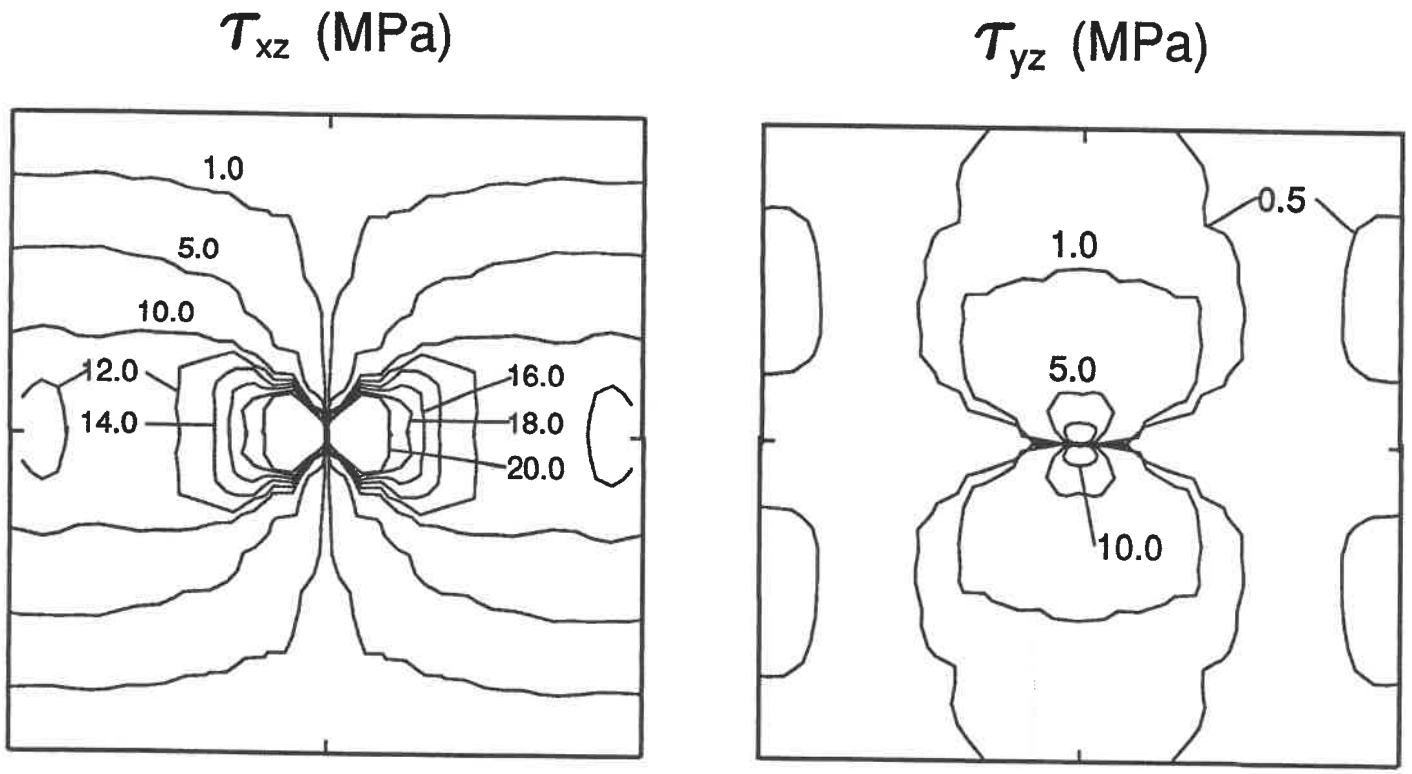

Figure 6.8 Interlaminar shear stress contours at the instant of maximum impact load: the 4th interface, Laminate B, 10 J.

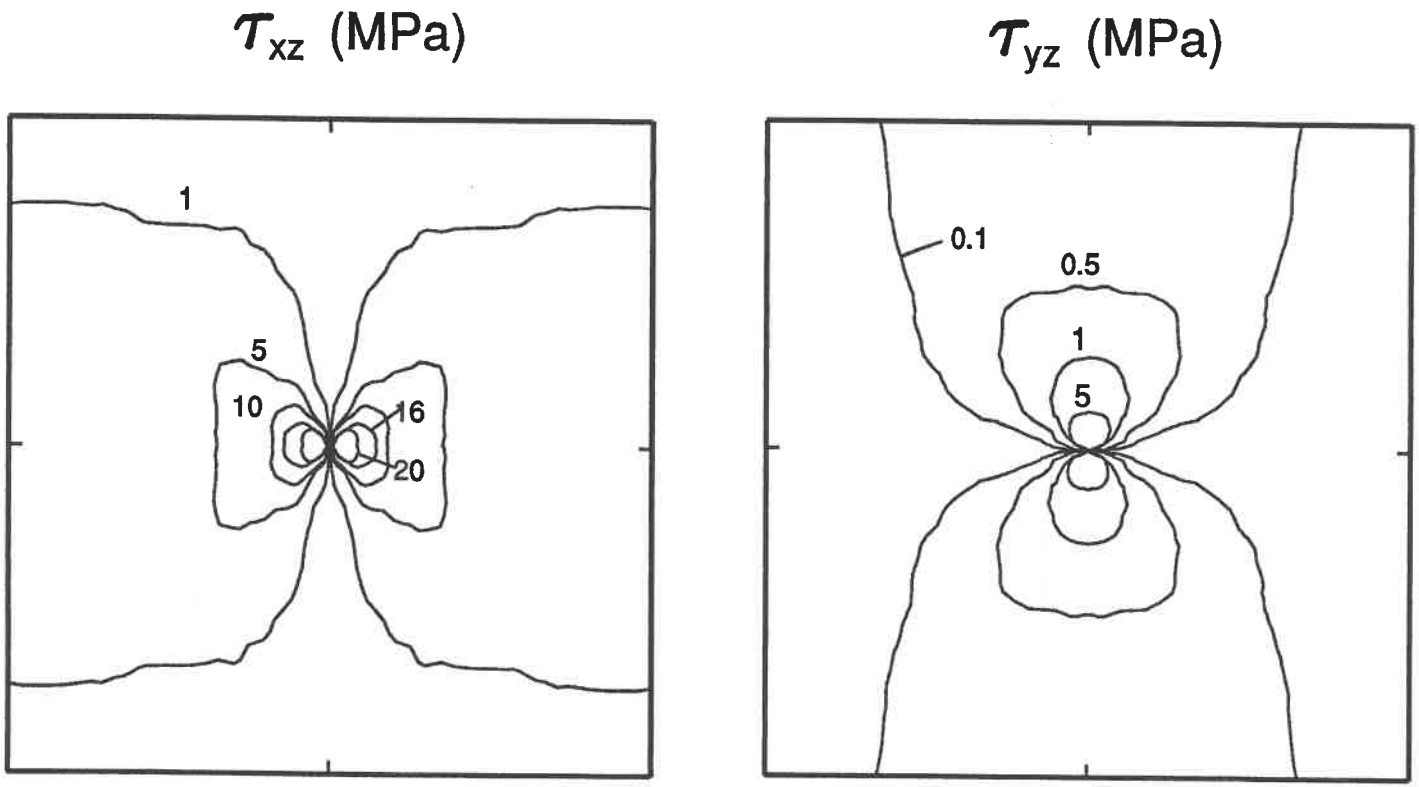

Figure 6.9 Interlaminar shear stress contours at the instant of maximum impact load: the 14th interface, Laminate C, 10 J.

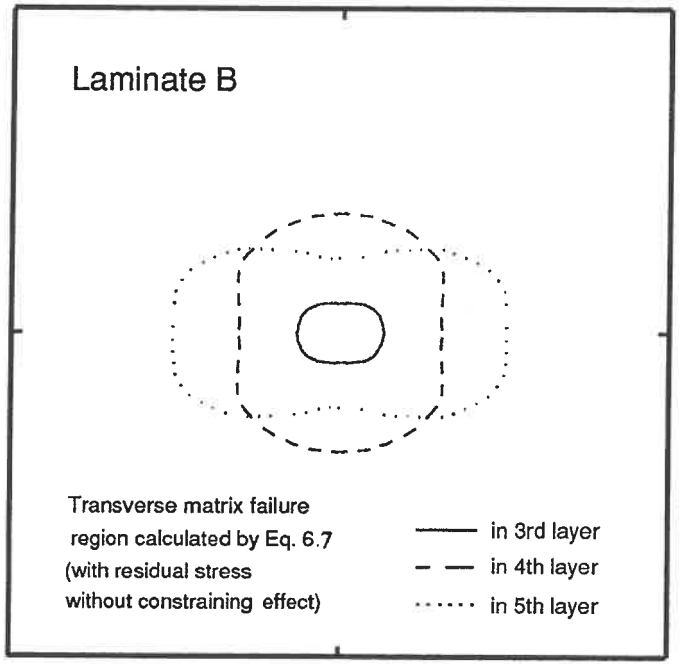

Figure 6.10 Distribution of transverse matrix failure in Laminate B under 10 J impact.

compressive side) except near the impact point (41). The delamination area follows a similar sequence of distribution. This suggests that the delamination area also depends on the transverse cracking which controls the initiation phase of the delamination.

6.5 Impact Response

It has been shown in (26, 27) that the laminate response to drop weight impact is basically quasi-static. Therefore the response could be approximated by a static indentation case (26-28). This point is also verified in the present study. Fig. 6.11 shows the dynamic response of an A type laminate under 5 J impact. The first six vibration modes are plotted in Fig. 6.12. It is seen that, in spite of some inertia effects at the early stage of impact, the plate response is dominated by the low frequency modes. Actually, with the impact duration of 5.44 ms in Fig. 5.12a, the load excitation frequency is 183 Hz, only about one seventh of the natural frequency of the system. Therefore the high vibration modes are hardly excited by the impact. The static problem under the equivalent maximum load of 5 J impact was also analyzed. The interlaminar shear stress, as shown in Fig. 6.13, is close to the dynamic result (Fig. 6.5b).

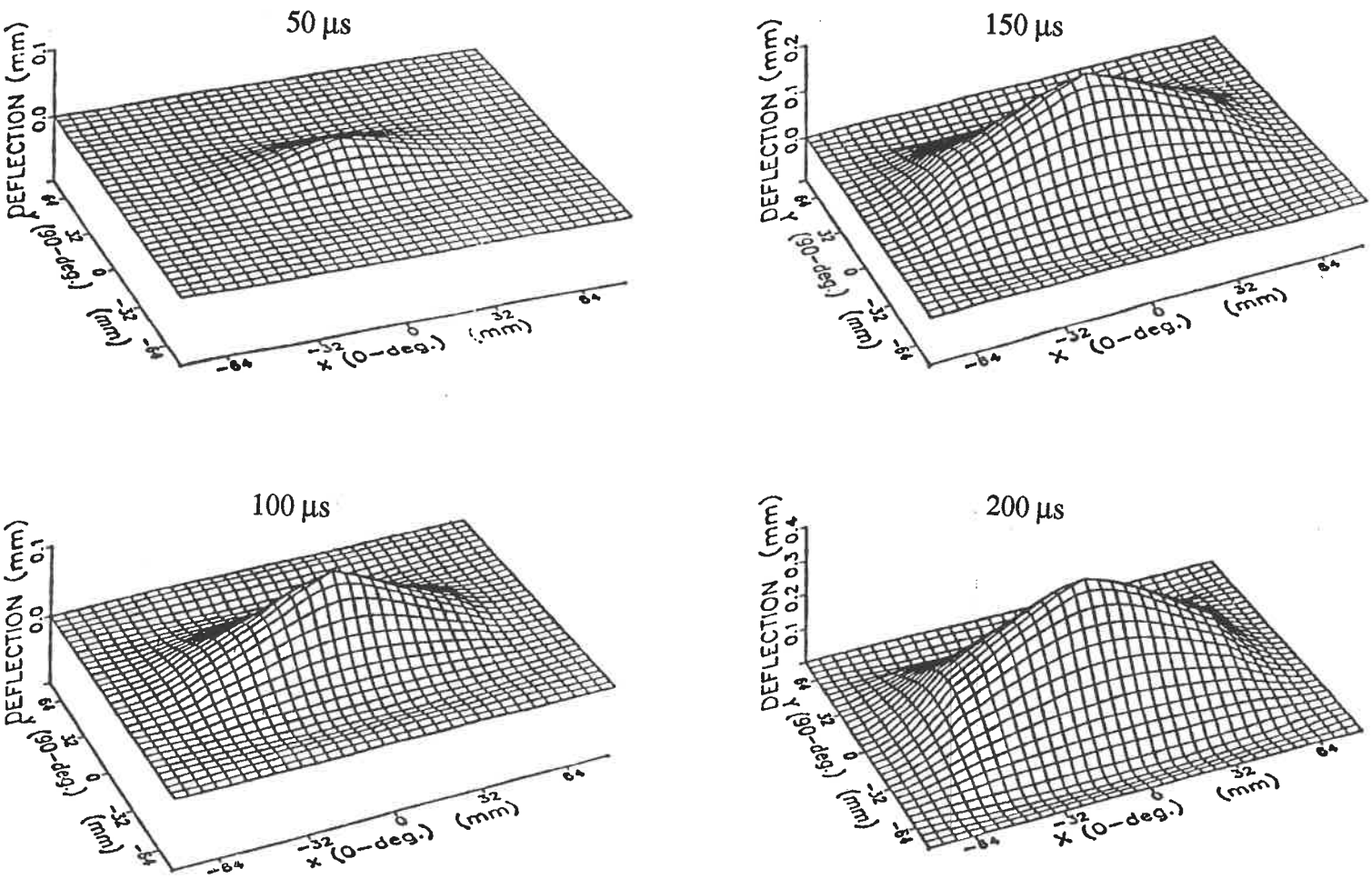

Figure 6.11 Dynamic deflection of an A type laminate under 5 J impact.

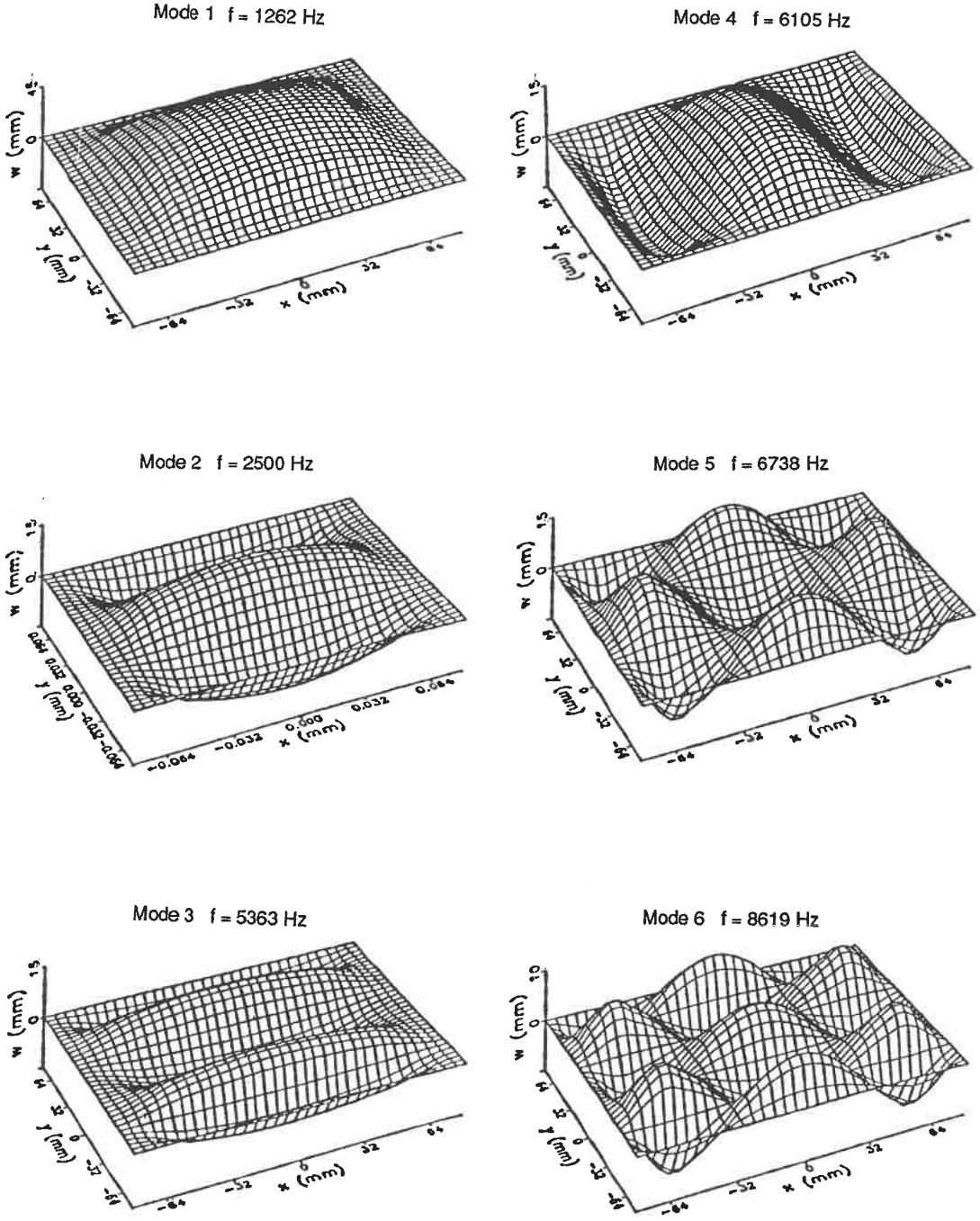

Figure 6.12 First six vibration modes of $[0_5/90_5/0_5]$ laminate. 0-degree fiber direction is along the x-axis.

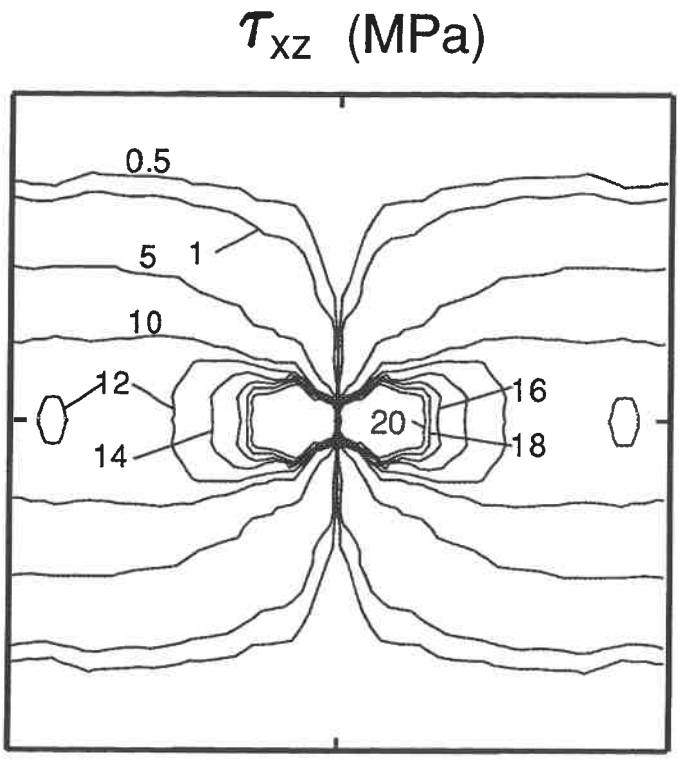

Figure 6.13 Interlaminar shear stress in an A type laminate under static indentation load equivalent to the maximum load of 5 J impact.

Chapter 7

Fracture Behavior of Impact-Induced Delamination

7.1 Objective

Physically, the impact-induced delamination results from a dynamic fracture process. The fracture behavior cannot be predicted by the Strength of Materials approach discussed in Chapter 6. It is so far not clear what mechanics parameters and material properties actually control the delamination extension in impacted laminates.

In the present chapter, the crack growth behavior of impact-induced delamination is studied from the viewpoint of fracture mechanics. Prediction of the delamination size is discussed based on the concept of crack arrest toughness. Since the delamination associated with transverse crack is the dominant damage mode in Laminates A and B, the two laminate types are considered in this chapter.

7.2 Fracture Mechanics Approach

Since the delamination is a process of unstable crack growth and subsequent

arrest, the fracture mechanics concept of crack arrest (59) might be used to characterize the delamination extension. Previous studies on impact fracture of polymers and composites (35, 50, 87, 88) have shown that the crack speed during unstable fracture is much higher than the impactor speed. So the crack growth generally occurs in a fixed-displacement condition and the energy available for crack growth is the elastic energy stored in the specimen (87, 88). Consequently, the strain energy release rate, G, of an impact-induced delamination may be expressed in the deflection-controlled form:

$$G = \frac{1}{2}\frac{\delta^2}{C^2}\frac{dC}{dA} \tag{7.1}$$

where δ is the load-point deflection, C is the flexural compliance and A is the delamination area. In Eq. 7.1, the laminate is assumed to be linear elastic and the effect of kinetic energy is neglected for the case of low velocity impact.

From the viewpoint of energy balance (59), the delamination growth depends on the variation of G. When G is higher than the material toughness, the delamination grows in an unstable manner. Such a growth will continue until G drops to a critical value, i.e., the delamination arrest toughness of the material. At this point, for additional crack extension, the energy released by the system is insufficient to create new fracture surfaces and the delamination growth stops. Therefore, under a given impact condition, the delamination size should be controlled by the delamination arrest toughness, G_{arr}, which may be determined from Eq. 7.1 at the instant of delamination arrest, i.e.

$$G_{arr} = \frac{1}{2}\frac{\delta_{arr}^2}{C^2}\frac{dC}{dA} \tag{7.2}$$

where δ_{arr} is the plate deflection at delamination arrest. The validity of such a criterion depends on the existence of G_{arr}, which represents the material resistance to a running crack and should be independent of the laminate type and the delamination size.

The above viewpoint was first proposed in (22-25). In order to verify the delamination arrest criterion for the laminates studied, it is important to determine the plate deflection at delamination arrest δ_{arr}, the flexural compliance C and dC/dA. The crack growth pattern at delamination arrest should also be defined.

7.3 Crack Growth Pattern at Delamination Arrest

Eqs. 7.1 and 7.2 assume that a dominant crack exists in the laminate. So the largest delamination in both A and B type laminates is considered, which is hereafter referred to as the major delamination of the plate.

As discussed earlier, the delamination width is controlled by a process of crack initiation and the length by the unstable crack growth and subsequent arrest. Fig. 5.8 shows that the major delamination length in both laminates increases rapidly with impact energy while the width varies only slightly. The other delamination(s), at the other interface(s), is (are) smaller in size and varies (vary) only slightly with impact energy. Considering the variations of transverse crack distribution in Figs. 5.10 and 5.11 as well, the major delamination length seems to be the dominant variable of the damage state in both laminates.

As shown in Fig. 5.7a, the delaminations in Laminate A are similar to that in the impacted $[0_5/90_5/0_5]$ Glass/Epoxy laminate (35). High-speed photography of the damage process (35) revealed that the first interface delamination was arrested earlier

than the second one. Since the crack growth is governed by the variation of G which, as shown later, depends on the laminate construction, the same sequence of delamination arrest can be expected in Laminate A. The extensive transverse cracks also occur early during impact (35-38). Therefore it is appropriate to assume that the major delamination in Laminate A is the last damage mode to be arrested in the damage process. One exception to this assumption may be the short transverse cracks that are associated with the delamination growth. These cracks, however, are considered secondary in terms of the small energy absorption involved. A similar damage sequence is also assumed in Laminate B.

With the above discussions, the major delamination growth just before arrest can be defined by considering the delamination geometry in Fig. 5.7 and the size variations in Fig. 5.8. From Fig. 5.7, the major delamination in both laminates may be approximated by an ellipse in which the major and minor axes correspond to the length (L) and width (W) of the delamination respectively. The delamination area is thus $A = \pi WL/4$. From Fig. 5.8, the delamination length increases rapidly with impact energy while the width varies only slightly. Thus the width may be assumed to be constant. This implies the crack growth in the form:

$$dA = \frac{\pi}{4} \overline{W}\, dL \tag{7.3}$$

where $\overline{W}$ denotes the average width of the major delamination. The other damage modes, which terminated earlier than the major delamination, are not included in Eq. 7.3.

7.4 Plate Deflection at Delamination Arrest

From the impact force record such as that in Fig. 5.12a, it seems appropriate to assume that the major delamination is arrested at around the time of maximum impact load. So the maximum load and the deflection at that moment might be associated with the crack arrest. However, during the unstable fracture, the plate deflection is almost fixed and the stored elastic energy is consumed by crack extension. Hence, theoretically, the load must drop due to sudden increase in compliance. So the load at delamination arrest should be lower than the maximum load. In the present study, the delamination arrest is assumed to occur just before the maximum load, as the damage-related noise in Fig. 5.12a indicates. So the deflection at maximum load, δ_{pmax}, is considered to approximate the deflection at delamination arrest, i.e.

$$\delta_{arr} \approx \delta_{pmax} \tag{7.4}$$

Fig. 7.1 plots δ_{pmax} against the major delamination length in both A and B type laminates. The test data represent the damage state with negligible fiber breakage. It is seen that the delamination is initiated at a critical plate deflection. And the major delamination length increases linearly with δ_{pmax}.

7.5 Post-Impact Flexural Compliance

The flexural compliance has been measured on part of the impacted laminates (the second set of specimens as defined in Chapter 5). Fig. 7.2 plots the post-impact

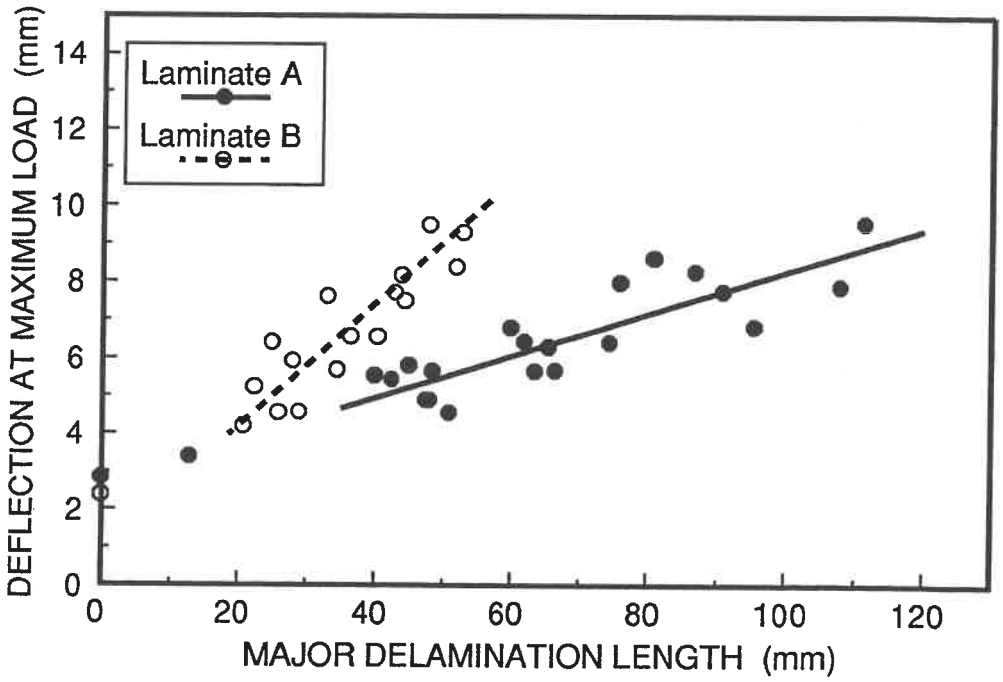

Figure 7.1 Central deflection at maximum impact load versus length of major delamination.

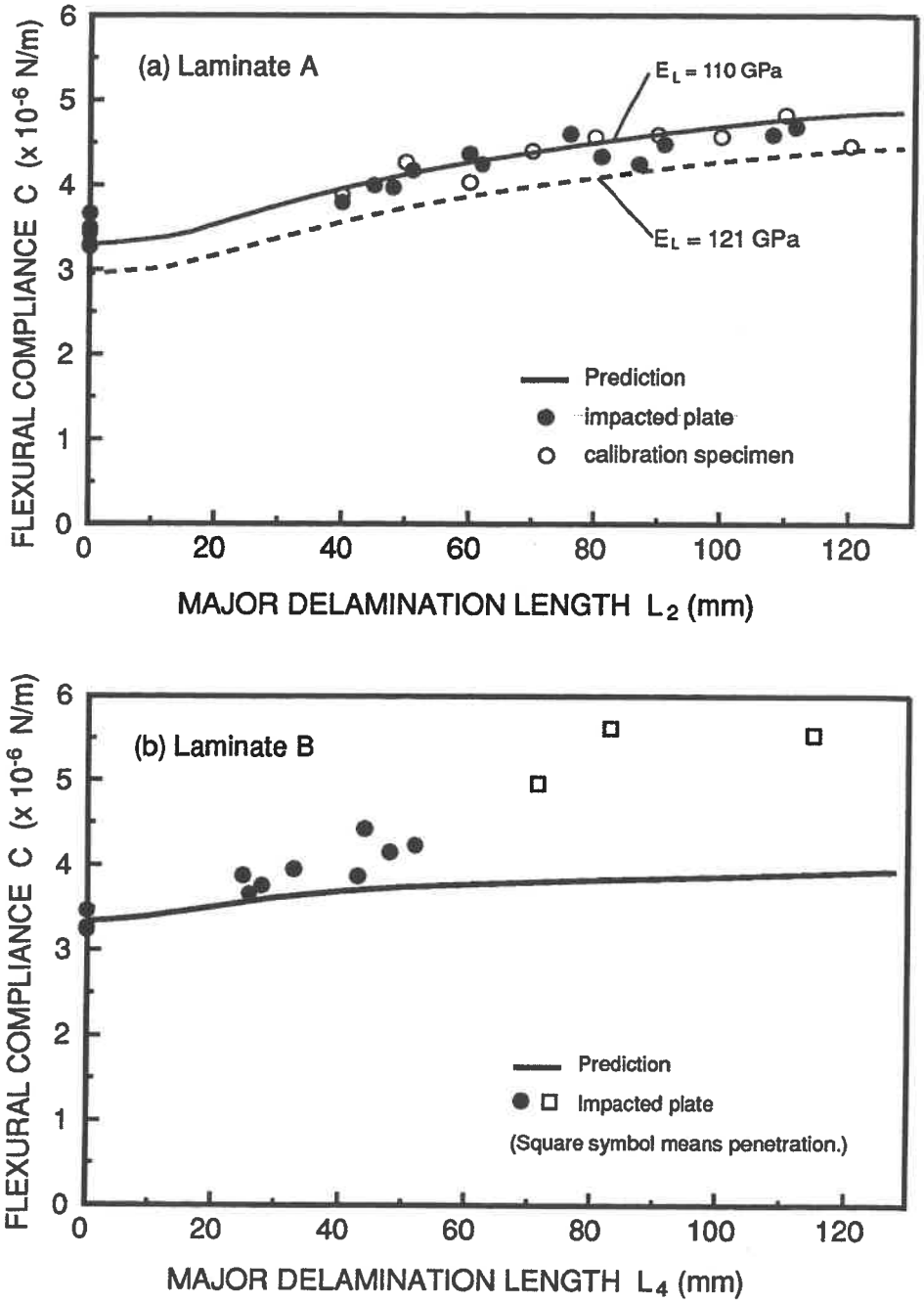

Figure 7.2 Flexural compliance versus length of major delamination: (a) Laminate A; (b) Laminate B.

compliance versus the major delamination length in Laminates A and B. The compliance change due to damage is relatively small when the damage is limited to delaminations and transverse cracks.

7.6 G_{arr} from Test Data

Evaluation of G_{arr} by Eqs. 7.2 and 7.3 requires determination of dC/dL. This could be done by test calibration or by stress analysis (59). A simple correlation of the test data is considered first. It is believed by intuition that the measured relationship between the delamination size and the level of impact should reveal some information about the material resistance to the delamination extension.

Consider the damage state in Laminate A. The major delamination is much larger than the other damage modes, and the delamination area is governed by the delamination length L_2. Therefore, the compliance change in Fig. 7.2a may be approximately attributed to the variation in L_2. As a verification, some A type laminates were fabricated containing an artificial delamination with W_2 = 17.5 mm and a varying L_2. The delamination was made by inserting two layers of Kapton film at the interface during laying up. As shown in Fig. 7.2a, the calibration specimens exhibit the same range of compliance as the impacted plates.

The increase of delamination size with impact level has been given by the L_2 vs δ_{pmax} relation in Fig. 7.1. The linear variation may be expressed in the form

$$\delta_{pmax} = aL_2 + b \tag{7.5}$$

where a and b are the regression constants. For the A type laminates in Fig. 7.1, a = 0.0562 and b = 2.6723 mm (correlation coefficient = 0.81). If such a variation can be characterized by the delamination arrest criterion in Eq. 7.2 with a constant G_{arr}, Eq. 7.2 may be integrated for compliance C to give

$$\frac{1}{C} = \frac{\pi \overline{W}_2 G_{arr}}{2a\,(aL_2 + b)} + \lambda \tag{7.6}$$

where $\overline{W}_2$ = 17.5 mm is the average width of the major delamination and λ is an integration constant. The variation of C by Eq. 7.6 can be correlated to the measured compliance in Fig. 7.2 in order to verify the assumed independence of G_{arr} on the delamination length, and, if so, to determine the value of G_{arr} by regression.

Multiplying both sides of Eq. 7.6 by Eq. 7.5 yields

$$\frac{\delta_{arr}}{C} = \lambda a L_2 + \lambda b + \frac{\pi \overline{W}_2 G_{arr}}{2a} \tag{7.7}$$

Hence, if G_{arr} is a constant, δ_{arr}/C should vary linearly with L_2. This is verified by the test data as plotted in Fig. 7.3. Linear regression of the test data gives

$$\frac{\delta_{arr}}{C} = \alpha L_2 + \beta \tag{7.8}$$

where α = 0.0096 kN/mm and β = 0.9354 kN are the regression constants (correlation coefficient = 0.68). Consequently, G_{arr} seems to be independent of the delamination size and can be determined from Eqs. 7.7 and 7.8 as

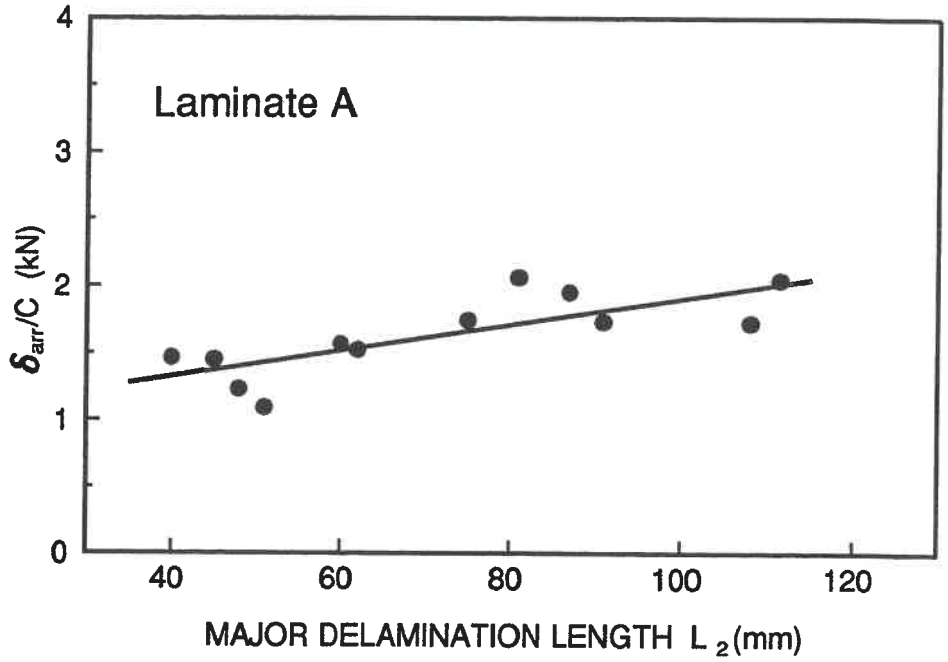

Figure 7.3 Variation of δ_{arr}/C versus delamination length L_2 in Laminate A.

$$G_{arr} = \frac{2(a\beta - b\alpha)}{\pi \overline{W}_2} \tag{7.9}$$

From the regression constants, it is found that G_{arr} = 0.98 kJ/m^2 in the A type laminate.

7.7 Finite Element Analysis

The fracture mechanics analysis based on test calibration of the compliance versus crack length relation needs to be verified. Since the compliance change due to delamination growth is relatively small, the scatter in compliance measurement may cause error in the analysis. As suggested in (89), the hybrid theory/experiment approach could be used to improve the analysis. The basic feature of the approach is to determine the compliance variation by stress analysis. So *dC/dA* in Eqs. 7.1 and 7.2 may be determined. The analytically (or numerically) determined *dC/dA* is then combined with test data to perform the fracture analysis. In the present study, finite element method is used to calculate *dC/dL* in the damaged laminates. The damage state is simplified in order to take into account the other damage modes which terminated before the major delamination arrest.

Fig. 7.4 illustrates the damage state in Laminate A as observed in test and modeled by finite element method. The simplified damage state consists of the delaminations at both interfaces, the transverse crack region in the middle layer, and the central transverse crack in the bottom layer. The local damage in the (impacted) upper layer is neglected. Rectangular delaminations are assumed in order to model the

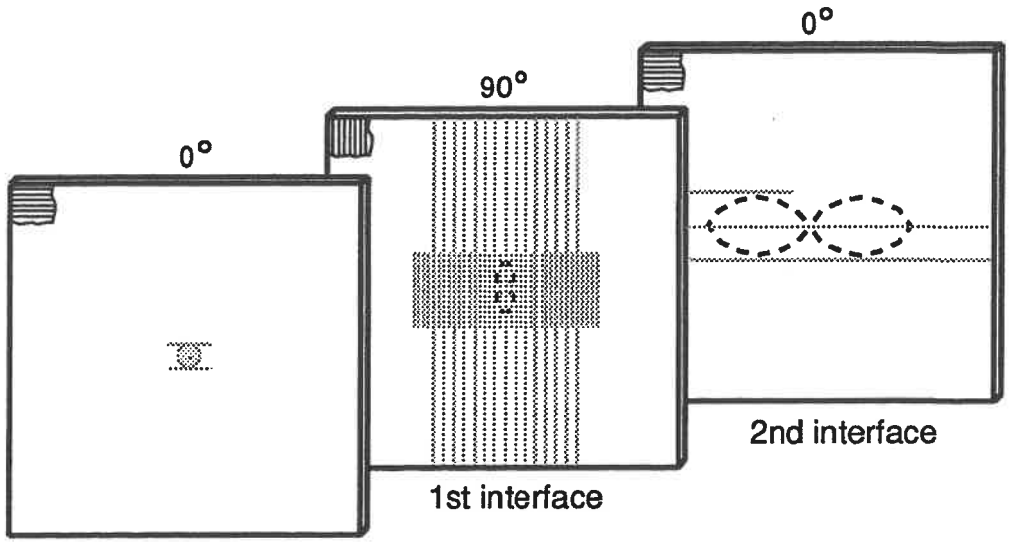

(a) Observation

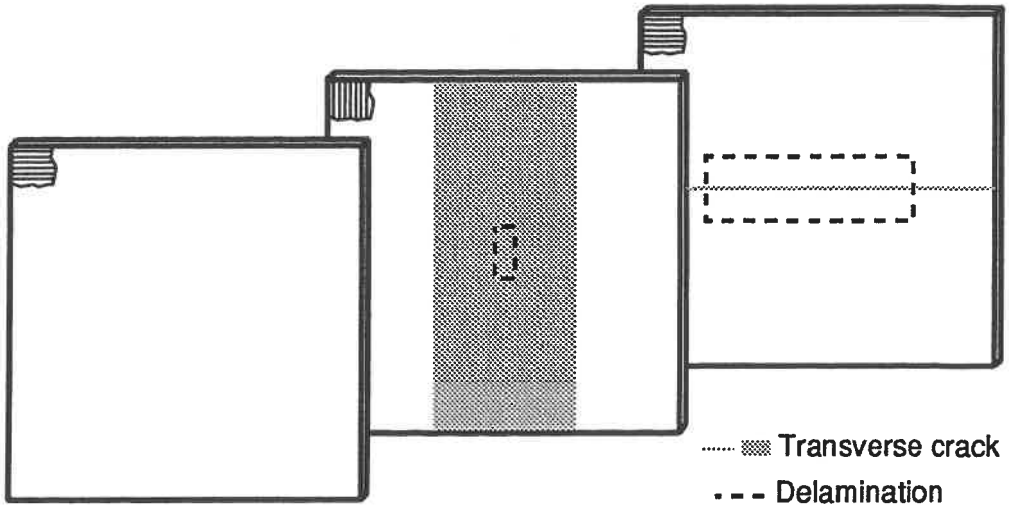

(b) Model

Figure 7.4 Simplification of damage state in A type laminate for finite element analysis.

multiple delaminations. The transverse crack region is approximated by a cross-span strip. Sizes of such damages may be determined from test measurements in Figs. 5.8a and 5.10. However, since the major delamination length is the dominant variable of the damage state, the damage state can be modeled by varying L_2 while approximating the other damages by their average sizes. The following dimensions are assumed in the model: the major delamination width W_2 = 17.5 mm, the first delamination length L_1 = 17.5 mm and width W_1 = 5 mm, and the width of the transverse crack region D_2 = 38 mm.

The damage in Laminate B is simplified in a similar manner. It consists of the delaminations at the 2nd, 3rd and 4th interfaces, the transverse crack region in the 4th layer, and the central transverse crack in the 5th layer. The transverse crack region is assumed to be a rectangular area. The major delamination length L_4 is assumed to be the only variable in the model. Based on the test measurements in Fig. 5.8b, the following sizes are assumed for the other delaminations: $W_4 = L_2 = W_2 = L_3 = W_3$ = 14 mm. The length and width of the transverse crack region in the 4th layer are taken to be H_4 = 33 mm and D_4 = 50 mm respectively.

Finite element model of the damaged laminates can be constructed using plate bending element and the multi-point constraint (MPC) technique (65, 90). Accordingly, every layer of the laminate is modeled by plate elements using the same mesh for all the layers. The displacements of adjacent nodes between the layers are constrained by a set of MPC equations so as to guarantee the deformation assumptions made in laminate theory. These assumptions include:

1) The plane section remains plane during deformation, i.e.

$$u^i = u^0 + z^i \, \theta_y^0 \tag{7.10}$$

$$v^i = v^0 - z^i \theta_x^0 \tag{7.11}$$

$$\theta_x^i = \theta_x^0 \tag{7.12}$$

$$\theta_y^i = \theta_y^0 \tag{7.13}$$

2) No deformation occurs in the thickness direction:

$$w^i = w^0 \tag{7.14}$$

where (u^0, v^0, w^0) and (θ_x^0, θ_y^0) are the midplane displacements and rotations of the reference layer respectively. While (u^i, v^i, w^i) and (θ_x^i, θ_y^i) are respectively the displacements and rotations of the i-th layer at position z^i from the midplane of the reference layer. The middle layer in Laminate A and the 3rd layer in Laminate B are used as the reference layers.

In the delaminated region at the interface, the above constraints are replaced by interface elements to simulate the delamination. The interface element allows the relative sliding and separating displacements of the layers at both sides of the delamination, and prevents them from penetrating each other.

The single transverse crack in the model is simulated by setting free the related degrees of freedom in the layer at positions where the crack occurs. The transverse crack region is modeled using the modulus degradation approach (91). Since the layer containing dense transverse cracks contributes negligible stiffness in the transverse direction to the laminate, it is assumed in such a layer that $E_T \approx 0$ and $\nu_{LT} \approx 0$, where E_T and ν_{LT} are the transverse Young's modulus and Poisson's ratio respectively. The

longitudinal modulus E_L and in-plane shear modulus G_{LT} remain unchanged. The following material properties have been used in the calculation: $E_L = 110\ GPa$, $E_T = 8.9\ GPa$, $G_{LT} = 5.1\ GPa$ and $\nu_{LT} = 0.29$.

The finite element analyses were conducted using ABAQUS code. Flexural compliance of the plate under central indentation load was determined by dividing the predicted deflection with the given load value. Only one quadrant of the plate was modeled because of symmetry considerations. One of the typical meshes used in the calculation is shown in Fig. 7.5a. This 11×11 mesh has been verified by predicting the deflection of intact laminates under sinusoidal distributed load, to which the exact solution is available (83). The prediction is within 4% from the exact value. A mesh refinement study has also been conducted for the damaged laminate under central indentation load. As shown in Fig. 7.5b, the flexural compliance converges rapidly with mesh refinement. The computation cost also increases sharply due to the iterations required for the contact problem.

The predicted compliance is shown in Fig. 7.2 for comparison with the test data. The predicted compliance seems to reasonably agree with the measured data in Laminate A, but to underestimate the measurements in Laminate B at larger delamination sizes. The damage state in Laminate B, which becomes more localized at higher impact energies, may be more severe than the simplified model. Nevertheless the predicted compliance curve reproduces the basic variation in test data of both laminates. Therefore, *dC/dL* is determined from the predicted compliance curve. The numerical *dC/dL* is plotted in Fig. 7.6 as a function of the major delamination length. In spite of a similar tendency in variation in both laminates, *dC/dL* seems to depend on the laminate construction.

It should be noted that the flexural modulus of $E_L = 110\ GPa$ has been used in

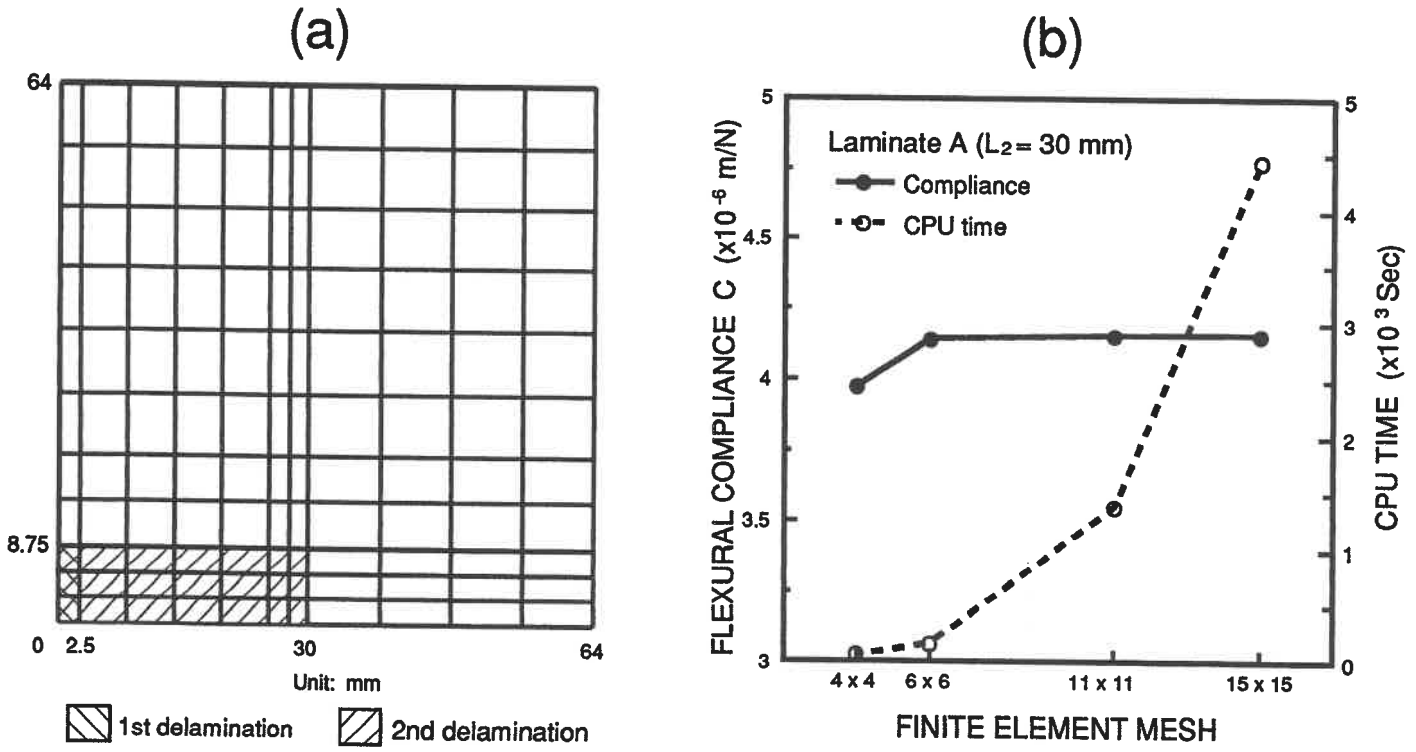

Figure 7.5 Finite element model of damaged A type laminate: (a) mesh for a quarter of the laminate; (b) mesh refinement study.

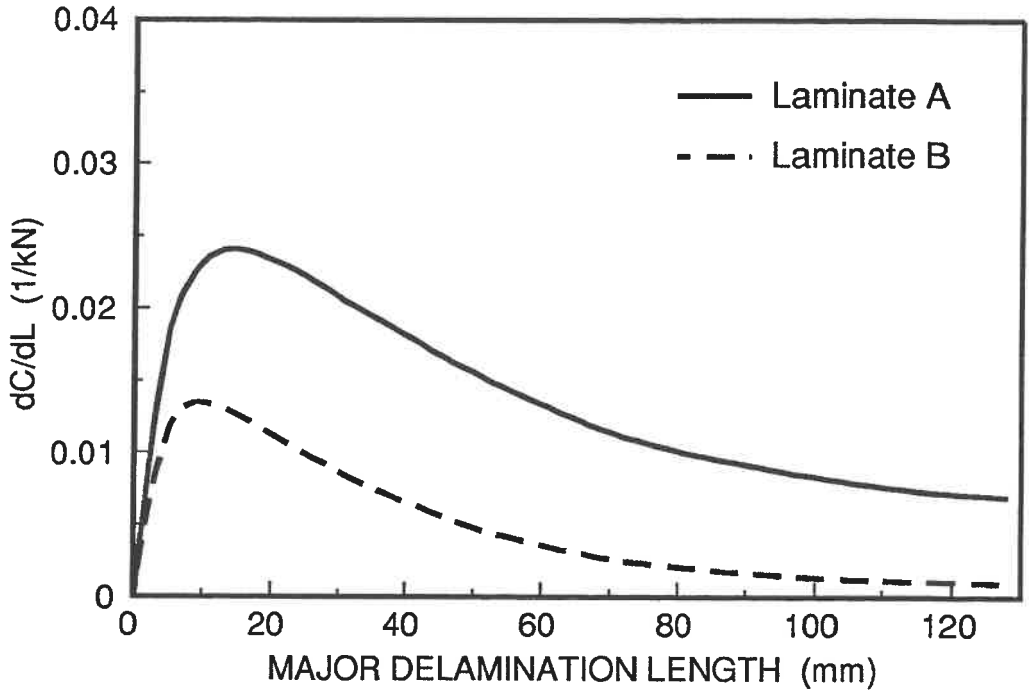

Figure 7.6 *dC/dL* determined by finite element analysis in A and B type laminates.

the calculation, instead of $E_L = 121\ GPa$ as measured from unidirectional beam specimens (75). Actually, the layer modulus in the fiber direction depends on the loading condition the layer is subjected to. The *in situ* layer modulus in the laminate under central indentation load is unknown. As shown in Fig. 7.2a, using $E_L = 121\ GPa$ results in underestimate of the flexural compliance. In the present study, an equivalent E_L was determined by correlating the predicted compliance with the measured data for intact laminates. $E_L = 110\ GPa$ was found to give good correlation in both A and B type laminates.

7.8 Delamination Arrest Criterion

According to the hybrid theory/experiment approach (89), the numerical *dC/dL* in Fig. 7.6 may be combined with test data to determine the delamination arrest toughness. Fig. 7.7 shows G_{arr} as a function of the arrested delamination length. G_{arr} was calculated from Eq. 7.2 using the measured compliance and the numerical *dC/dL*. For the two laminates and the limited test data obtained, G_{arr} seems to be relatively constant regardless of the delamination size. G_{arr} is about 1 kJ/m^2, verifying the value obtained in Section 7.6. A scatter between 0.5 and 1.5 kJ/m^2 is observed. The scatter may come from the measurements of C and δ_{arr}, and from the dynamic effects during impact test. A similar scatter has also been observed in measuring the Mode II delamination arrest toughness of Glass/Epoxy composite (72).

In order to evaluate the delamination arrest criterion, Eq. 7.2 may be converted into the following form:

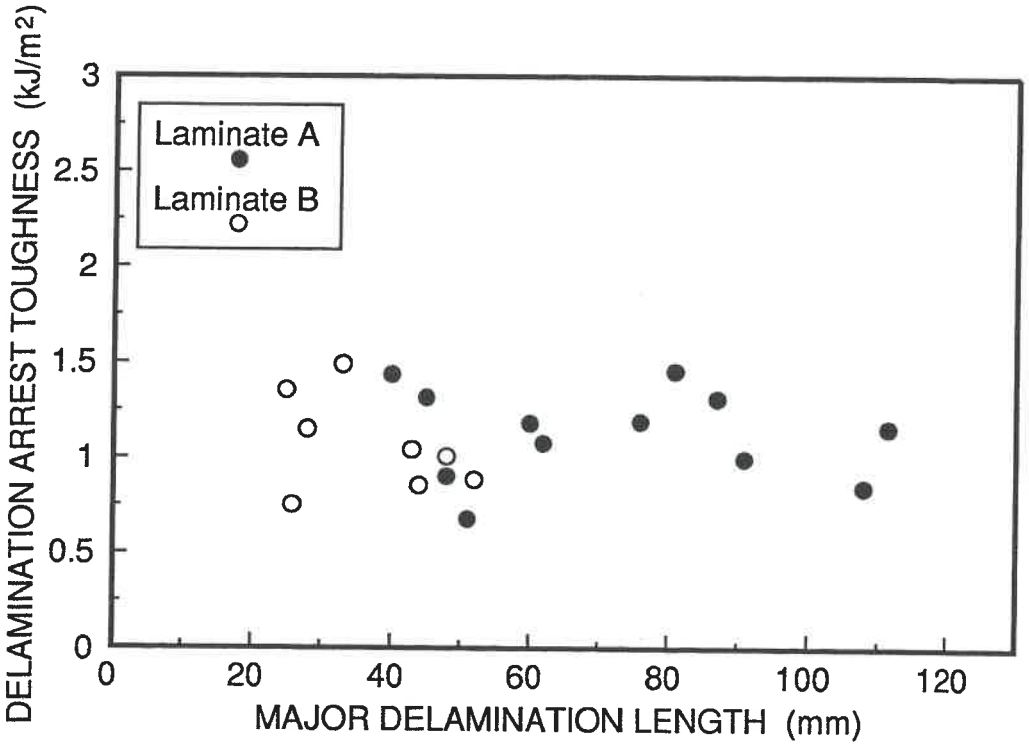

Figure 7.7 Delamination arrest toughness G_{arr} versus major delamination length in A and B type laminates.

$$\delta_{arr} = C\sqrt{\frac{\pi \overline{W} G_{arr}}{2\, dC/dL}} \tag{7.15}$$

The right-hand side of Eq. 7.15 is a prediction of the delamination arrest deflection δ_{arr} based on the measured compliance C and the numerical dC/dL. The predicted δ_{arr} using different G_{arr} values are plotted in Fig. 7.8 for both laminates. It is found that the predicted δ_{arr} data, as shown for example in the case of G_{arr} = 0.5 kJ/m^2, reproduce the measured linear variation between δ_{arr} and the delamination extension. The test data distribute around the predictions with G_{arr} = 1 kJ/m^2. This suggests that, knowing δ_{arr} and G_{arr}, the delamination size could be determined by the delamination arrest criterion.

In Section 7.6, for Laminate A, it has been shown by test data that δ_{arr}/C should vary linearly with the delamination length to reflect a constant G_{arr}. This point may be verified from Eq. 7.15 using the numerical dC/dL. As shown in Fig. 7.9, the linear variation of test data is reproduced by the predicted curve for both A and B type laminates, taking G_{arr} = 1 kJ/m^2. This shows again that the intrinsic variations of both δ_{arr} and C over the arrested delamination length are consistent with the constant delamination arrest toughness in the laminates.

It should be noted that G_{arr} by Eq. 7.2 does not include the effect of kinetic energy. Kinetic energy is generated by both the impact load and the unstable fracture. Part of the energy may be added to the crack driving force, so the crack may propagate further than expected from the release of stored elastic energy (59). If the effect of kinetic energy is significant, G_{arr} by Eq. 7.2 should decrease with the delamination size because the amount of kinetic energy increases with impact energy and crack extension (59). In Fig. 7.7, however, such an effect does not seem to be significant and may be within the scatter of test data. Actually, the contribution of kinetic energy to

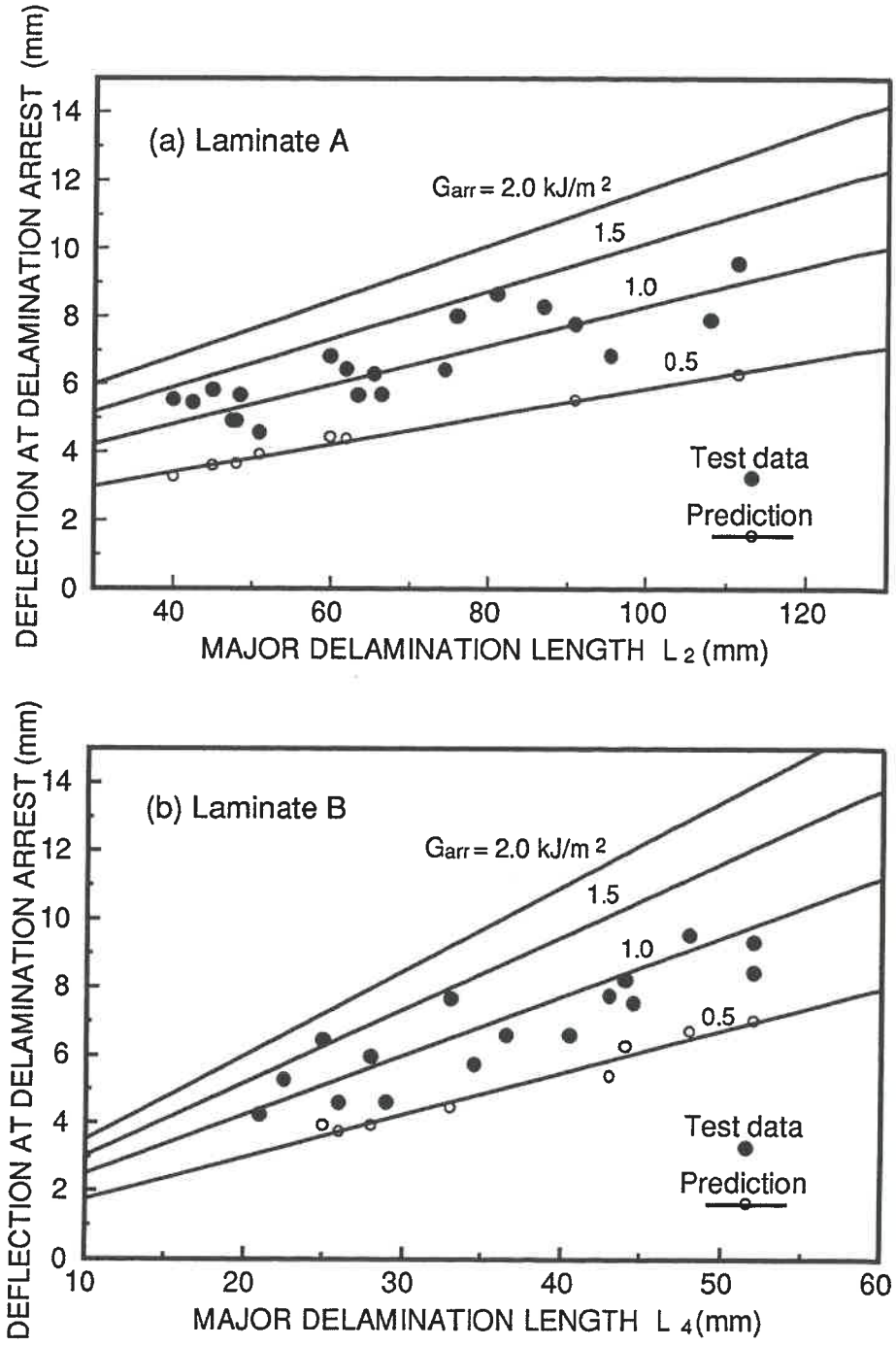

Figure 7.8 Predicted variation of δ_{arr} versus major delamination length: (a) Laminate A; (b) Laminate B.

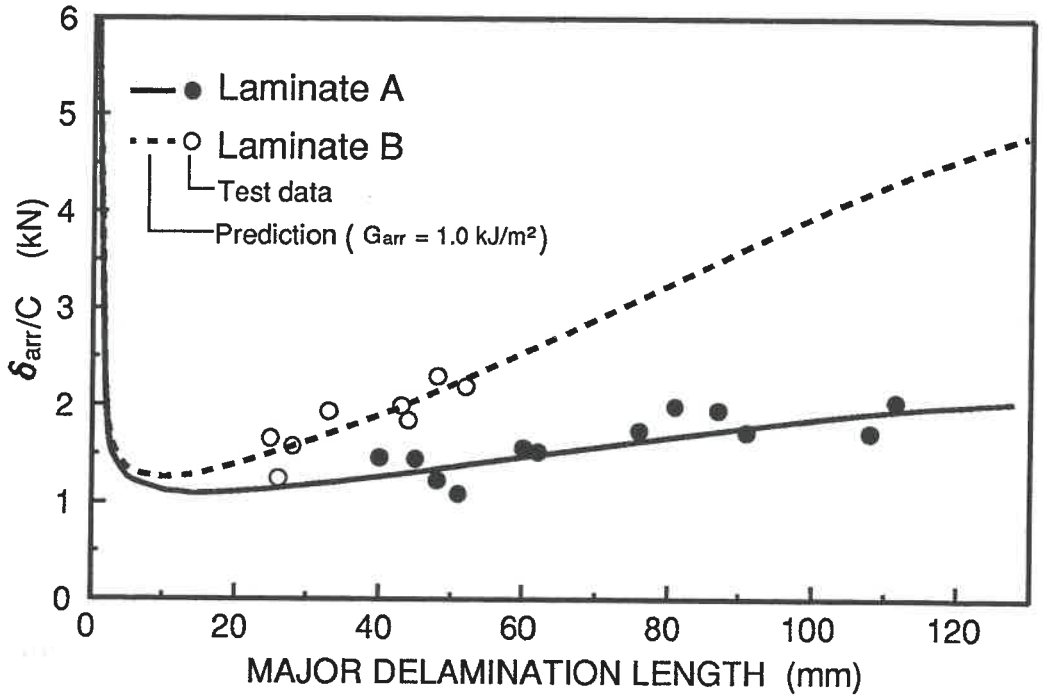

Figure 7.9 Predicted variation of δ_{arr}/C versus major delamination length in A and B type laminates.

crack growth depends on many factors such as the material properties, the sample geometry and the loading condition (92). In the present study, the plate response to the range of drop weight impact is basically quasi-static. In addition, the active crack front is much smaller than the dimension of the flexible plate. Much of the kinetic energy may be contained in the material away from the crack front (59), and its effect on crack arrest is limited. Similar observations have also been reported in other studies (66, 92-94).

Since the delamination arrest is under a Mode II dominated condition, it is interesting to compare G_{arr} with the Mode II toughness of the material. It is found that G_{arr} is close to the average propagation toughness of 1.02 kJ/m^2 , and lower than the dynamic initiation toughness of 1.30 kJ/m^2. The two values are measured on cracked beam specimens subjected to drop weight impact load (66). Moreover, G_{arr} is much lower than the initiation toughness under static loading (1.81~2.97 kJ/m^2 (66, 68, 78, 95, 96)). This sequence agrees with the loading rate dependence of the thermoplastic composite (68). For the less rate-dependent Glass/Epoxy composite, the Mode II arrest toughness is found to coincide with the static initiation toughness (72).

It must be noted that the Mode II toughness in (66, 68, 78, 95, 96) concerns the delamination between 0-degree plies. While G_{arr} in this study is not for a pure Mode II delamination and is the toughness at the 0/90 interface. In another respect, the G_{arr} value depends upon the measurement of the plate deflection at delamination arrest, δ_{arr}. From Eq. 7.2, the error in δ_{arr} can contribute a doubled error to G_{arr}, i.e.

$$\frac{\Delta G_{arr}}{G_{arr}} = 2\,\frac{\Delta \delta_{arr}}{\delta_{arr}} \tag{7.16}$$

In the present study, δ_{arr} was approximated in Eq. 7.4 by the deflection at maximum

impact load, δ_{pmax}. This assumption is based on the damage-related noise on the load-time signal which terminated at about the time of maximum load. High-speed photography of impact damage in $[0_5/90_5/0_5]$ Glass/Epoxy laminate (35) has shown that the major delamination stopped at or just before half of the contact duration, but no load record was available in (35). In the present study, as shown in Fig. 5.12a for example, δ_{pmax} also corresponds to about half of the contact duration. Further studies are required to verify this point. The combination of instrumented impact tester and the high speed photography should be able to accurately determine the load and deflection at the instant of delamination arrest.

7.9 Unstable Delamination Growth

Unstable fracture of impact-induced delamination has been observed in both thermoset and thermoplastic composites (21, 26, 27, 35, 50). However the mechanism of the fracture behavior has not been studied. Energy theory of fracture indicates that the stability of fracture depends on the variations of strain energy release rate and material resistance during crack growth. Since the unstable fracture takes place in a deflection-controlled condition, the strain energy release rate G defined by Eq. 7.1 varies with the plate compliance which changes as the delamination propagates. Therefore, if the interactions between the damage modes are neglected, G variation due to the major delamination growth can be obtained from the numerical C and dC/dL. On the other hand, the fracture resistance of polymer composites is generally sensitive to loading rate (66, 68-71). Under impact load or during rapid delamination growth, the strain rate at crack tip can be very high and the material toughness significantly

reduced. Based on these considerations, the fracture behavior of impact-induced delamination can be qualitatively studied.

Fig. 7.10 shows the variation of G in Laminates A and B under given plate deflections. Due to symmetry considerations, the G variation at either propagating crack fronts is shown, with $l = L/2$ being half of the major delamination length. At a given deflection, G first increases and then decreases as a function of the delamination length. As discussed in (59), this variation represents a typical case of unstable crack growth and subsequent arrest. Taking Laminate A as an example, the fracture behavior can be explained in more detail in Fig. 7.11.

It is assumed in Fig. 7.11 that the delamination is initiated from an initial length l_A. The initiation depends upon the value of G at l_A. When the impact energy is low, the plate deflection is small (such as $\delta = \delta_0$), so the delamination cannot be initiated because G is lower than the initiation toughness G_{cr}.

When the impact energy is at such a level that a critical deflection $\delta = \delta_{cr}$ is reached, the delamination will be initiated at Point A where $G = G_{cr}$. At onset of the delamination, an increasing amount of energy is released since G increases as the delamination grows. So the delamination may speed up due to more energy available for crack growth. At the same time, the material toughness, which is also shown schematically in the figure, decreases at the crack tip. Thus the delamination is accelerated to result in an unstable crack growth. The unstable growth continues when G remains higher than the material toughness, but the delamination may decelerate as G passes over its maximum (Point B) and decreases, as observed in (35). The material toughness might also recover as the crack slows down (59). The crack arrest occurs at Point C where $G = G_{arr}$. Thus, at the critical impact energy, the delamination suddenly initiates at l_A and extends to l_C.

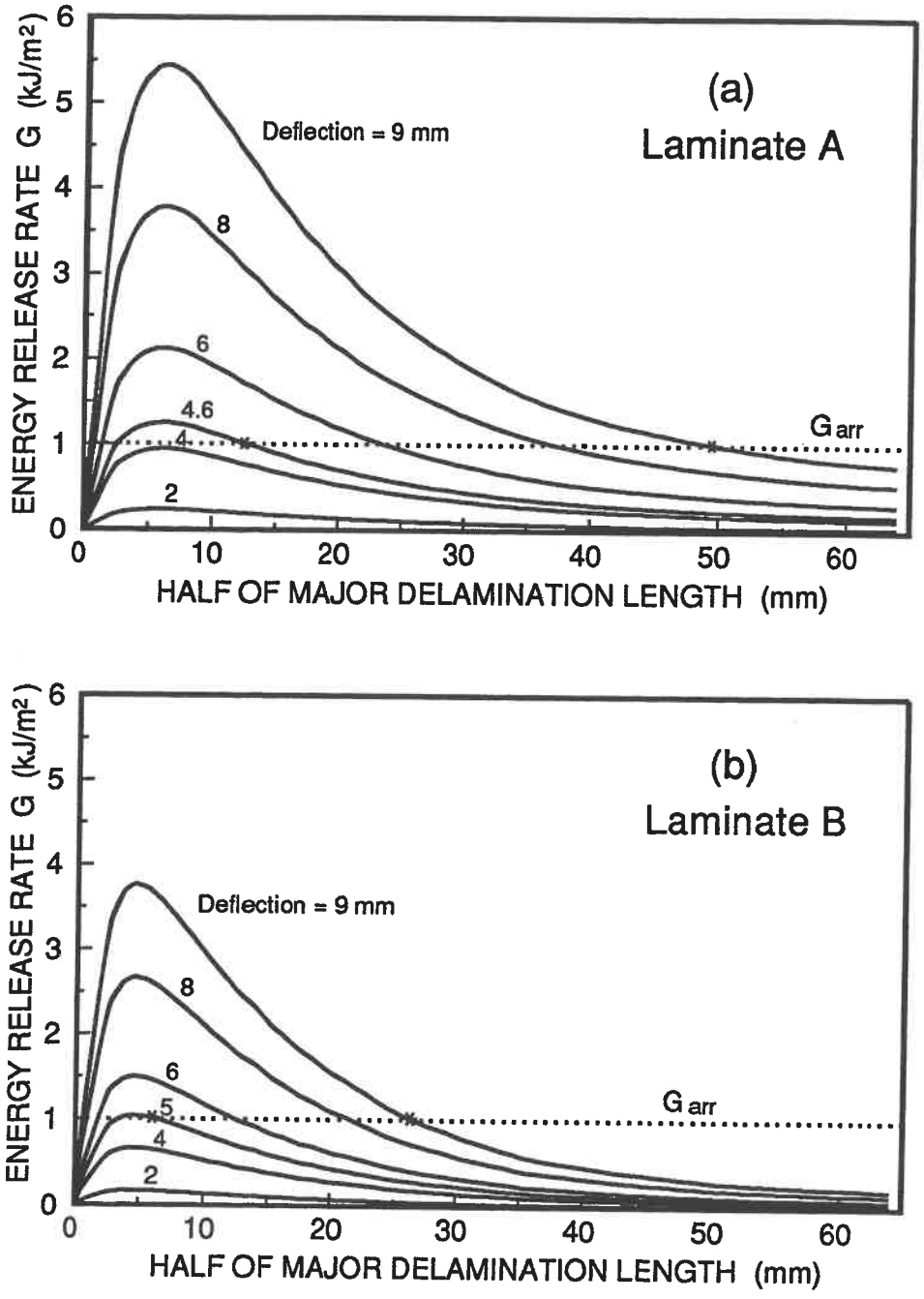

Figure 7.10 Variation of strain energy release rate with major delamination extension: (a) Laminate A; (b) Laminate B.

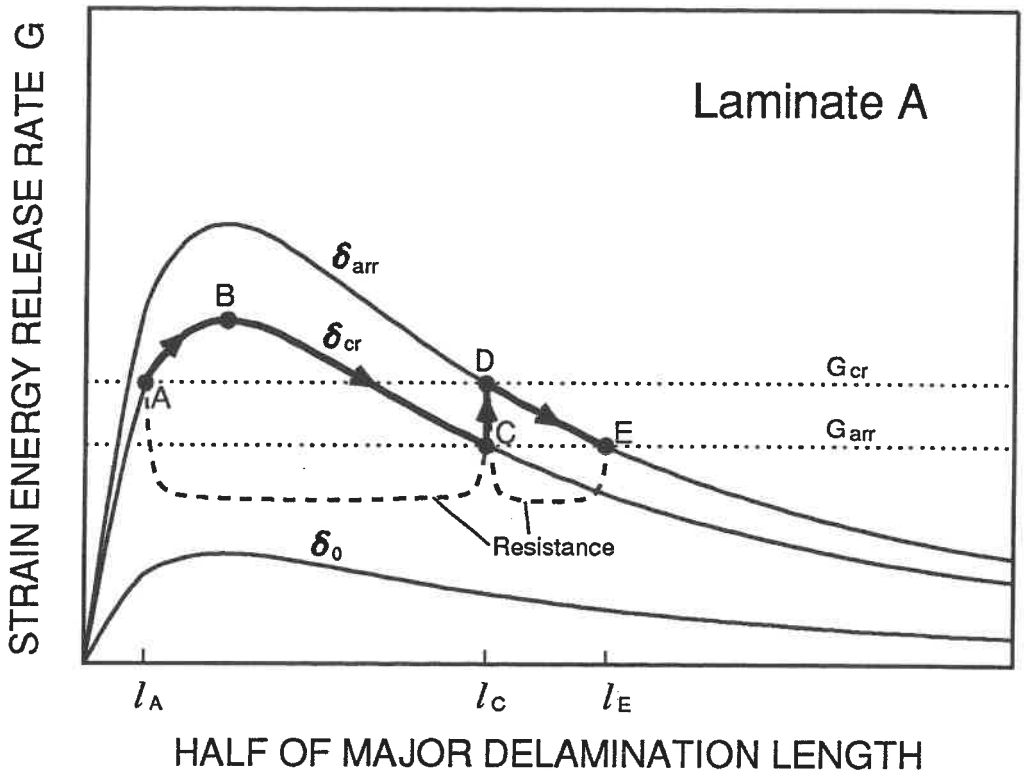

Figure 7.11 Unstable crack growth mechanism of impact-induced delamination.

When a higher impact energy is applied, the delamination will be a multiple crack growth process. First, the delamination is initiated at Point A when the plate deflection reaches δ_{cr}. The delamination rapidly propagates at this deflection, with G varying from Pint A to Point C. It is temporarily arrested at Point C because $G = G_{arr}$. This results in an initial crack extension from l_A to l_C. Since the deflection still increases, G at the current delamination front l_C also increases. If the plate deflection is large enough to rise G to G_{cr} once again (i.e. to Point D), the delamination will be initiated to have a subsequent crack growth from l_C to l_E. The delamination is arrested at l_E because G drops to G_{arr} at Point E. Depending on the level of impact, the subsequent growth may repeat a few times until final crack arrest is reached at $\delta = \delta_{arr}$. It is seen from Fig. 7.11 that the subsequent growth extends a small distance within the region of a decreasing G. However, the growth may still be unstable because the dynamic effects or material inhomogeneity could induce an initial crack speed and cause the material toughness to drop as shown in the figure.

The crack growth mechanism in Fig. 7.11 seems to be supported by test observations. During testing, the delamination did not occur in the two laminates under the impact of below 3 J. It was suddenly initiated at around 3 J, extending about 48 mm in Laminate A and 23 mm in Laminate B. The dependence of crack extension on laminate construction may be explained by the G-curve in Fig. 7.10. The G-curve of Laminate A is more flattened than that of Laminate B, and it possesses a larger span over a constant G_{arr}. At higher impact energies, larger delaminations may be generated in both laminates. While the fracture surface, such as that shown in Fig. 5.5, exhibits the trace of a multiple crack growth process.

It is worth noting that the fracture mechanism in Fig. 7.11 is based on a simplified fracture analysis. In reality, the delamination involves a complex fracture

process. First, it has been shown that the delamination is initiated from the critical transverse cracks, which are near, but a distance away from, the impact point (13, 14, 39). So the initial delamination length in Fig. 7.11 is measured between a pair of the critical cracks (Fig. 5.7a), i.e., $2l_0 = 2l_A = 2.5$. However, as can be seen in Fig. 5.5, the delamination was not initiated from a single pair of transverse cracks, but from a group of cracks distributed in the initiation region. Secondly, the delamination seems to be initiated at the same time as the transverse cracks propagate. The delamination at the first interface is also initiated simultaneously. Therefore the interactions between the damage modes must be significant in the initiation phase. In another respect, the dynamic initiation toughness G_{cr} = 1.30 kJ/m^2 has been assumed in Fig. 7.11 for a qualitative discussion. This value belongs to the pure Mode II fracture of unidirectional APC-2 composite under drop weight impact (66). The complex crack initiation process as shown in Fig. 5.5 is rather controlled by some mixed-mode fracture properties of the material.

Experimental studies (26, 27) in terms of comparison testing have shown that the laminate response under low velocity impact approximates to the static indentation response. Similar delaminations are also observed in the indentation test as a result of unstable crack growth and subsequent arrest (26, 27). Since the present analysis is based on quasi-static considerations, the fracture behavior in Fig. 7.11 may also apply to delaminations caused by indentation load.

Chapter 8

Measurement of Mode II Interlaminar Fracture Toughness

8.1 Objective

Previous studies demonstrate that the impact-induced delamination in the crossply laminates results from a Mode II dominated unstable fracture. The delamination seems to be arrested at a constant interlaminar fracture energy. Therefore the Mode II fracture toughness may be an important parameter for characterizing the delamination. In the present study, the end-loaded-split (ELS) fracture test (97) is conducted to measure the Mode II toughness of APC-2 composite.

The ELS specimen, as shown in Fig. 8.1, is a cantilever beam with a midplane crack near the loaded end. This specimen is considered because the crack may grow in an initially unstable and subsequently stable manner (72). The fracture behavior may be used to measure the Mode II crack arrest toughness if the crack is arrested within the beam span. The crack arrest toughness has been measured in (72) for Glass/Epoxy composite. The measurement for APC-2 composite is discussed in the present chapter.

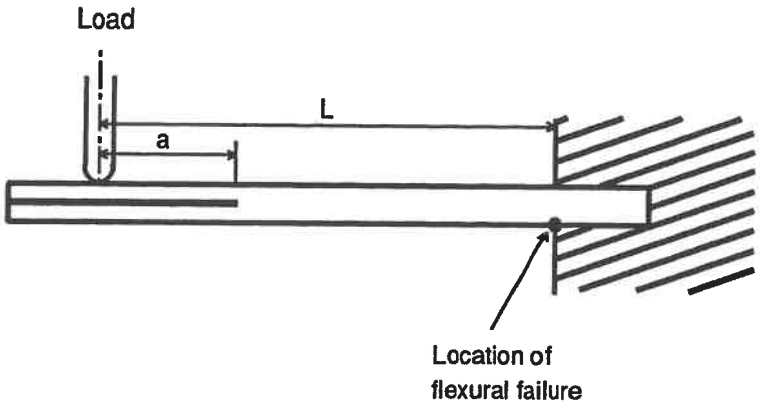

Figure 8.1 End-loaded-split (ELS) fracture test.

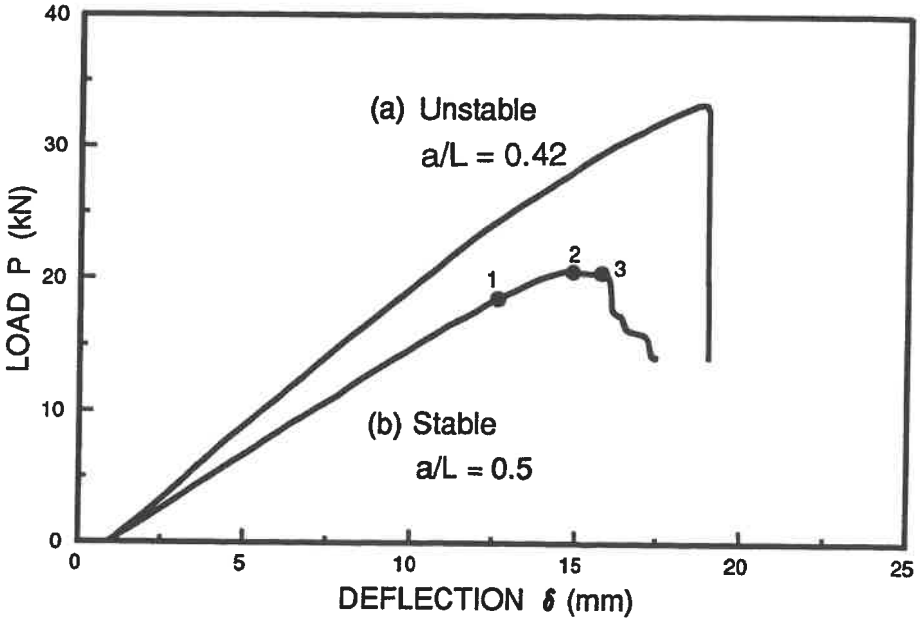

Figure 8.2 Load-deflection response of PEEK/Carbon (APC-2) composite under ELS test: (a) unstable fracture; (b) stable fracture.

8.2 ELS Fracture Test

Some $[0]_{26}$ plates were manufactured for the ELS fracture test, following the procedure discussed in Section 4.2. The artificial delamination was made by inserting a 25μm-thick Kapton film at the midplane of the plate during laying up. After molding, the plates were cut into 145 × 12.5 × 3.5 mm beam specimens using a diamond coated saw. Water was used to reduce the local heating caused by cutting.

The ELS test was conducted on an Instron 1125 tester at the crosshead speed of 5 mm/min. The beam span, L, was 80 mm. And the crack length, a, was varied by clamping the specimen at different positions along the uncracked part of the beam. Fracture analysis by linear beam theory (98) predicts that the crack growth may be unstable when $a/L < 0.55$ and is stable for longer crack lengths. Both stable and unstable fracture cases were considered. A modified cylindrical load nose, 3 mm in diameter, was used to provide a uniform line load over the beam width. During testing, the load-deflection (P-δ) response of the specimen was monitored using the Instron Series IX automated materials testing system, which was operated through a personal computer.

Previous studies (96, 99) on Mode II fracture of APC-2 composite have shown that the resin-rich region at the Kapton-film crack tip results in artificially high values of Mode II toughness. Therefore, a Mode II precrack was introduced as suggested in (99). For precracking, the specimen was clamped with $a/L > 0.65$ and was loaded until the crack stably extended for about 10 mm. Then the cracked part of the sample was slightly opened and the crack tip position determined using a 10× optical microscope. The crack tip was marked on both sides of the beam.

8.3 Results and Discussion

8.3.1. Crack Length and Fracture Load

Determination of fracture toughness depends on measuring the crack length and the load (or deflection) at fracture. The crack length was measured on the fractured sample between the initial crack tip and the imprint of load nose on the beam surface. The measurements on both sides of the sample differ within 1.6 mm and the average value was used for toughness calculation.

The fracture load, P_{cr}, was determined from the P-δ curve as shown in Fig. 8.2. Case (a) is a typical unstable fracture and Case (b) is a stable one. In both cases, the P-δ response is linear at small deflections and gradually becomes nonlinear as the deflection increases. The extent of nonlinearity becomes more significant when approaching the maximum load, P_{max}. Nonlinearity in P-δ curve has also been observed in Mode II test on APC-2 composite using the end-notched-flexure (ENF) specimen (78, 96, 99). In (78, 96, 99) the ENF specimens were sized to guarantee a small deflection at fracture, and the observed nonlinearity was attributed to either the visco-elastic effects or subcritical crack growth in addition to material yielding at the crack tip. In the ELS specimens, however, the deflection in Fig. 8.2 was relatively large when the nonlinear response began. Therefore it is expected that the effect of large deflection may also be a source of the nonlinearity.

In order to determine P_{cr}, a few specimens were selectively unloaded at different load levels. The specimen edges were then examined under the microscope for crack growth. The unloading points are illustrated in Fig. 8.2b, where Point 1 is in the range of initial nonlinearity, Point 2 is located just before P_{max}, and Point 3

(obtained only for stable crack growth) is when the load passed over P_{max} and began to flatten or to drop. It was found that the crack did not seem to grow at the load levels defined by Points 1 and 2, while crack growth was always observed at Point 3. Therefore, the initial nonlinearity in the P-δ curve is caused by the large deflection effect. And it is appropriate to assume that the crack initiation occurred at around P_{max}.

It should be noted that some stable crack growth has been observed in ENF specimens before the maximum load is reached (78, 96, 99). Such growth, if existed, was not measurable in the ELS specimens. Nonlinear deformation and microdamage (96) may have also occurred at the crack tip before P_{max} was reached. The enhanced nonlinearity near P_{max} might be due to such mechanisms. The mechanisms may be detected by techniques such as acoustic emission (96), not by visual inspection of the specimen edges. In the present study, the fracture toughness is defined as the material resistance to growth of the observable "macro-crack". Thus it is reasonable to take P_{max} as the critical load for crack initiation. The corresponding deflection, δ_{pmax}, was also recorded for toughness calculation.

8.3.2 Large Deflection Effect

Linear elastic fracture mechanics theory indicates that (59), if the P-δ response of a cracked beam remains linear until fracture, the fracture toughness G_c can be calculated either from the fracture load P_{cr}:

$$G_c = \frac{P_{cr}^2}{2b}\frac{dC}{da} \tag{8.1}$$

or from the deflection at fracture δ_{cr}:

$$G_c = \frac{1}{2b}\frac{\delta_{cr}^2}{C^2}\frac{dC}{da} \tag{8.2}$$

The flexural compliance C may be derived from linear beam theory. For the ELS specimen it has been shown that (98)

$$C = \frac{12}{bh^3 E_f}(a^3 + \frac{L^3}{3}) \tag{8.3}$$

where E_f is the flexural modulus in the axial direction of the beam, which can be measured by the method developed in (72). Then the Mode II toughness may be written in the form

$$G_{IIc}^s(P) = \frac{18P_{cr}^2 a^2}{b^2 h^3 E_f} \tag{8.4}$$

or equivalently

$$G_{IIc}^s(\delta) = \frac{9\delta_{cr}^2 a^2 h^3 E_f}{8(3a^3 + L^3)^2} \tag{8.5}$$

where $G_{IIc}^s(P)$ and $G_{IIc}^s(\delta)$ denote the toughness values calculated by P_{cr} and δ_{cr} respectively.

Eqs. 8.4 and 8.5 are simple to use and valid in the range of small deflections. However, in testing APC-2 composite, the ELS specimen requires a large deflection to

initiate the fracture. In this situation, the toughness could still be calculated from Eqs. 8.4 or 8.5, but the resulting values may not be accurate because the fracture occurs in the nonlinear range of P-δ curve. Although such effects can be minimized by increasing the sample thickness, it is of practical significance to evaluate the effects and to provide corrections to the linear theory results.

Large-deflection analysis of ELS specimen has been considered by Williams (98, 100). The ELS specimen in (98, 100) is different from the original form (Fig. 8.1). And the corrections to Eq. 8.4 were only provided for the limiting cases as $a/L \rightarrow 0$ and $a/L \rightarrow 1$. In the present study, a similar analysis was carried out for the original ELS specimen, and corrections to Eqs. 8.4 and 8.5 were obtained for all range of crack length. Details of the analysis are included in Appendix A.

Analyses in Appendix A show that the toughness values calculated from Eqs. 8.4 and 8.5 differ if the specimen is fractured at a large deflection. For the crack length of $a/L > 0.3$, the Mode II toughness G_{IIc} is generally underestimated by $G^s_{IIc}(P)$ and is over estimated by $G^s_{IIc}(\delta)$. The large deflection effect may be eliminated by using the following corrections:

$$G_{IIc} = F_P \, G^s_{IIc}(P) \tag{8.6}$$

$$G_{IIc} = F_\delta \, G^s_{IIc}(\delta) \tag{8.7}$$

where F_P and F_δ are the large deflection correction factors. Figs. 8.3 and 8.4 plot F_P and F_δ respectively as functions of the specimen deflection normalized by crack length. The values are also tabulated in Appendix B for reference. The data reduction scheme based on Eqs. 8.4 and 8.6, or Eqs. 8.5 and 8.7, maintains the simple calculation

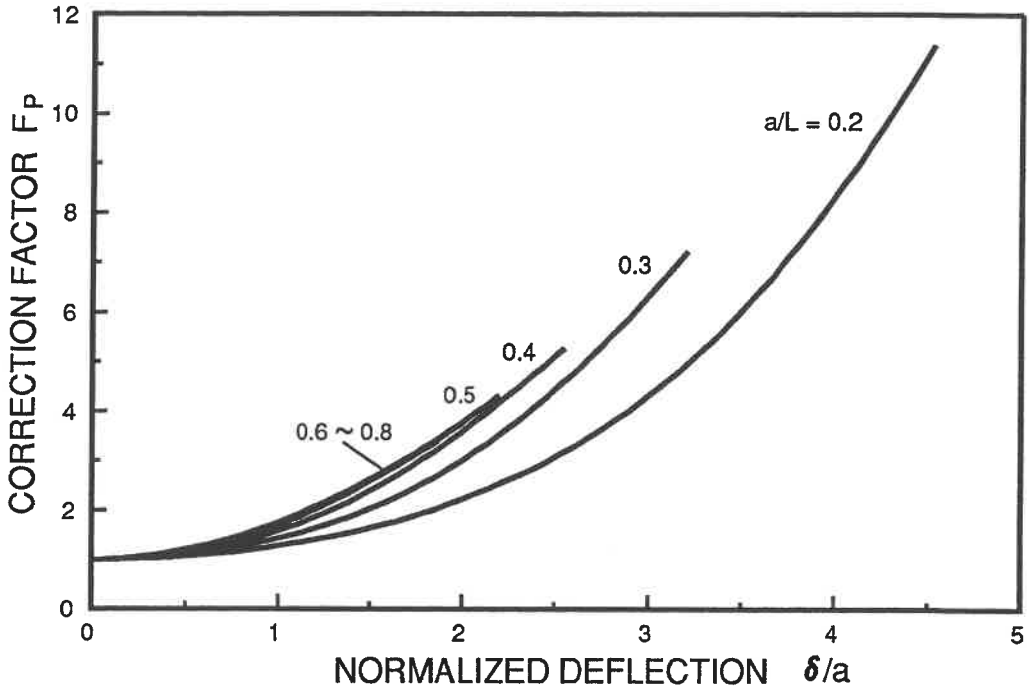

Figure 8.3 Large-deflection correction factor for Mode II fracture toughness calculated by linear beam theory using fracture load.

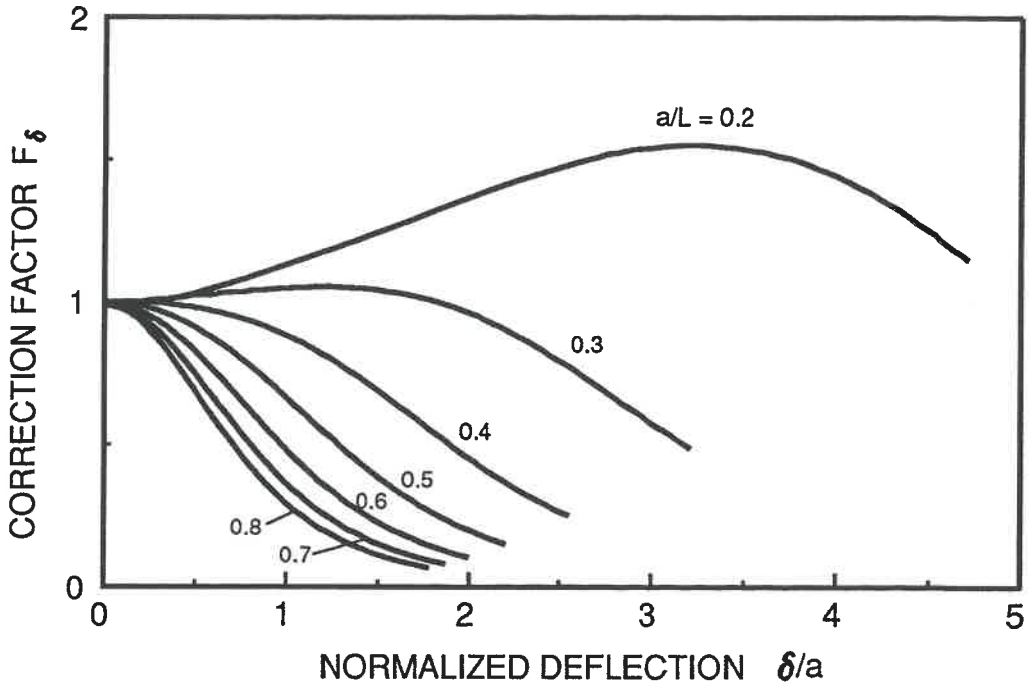

Figure 8.4 Large-deflection correction factor for Mode II fracture toughness calculated by linear beam theory using sample deflection at fracture.

by linear beam theory and accounts for the large deflection effect.

8.3.3 Mode II Initiation Toughness

Fig. 8.5 presents the Mode II initiation toughness calculated from P_{cr} and δ_{cr} using Eqs. 8.4 and 8.5 respectively. Each calculation seems to suggest a constant toughness over the crack length within the scatter in test data, but the value from δ_{cr} is obviously higher than that from P_{cr}. This is consistent with the large deflection effect as discussed in Appendix A. The results corrected by Eqs. 8.6 and 8.7 are plotted in Fig. 8.6, where the data of the specimens from one panel are shown for clarity. The corrected data tend to agree with each other to suggest a common toughness. G_{IIc} averaged from all test data is 2.82 kJ/m^2, which is higher than the value in (66, 68, 99) but agrees with that reported by other researchers (78, 96).

8.3.4 Unstable Fracture

One of the purposes in testing the ELS specimen is to measure the Mode II crack arrest toughness of APC-2 composite. Such a measurement requires two conditions that the unstable fracture is achieved and the crack growth is arrested within the beam span. Since the unstable fracture occurs at a high crack speed, the sample deflection remains almost constant during the fracture process. So the arrest toughness, G_{IIa}, may be calculated from Eq. 8.5 by using the arrested crack length, a_{arr}.

G_{IIa} has been measured successfully in (72) for Glass/Epoxy composite.

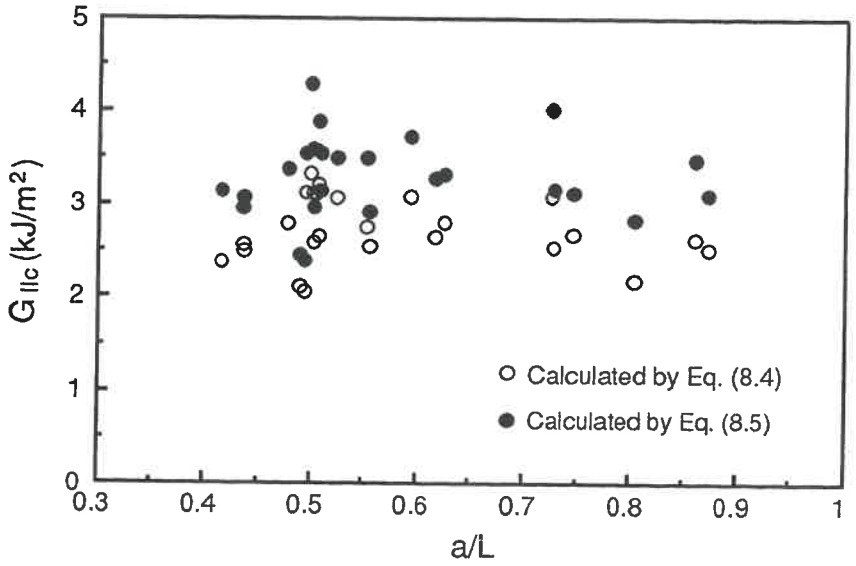

Figure 8.5 Mode II delamination initiation toughness as a function of crack length for PEEK/Carbon (APC-2) composite: before correction.

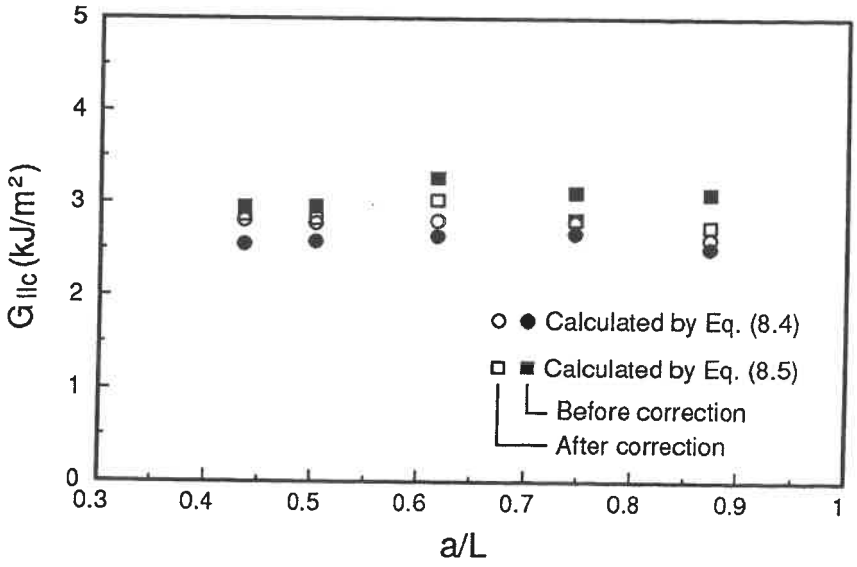

Figure 8.6 Mode II delamination initiation toughness as a function of crack length for PEEK/Carbon (APC-2) composite: after correction.

However, it could not be measured in the present study for APC-2 composite. The unstable crack was not arrested within the beam span and it propagated into the clamped end. The crack arrest could not be achieved even if thicker specimens ($[0]_{30}$ and $[0]_{40}$) were used. It seems that, for the rate-sensitive material, the ELS specimen should be modified or other types of specimen developed for measuring G_{IIa}.

Some considerations on the fracture behavior of the ELS specimen may be helpful for the design of a better test method for G_{IIa} measurement. Fig. 8.7 shows the variation of strain energy release rate, G_{II}, over the crack growth in an APC-2 ELS specimen at the critical deflection. From the linear beam theory analysis (98), the unstable fracture may be achieved if

$$a/L < 0.55 \tag{8.8}$$

where G_{II} increases at crack initiation. However, test observation showed that the condition for unstable fracture is affected by a number of mechanisms. First, as shown in Fig. 8.1, a flexural failure may occur at the clamped end because of excessive axial compressive stress at the bottom surface of the beam. Such a failure must be prevented for a valid fracture test. At crack initiation, $G_{II} = G_{IIc}$, so the maximum compressive stress σ_{max} may be derived from the bending moment at the clamped end, i.e.

$$\sigma_{max} = (\frac{L}{a})\sqrt{\frac{2E_f G_{IIc}}{h}} \tag{8.9}$$

σ_{max} should not exceed the axial compressive strength σ_{cr} of the material. This requires that

$$\frac{a}{L} > \sqrt{\frac{2E_f G_{IIc}}{h\sigma_{cr}^2}} \tag{8-10}$$

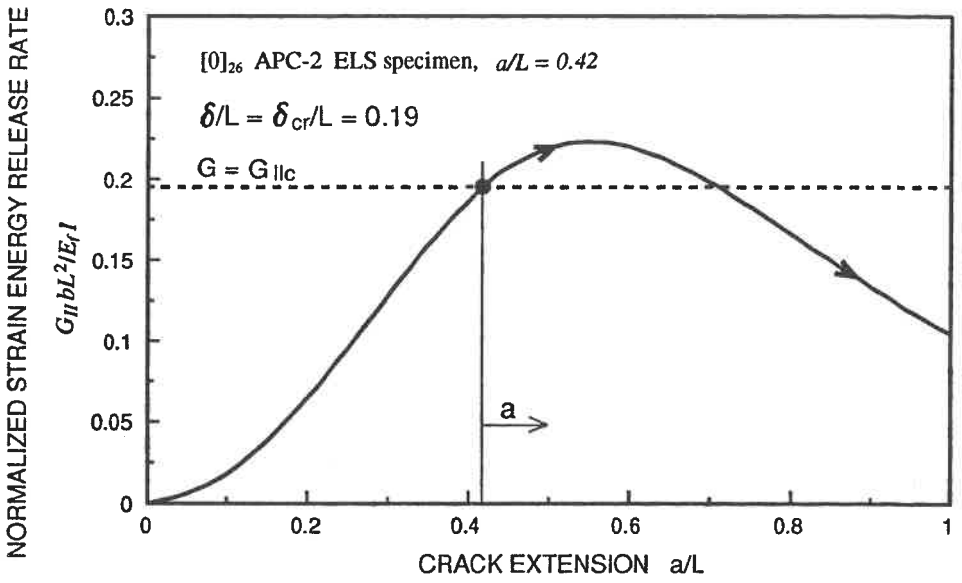

Figure 8.7 Variation of strain energy release rate in a PEEK/Carbon (APC-2) ELS specimen during crack extension.

Therefore the crack length without flexural failure depends on the relative magnitudes of the fracture toughness, flexural modulus and compression strength of the material. Referring to Eq. 8.8, the unstable fracture may not occur in the material having either a high fracture toughness or a low compressive strength, unless thick specimens are used. For the $[0]_{26}$ APC-2 specimen, with σ_{cr} = 1100 MPa (Table 4.1), $E_f = 118\ GPa$, G_{IIc} = 2.82 kJ/m^2 and h = 3.5 mm, a small range of crack length is available for producing unstable fracture:

$$0.4 < a/L < 0.55 \tag{8.11}$$

In fact, the crack length is more limited than Eq. 8.11 because of the large deflection effect. As discussed in Appendix A, the large deflection effect tends to reduce the crack length for producing unstable fracture. Test results showed that the unstable fracture could be achieved at about a/L = 0.43. A longer or shorter crack length may result in either a stable fracture or the bending failure at the clamped end. This limitation must be considered in designing a flexural specimen for G_{IIa} measurement.

In Fig. 8.7, with similar discussions as in Fig. 7.11, the position of crack arrest seems to depend on both the shape of the G-curve and the fracture properties of the material. For a less rate-sensitive composite, G_{IIa} is lower but close to G_{IIc}. So the crack could be arrested within the specimen. This is the case in testing Glass/Epoxy composite (72), where G_{IIa} was found to be around the initiation toughness. For the rate-sensitive composite, G_{IIa} may be much lower than G_{IIc}. The crack could not be arrested before reaching the clamped end, where G_{II} is still high enough to drive the crack. It seems that, to arrest the crack within the beam, the specimen should be so designed that the G-curve decreases sharply to very low values in the range of stable

fracture.

A survey is made of the available Mode II fracture tests using cracked beam specimens. The width-tapered ELS specimen (98) has been shown to offer a stable fracture. As shown in Figs. 8.8a and 8.8b, the fracture in the center-notched-flexure (CNF) specimen (66, 95) and the cantilever-beam-enclosed-notch (CBEN) specimen (72) is essentially unstable. These specimens cannot be used for measuring G_{IIa}. The end-notched-flexural (ENF) specimen (101), Fig. 8.8c, exhibits a unstable/stable fracture behavior for the initial crack length of $a/L < 0.75$. The G-curve over $a > L$ is established from the compliance expression derived in (71). The G-curve can decrease to very low G_{II} values in the stable fracture range. This specimen could be a candidate for measuring G_{IIa} in rate-sensitive composites. However, care must be taken for the position of crack arrest. Since the load is applied at $a = L$ and G_{II} drops sharply at $a > L$, the crack may be arrested at or near the point of load application. So the friction between the crack surfaces (58) contributes to the crack arrest. This effect should be evaluated before the specimen could be applied for G_{IIa} measurement.

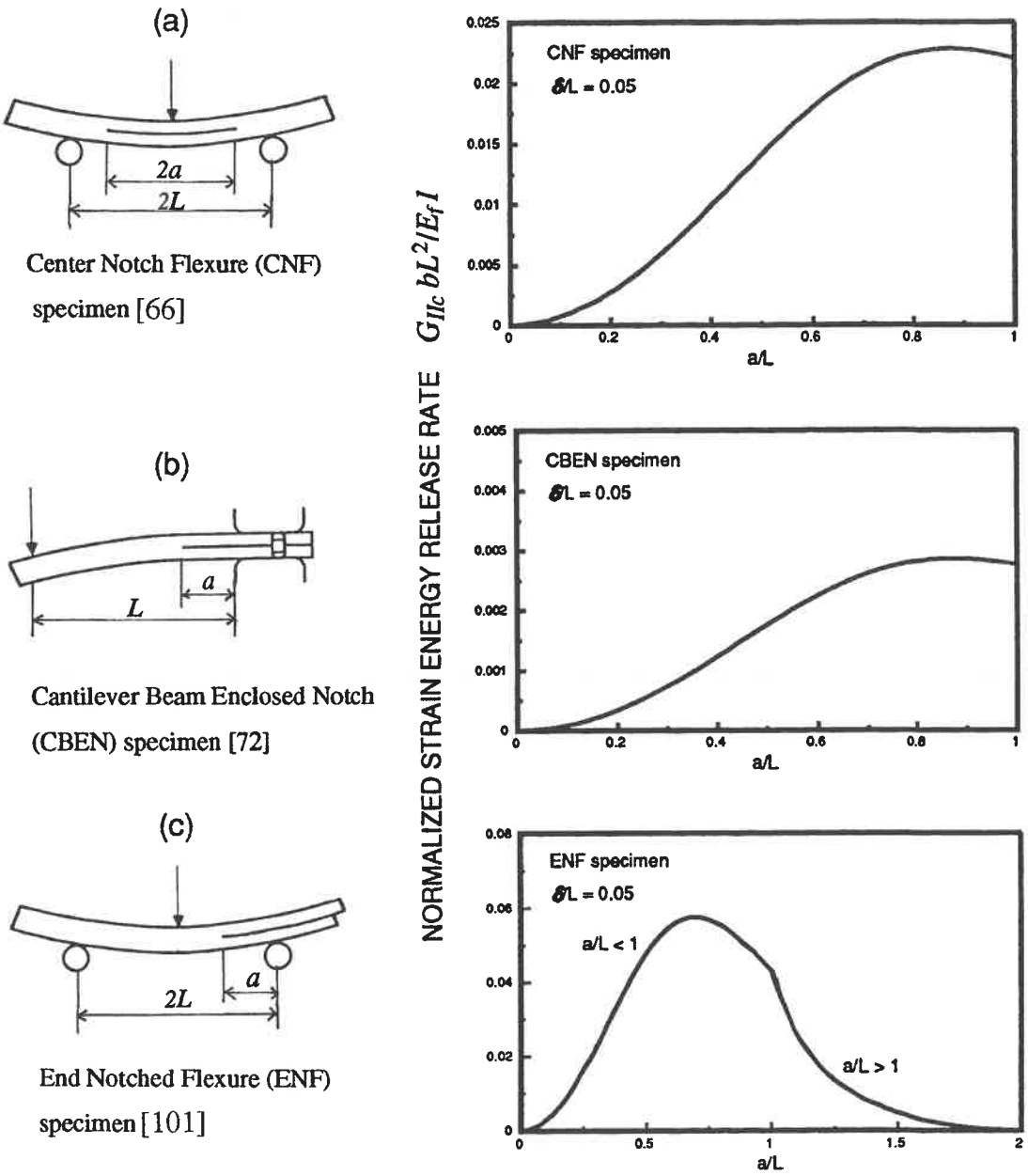

Figure 8.8 Variation of strain energy release rate as a function of crack extension in the typical Mode II fracture test specimens under a given deflection.

Chapter 9

Summary and Conclusion

In summary, this dissertation studies the low velocity impact damage in PEEK/Carbon (APC-2) thermoplastic composite. Emphases of the study were focused on the material properties that may control the damage extension of impact-induced delamination and transverse crack. Specifically, the following studies have been carried out:

1) Three crossply laminates, namely $[0_5/90_5/0_5]$, $[0_3/90_3/0_3/90_3/0_3]$ and $[0/90/.../0/90]_{15t}$, were subjected to instrumented drop weight impact test. The damage behavior was characterized by visual inspection, X-radiography and a thermal deplying technique. Fractography of the delamination surface was studied by scanning electron microscope and compared with that of pure Mode I and Mode II impact fracture surfaces. The post-impact flexural compliance was also measured by a static indentation test.

2) A method combining the "first-ply-failure" test and incremental laminate analysis was proposed to determine the thermal residual stress and the *in situ* lamina strength in the thermoplastic laminates.

3) The Strength of Materials approach to characterizing the damage extension was evaluated by a dynamic finite element stress analysis using the

measured impact force history. Correlations between the impact stress field and damage extension were studied qualitatively. Effects of the residual stress and crack constraining mechanism on transverse crack extension were accessed.

4) A fracture mechanics approach based on the concept of crack arrest toughness was proposed to characterize the impact-induced delamination. The delamination arrest criterion was verified by studying the delamination behavior in $[0_5/90_5/0_5]$, $[0_3/90_3/0_3/90_3/0_3]$ laminates. The strain energy release rate was calculated by the compliance method of linear elastic fracture mechanics. The variation of compliance with delamination size was calibrated by a finite element method which simulates the delaminations and transverse cracks. The predicted compliance was combined with test data to perform the fracture analysis.

5) Large deflection analysis of the end-loaded-split (ELS) fracture test was conducted and verified by test measurement. Data reduction procedure of the test was improved to take into account the large deflection effect on Mode II toughness measurement. Using the specimen for measuring Mode II crack arrest toughness was also discussed.

Based on the above studies, the following remarks could be made:

1) For the crossply laminates studied, APC-2 composite exhibits the same damage modes as thermoset epoxy composites. Delamination and transverse crack predominate the damage in $[0_5/90_5/0_5]$ and $[0_3/90_3/0_3/90_3/0_3]$ laminates, while fiber breakage controls the penetration failure in $[0/90/.../0/90]_{15t}$ laminate. The material is superior to Kevlar/Epoxy and Graphite/Epoxy in impact delamination resistance.

2) Thermal residual stresses in the laminates can be as high as half of the transverse strength of the material. For a small lamina thickness, the crack constraining mechanism significantly increases the *in situ* lamina strength over the unidirectional

strength.

3) The extension of transverse cracks in the impacted laminates cannot be predicted by the Strength of Materials approach. The delamination growth is qualitatively related to the interlaminar shear stress field. But the stress field cannot be used to predict the delamination size because it had been released at the delaminated interface.

4) Impact-induced delamination in the crossply laminates is a process of Mode II dominated unstable fracture and subsequent crack arrest. The delamination extension may be characterized by strain energy release rate and the delamination arrest criterion. The fracture occurs under deflection-controlled conditions and is arrested at a constant interlaminar fracture energy. For the two laminates considered, the delamination arrest toughness seems to be independent of the delamination size.

5) Large deflection effect may be significant in the end-loaded-split (ELS) fracture test. The toughness values calculated linear beam theory can be corrected by the correction factors provided in the present study.

Chapter 10

Recommendation

The following recommendations are made for future investigations:

1) The proposed delamination arrest criterion needs to be verified by testing different laminate types and various material systems. The effects of laminate geometry and impact conditions should also be evaluated.

2) On-line records of the impact force, laminate response and the history of delamination propagation are required for studying the delamination growth. Instrumented impact test equipped with a combination of the moiré technique and high speed photography (51) may be an appropriate choice for the opaque carbon fiber composites.

3) Simple and effective methods should be developed to calculated the strain energy release rate in damaged laminates. The finite element model used in the present study may be improved to calculate the strain energy release rate at the delamination front, then the effect of large deflection on delamination growth may be estimated.

4) The finite element model may also be used to simulate the delamination propagation by releasing the MPC equations at the delamination front. Multiple delaminations at different interfaces may be simulated to assess the interactions

between them.

5) Test methods should be developed to characterize the dynamic fracture properties of composite materials. The Mode II crack arrest toughness could possibly be measured by modifying the ELS specimen or the ENF specimen. The effect of kinetic energy on the toughness measurement needs to be estimated.

Reference

1. *Toughened Composites: Recent Developments*, NASA Langley Research Center (1985).

2. PARTRIDGE, I. K., *Advanced Composites.*, Elsevier Science Publishers Ltd. (1986).

3. EVANS, R. E. and J. E. MASTERS, 1987 "A New Generation of Epoxy Composites for Primary Structural Applications: Materials and Mechanics," in *Toughened Composites, ASTM STP 937*, pp. 413-436.

4. DUMUTS, E., R. S. WHITEHEAD and B. DEO, 1985 "Assessment of Damage Tolerance in Composites," Composites, 4, 45-58.

5. BAKER, A. A., R. JONES and R. J. CALLINAN, 1985 "Damage Tolerance of Graphite/Epoxy Composites," Composite Structures, 4, 15-44.

6. RAMKUMAR, R. L., 1983 "Effect of Low-Velocity Impact Damage on the Fatigue Behavior of Graphite/Epoxy Laminates," in *Long-Term Behavior of Composites, ASTM STP 813*, pp. 116-135.

7. WILLIAMS, J. G. and M. D. RHODES, 1982 "Effect of Resin on Impact Damage Tolerance of Graphite/Epoxy Laminates," in *Composite Materials: Testing and Design (Sixth Conference), ASTM STP 787*, pp. 450-480.

8. WANG, H., P. H. CHEN and Z. SHEN, 1988 "Compression Failure of Graphite/Bismaleimide Quasi-Isotropic Laminates after Impact," in Proc. 4th National Conference on Composites, Xian, China (1988).

9. WHITCOMB, J. D. and K. N. SHIVAKUMAR, 1989 "Strain-Energy Release Rate Analysis of Plates with Postbuckled Delaminations," Journal of Composite Materials, 23, 714-733.

10. *Foreign Object Impact Damage to Composites, ASTM STP 568* (1975).

11. CANTWELL, W. J. and J. MORTON, 1991 "The Impact Resistance of Composite Materials: A Review," Composites, 22, 347-362.

12. GRESZCZUK, L. B., 1975 "Response of Isotropic and Composite Materials to Particle Impact", in *Foreign Object Impact Damage to Composites, ASTM STP 568*, pp. 183-211.

13. JOSHI, S. P. and C. T. SUN, 1985 "Impact Induced Fracture in a Laminated Composite," Journal of Composite Materials, 19, 51-66.

14. CHOI, H. Y., H.-Y. T. WU and F.-K. CHANG, 1991 " A New Approach to-

wards Understanding Damage Mechanisms and Mechanics of Laminated Composites Due to Low-Velocity Impact: Part II-Analysis," Journal of Composite Materials, 25, 1012-1038.

15. CHOI, H. Y., H. S. WANG and F.-K. CHANG, 1992 "Effect of Laminate Configuration and Impactor's Mass on the Initial Impact Damage of Graphite/Epoxy Composite Plates Due to Line-Loading Impact," Journal of Composite Materials, 26, 804-827.

16. WU, H. -Y. T. and G. S. SPRINGER. 1988 "Impact Induced Stresses, Strains, and Delaminations in Composite Plates," Journal of Composite Materials, 22, 533-558.

17. CHOI, H. Y. and F. -K. CHANG, 1992 "A Model for Predicting Damage in Graphite/Epoxy Laminated Composites Resulting from Low-Velocity Point Impact," Journal of Composite Materials, 26, 2134-2169.

18. CAIRNS, D. S. and P. A. LAGACE, 1992 "A Consistent Engineering Methodology for the Treatment of Impact in Composite Materials," Journal of Reinforced Plastics and Composites, 11, 395-412.

19. BACHRACH, W. E. and R. S. HANSEN, 1988 "Mixed Finite-Element Method for Composite Cylinder Subjected to Impact," AIAA Journal, 27, 632-638.

20. BOGDANOVICH, A. E. and E. V. IARVE, 1992 "Numerical Analysis of Im-

pact Deformation and Failure in Composite Plates," Journal of Composite Materials, 26, 520-545.

21. WANG, H. and T. VU-KHANH, 1991 "Impact-Induced Delamination in $[0_5/90_5/0_5]$ Carbon Fiber/Polyetheretherketone Composite Laminates," Polymer Engineering & Science, 31, 1301-1309.

22. WANG, H. and T. VU-KHANH, "Low Velocity Impact Damage in PEEK/ Carbon Crossply Laminates," in Proc. ICCM-8, S. T. Tsai and G. S. Springer, Eds., Honolulu (1991).

23. WANG, H. and T. VU-KHANH, 1992 "Delamination Arrest Toughness in PEEK/Carbon Crossply Laminates under Low Velocity Impact," in Proc. 2nd International Symposium on Composite Materials and Structures, Beijing, China (1992).

24. WANG, H. and T. VU-KHANH, 1992 "Damage Extension in Carbon Fiber/ PEEK Crossply Laminates under Low Velocity Impact," (submitted to Journal of Composite Materials).

25. WANG, H. and T. VU-KHANH, "Mechanisms of Unstable Crack Growth of Impact-Induced Delamination," (to be submitted).

26. SJOBLOM, P. O., J. T. HARTNESS and T. M. CORDELL, 1988 "On Low-Velocity Impact Testing of Composite Materials," Journal of Composite Materi-

als, 22, 30-52.

27. LEE, S. M. and P. ZAHUTA, 1991 "Instrumented Impact and Static Indentation of Composites," Journal of Composite Materials, 25, 204-222.

28. POE, C. C., 1991 "Simulating Impact Damage in a Thick Graphite/Epoxy Laminate Using Spherical Indenters", Journal of Reinforced Plastics and Composites 10, 293-307.

29. LIU, D. and L. E. MALVERN, 1987 "Matrix Cracking in Impacted Glass/Epoxy Plates," Journal of Composite Materials, 21, 594-609.

30. MURTHY, P. L. N. and C. C. CHAMIS, 1986 "Dynamic Stress Analysis of Smooth and Notched Fiber Composite Flexural Specimens," in *Composite Materials: Testing and Design (Seventh Conference), ASTM STP 893*, pp. 368-391.

31. CANTWELL, W. J. and J. MORTON, 1989 "Geometrical Effects in the Low Velocity Impact Response of CFRP," Composite Structures, 12, 39-59.

32. CANTWELL, W. J., 1988 "The Influence of Target Geometry on the High Velocity Impact Response of CFRP," Composite Structures, 10, 247-265.

33. ROSS, C. A. and R. L. SIERAKOWSKI, 1973 "Studies on the Impact Resistance of Composite Plates," Composites, 4, 157-161.

34. VEDULA, M. and M. J. KOCZAK, 1989 "Impact Resistance of Cross-Plied Polyphenylene Sulfied Composites," Journal of Thermoplastic Composite Materials, 2, 154-163.

35. TAKEDA, N., R. L. SIERAKOWKI, C. A. ROSS and L. E. MALVERN, 1982 "Delamination-Crack Propagation in Ballistically Impacted Glass/Epoxy Composite Laminates," Experimental Mechanics, 22, 19-25.

36. TAKEDA, N., R. L. SIERAKOWSKI and L. E. MALVERN, 1981 "Wave Propagation Experiments on Ballistically Impacted Composite Laminates," Journal of Composite Materials, 15, 157-174.

37. MOORE, D. R. and R. S. PREDIGER, 1988 " A Study of Low-Energy Impact of Continuous Carbon-Fiber-Reinforced Composites," Polymer Composites, 9, 330-336.

38. CHOI. H. Y., R. J. DOWNS and F. -K. CHANG, 1991 "A New Approach toward Understanding Damage Mechanisms and Mechanics of Laminated Composites Due to Low-Velocity Impact: Part I-Experiments," Journal of Composite Materials, 25, 992-1011.

39. TAKEDA, N., R. L. SIERAKOWSKI and L. E. MALVERN, 1982 "Microscopic Observations of Cross Sections of Impacted Composite Laminates," Composite Technology Review, 4, 40-44.

40. SUN, C. T. and S. RECHAK, 1988 "Effect of Adhesive Layers on Impact Damage in Composite Laminates," in *Composite Materials: Testing and Design (Eighth Conference), ASTM STP 972*, pp. 97-123.

41. BOLL, D. J., W. D. BASCOM, J. C. WEIDNER and W. J. MURRI, 1986 "Impact Damage in Epoxy-Matrix Carbon-Fiber Composites," Journal of Material Science, 21, 2667-2677.

42. TAKEDA, N., R. L. SIERAKOWSKI and L. E. MALVERN, 1981 "Transverse Cracks in Glass/Epoxy Cross-ply Laminates Impacted by Projectiles," Journal of Material Science, 16, 2008-2011.

43. REIFSNIDER, K. L., 1990 "Damage and Damage Mechanics," in *Fatigue of Composite Materials*, K. L. Reifsnider Ed., Elsevier Science Publishers (1990).

44. FREEMAN, S. M., 1982 "Characterization of Interlaminar Damage in Graphite/Epoxy Composites by the Deply Technique," in *Composite Materials: Testing and Design (Sixth Conference), ASTM STP 787*, pp. 50-62.

45. WU, H.-Y. T. and G. S. SPRINGER, 1988 "Measurement of Matrix Cracking and Delamination Caused by Impact on Composite Plates," Journal of Composite Materials, 22, 518-532.

46. GUYNN, E. G. and T. K. O'BRIEN, 1985 "The Influence of Lay-up and Thickness on Composite Impact Damage and Compression Strength", in Proc. AIAA/

ASME/SAW 26th Structures, Structural Dynamics, and Materials Conference, Orlando (1985).

47. LIU, D., 1988 "Impact-Induced Delamination - A View of Bending Stiffness Mismatching," Journal of Composite Materials, 22 674-692.

48. MALVERN, L. E., C. T. SUN and D. LIU, 1989 "Delamination Damage in Central Impacts at Subperforation Speeds on Laminated Kevlar/Epoxy Plates," in *Composite Materials: Fatigue and Fracture, Second Volume, ASTM STP 1012*, pp. 387-405.

49. LIU, D., 1990 "Delamination Resistance in Stitched and Unstitched Composite Plates Subjected to Impact Loading," Journal of Reinforced Plastics and Composites, 9, 59-69.

50. GRADY, J. E. and C. T. SUN, 1986 "Dynamic Delamination Crack Propagation in a Graphite/Epoxy Laminate," *Composite Materials: Fatigue and Fracture*, ASTM STP 907, pp. 5-31.

51. CHAI, H., W. G. KNAUSS and C. D. BABCOCK, 1983 "Observation of Damage Growth in Compressively Loaded Laminates," Experimental Mechanics, 23, 329-337.

52. TAN, T. M. and C. T. SUN, 1985 "Use of Statical Indentation Laws in the Impact Analysis of Laminated Composite Plates," Journal of Applied Mechanics,

52, 6-12.

53. CAIRNS , D. S. and P. A. LAGACE, 1987 "Thick Composite Plates Subjected to Lateral Loading," Journal of Applied Mechanics, 54, 611-616.

54. SANKAR, B., 1989 " Interlaminar Shear Stresses in Composite Laminates Due to Static Indentation," Journal of Reinforced Plastics and Composites, 8, 458-471.

55. HARSHIN, Z., 1980 "Failure Criteria for Unidirectional Fiber Composites," Journal of Applied Mechanics, 47, pp. 329-334.

56. JERONIMIDIS, G. and A. T. PARKYN, 1988 "Residual Stresses in Carbon Fiber-Thermoplastic Matrix Laminates," Journal of Composite Materials, 22, 401-415.

57. FLAGGS, D. L. and M. H. KURAL, 1982 "Experimental Determination of In Situ Transverse Lamina Strength in Graphite/Epoxy Laminates, " Journal of Composite Materials, 16, 103-116.

58. GILLESPIE, J. W. Jr., L. A. CARLSSON and R. B. PIPES, 1986 "Finite Element Analysis of the End Notched Flexure Specimen for Measuring Mode II Fracture Toughness," Composites Science and Technology, 27, 177-197.

59. BROEK, D., *Elementary Engineering Fracture Mechanics*, Martinus Nijhoff

Publishers (1986).

60. FRIEDRICH, K., *Application of Fracture Mechanics to Composite Materials*, Elsevier Science Publishers (1989).

61. NEWAZ, G. M., *Delamination in Advanced Composites*, Technomic Publishing Company (1991).

62. LU, X. and D. LIU, 1991 "Finite Element Analysis of Strain Energy Release Rate at Delamination Front," Journal of Reinforced Plastics and Composites, 9, 279-292.

63. S. N. CHATTERJEE, W. A. DICK and R. B. PIPES, 1986 "Mixed-Mode Delamination Fracture in Laminated Composites," Composites Science and Technology, 25, 49-67.

64. SUN, C. T. and J. E. GRADY, 1988 "Dynamic Delamination Fracture Toughness of a Graphite/Epoxy Laminate under Impact," Composites Science and Technology, 31, 55-72.

65. GRADY, J. E., C. C. CHAMIS and R. A. AIELLO, 1989 "Dynamic Delamination Buckling in Composite Laminates under Impact Loading: Computational Simulation," in *Composite Materials: Fatigue and Fracture, Second Volume, ASTM STP 1012*, pp. 137-149.

66. MAIKUMA, H., J. W. GILLESPIE, Jr. and D. J. WILKINS, 1990 "Mode II Interlaminar Fracture of the Center Notch Flexural Specimen under Impact Loading," Journal of Composite Materials, 24, 124-147.

67. SANKAR, B. V. and S. HU, 1991 "Dynamic Delamination Propagation in Composite Beams," Journal of Composite Materials, 25, 1414-1426.

68. SMILEY, A. J. and R. B. PIPES, 1987 "Rate Sensitivity of Mode II Interlaminar Fracture Toughness in Graphite/Epoxy and Graphite/PEEK Composite Materials," Composites Science and Technology, 29, 1-15.

69. SMILEY, A. J. and R. B. PIPES, 1987 "Rate Effects on Mode I Interlaminar Fracture Toughness in Composite Materials," Journal of Composite Materials, 21, 670-687.

70. LINGG, C. L., S. MALL and S. L. DONALDSON, 1989 "Loading Rate Effect on Mode III Delamination Fracture Toughness of Graphite/Epoxy," in Proc. of the American Society for Composites (1989).

71 CAIRNS, D. S., 1992 "Static and Dynamic Mode II Strain Energy Release Rates in Toughened Thermosetting Composite Laminates," Journal of Composites Technology & Research, 14, 37-42.

72. VU-KHANH, T., 1987 "Crack-Arrest Study in Mode II Delamination in Composites," Polymer Composites, 8, 331-341.

73. WANG, H and T. VU-KHANH, 1993 "Large Deflection Correction for Mode II Toughness Measurement of Composite Materials" (accepted by ICCM-9).

74. CURTIS, P. T., 1987 "An Investigation of the Mechanical Properties of Improved Carbon Fibre Composite Materials," Journal of Composite Materials, 21, 1118-1144.

75. Property Data of Aromatic Polymer Composites, APC-2/Hercules Mangnamite AS4 Carbon Fiber, ICI, Inc.

76. BERNARD, C., J. DENAULT, J. DUFOUR and T. VU-KHANH, *IMI/NRCC Report 89RT-103-865-C.*

77. KIM, K. S., H. T. HAHN and R. B. CROMAN, 1989 "The Effect of Cooling Rate on Residual Stress in a Thermoplastic Composite," Journal of Composite Technology & Research, 11, 47-52.

78. CHAI, H., 1990 "Interlaminar Shear Fracture of Laminated Composites," International Journal of Fracture, 43, 117-131.

79. MASTERS, J. E., 1987 "Characterization of Impact Damage Development in Graphite/Epoxy Laminates", in *Fractography of Modern Engineering Materials: Composites and Metals, ASTM STP 948,* pp. 238-258.

80. ABAQUS User's Manual, Version 4.7, Hibbitt, Karlsson & Sorensen Inc.(1989).

81. TSAI, S. W. and H. T. HAHN, *Introduction to Composite Materials*, Technomic Publishing Company (1980).

82. REDDY, J. N. and E. J. BARBERO, 1989 "A Plate Bending Element Based on a Generalized Laminate Plate Theory," International Journal for Numerical Methods in Engineering, 28 2275-2292.

83. PAGANO, N. J. and S. J. HATFIELD, 1972 "Elastic Behavior of Multilayered Bidirectional Composites," AIAA Journal, 10, 931-933.

84. YANIV, G., G. PEIMANIDIS and I. M. DANIEL, 1989 "Environmental Effects on High Strain Rate Properties of Graphite/Epoxy Composite," in *Test Methods for Design Allowables for Fibrous Composites: 2nd Volume*, ASTM STP 1003, pp. 16-30.

85. ROSS, C. A., L. E. MALVERN, R. L. SIERAKOWSKI and N. TAKEDA, 1985 "Finite-Element Analysis of Interlaminar Shear Stress Due to Local Impact," in *Recent Advances in the United States and Japan*, ASTM STP 864, pp. 355-367.

86. VU-KHANH, T., R. LANGLOIS and R. GAUVIN, 1989, "Influence of Ply Orientation on the Measurement of Mode II Delamination," in Proc. ICCM-7, Y. Wu, Z. Gu and R. Wu Eds., Guangzhou, China (1989).

87. VU-KHANH, T. and F. X. DE CHARENTENAY, 1985 "Mechanics and

Mechanisms of Impact Fracture in Semi-Ductile Polymers," Polymer Engineering & Science, 25 841-850.

88. VU-KHANH, T. and B. FISA, 1990 "Effects of Fillers on Fracture Performance of Thermoplastics: Strain Energy Density Criterion," Theoretical & Applied Fracture Mechanics, 13, 11-19.

89. NAIRN, J. A., S. LIU and H. CHEN, 1991 "Longitudinal Splitting in Epoxy and K-Polymer Composites: Shear Lag Analysis Including the Effect of Fiber Bridging," Journal of Composite Materials, 25, 1086-1107.

90. WILT, T. E., P. L. N. MURTHY and C. C. CHAMIS, 1989 " Fracture Toughness Computational Simulation of General Delaminations in Fiber Composites," Journal of Reinforced Plastics and Composites, 8, 2-17.

91. F. -K. CHANG and L. B. LESSARD, 1991 "Damage Tolerance of Laminated Composites Containing an Open Hole and Subjected to Compressive Loadings: Part I-Analysis," Journal of Composite Materials, 25, 2-43.

92. KALTHOFF, J. F., J. BEINERT, J., S. WINKLER and W. KLEMM, 1980 "Experimental Analysis of Dynamic Effects in Different Crack Arrest Test Specimens," in *Crack Arrest Methodology and Applications, ASTM STP 711*, pp. 109-127.

93. CROSLEY, P. B. and E. J. RIPLING, 1980 "Significance of Crack Arrest

Toughness (K_{Ia}) Testing," in *Crack Arrest Methodology and Applications*, ASTM STP 711, pp. 321-337.

94. IRWIN, G. R., "Comments on Dynamic Fracturing," *Fast Fracture and Crack Arrest, ASTM STP 627*, pp. 7-18.

95. MAICUMA, H., J. W. GILLESPIE Jr. and A. J. WHITNEY, 1989 "Analysis and Exprimental Characterization of the Center Notched Flexural Test Specimen for Mode II Interlaminar Fracture," Journal of Composite Materials, 23, 756-786.

96. RUSSELL, A. J., 1991 "Initiation and Growth of Mode II Delamination in Toughened Composites", in *Composite Materials: Fatigue and Fracture (Third Volume), ASTM STP 1110*, pp. 226-242.

97. BRADLEY, W. L., Presentation at ASTM Task Group Meeting, Committee D-30, Charleston, SC. April 30 (1986).

98. WILLIAMS, J. G., 1989 "Fracture Mechanics of Anisotropic Materials," in *Application of Fracture Mechanics to Composite Materials*, K. Friedrich Ed., Elsevier Science Publishers, pp. 3-38.

99. CARLSSON, L. A., J. W. GILLESPIE and B. R. PIPES, 1986 "Mode II Interlaminar Fracture of Graphite/Epoxy and Graphite/PEEK", Journal of Reinforced Plastics and Composites, 5, 170-187.

100. WILLIAMS, J. G., 1987 "Large Displacement and End Block Effects in the 'DCB' Interlaminar Test in Modes I and II," Journal of Composite Materials, 21, 330-348.

101. RUSSELL, A. J. and K. N. STREET, 1982 "Factors Affecting the Interlaminar Fracture Energy of Graphite/Epoxy Laminates," in Proc. ICCM-IV, Tokyo (1982).

102. FREEMAN, J. G., Phil. Mag., 37 (1947).

103. ACTON, F. S., *Numerical Methods That Work*, Harper and Row (1970).

104. ABRAMOWITZ, M. and I. A. STEGUN, *Hand Book of Mathematical Functions with Formulas, Graphs, and Mathematical Tables*, National Bureau of Standards (1964).

105. WILLIAMS, J. G., 1988 "On the Calculation of Energy Release Rates for Cracked Laminates," International Journal of Fracture, 36, 101-119.

Appendix A

Large Deflection Analysis of End-Loaded-Split Fracture Test

A.1 Objective

When the end-loaded-split (ELS) fracture test, Fig. A.1a, is used to measure the Mode II delamination toughness of tough or less rigid composites, a large deflection may be required to initiate the fracture. The data reduction procedure based on linear beam theory analysis, i.e. Eqs. 8.4 or 8.5, needs to be corrected to eliminate the large deflection effect.

Large deflection analysis of ELS specimen has been studied by Williams (98, 100). The ELS specimen in (98, 100) is modified from its original form (Fig. A.1a) to include an end block as shown in Fig. A.1c. And the correction to strain energy release rate is only given for two limiting cases: $a/L \rightarrow 0$ and $a/L \rightarrow 1$, where a and L are the crack length and the span of the specimen respectively.

In this appendix, the original ELS specimen is analyzed by nonlinear beam theory. Large deflection corrections to strain energy release rate are obtained for all range of crack length. The effect of large deflection on fracture stability is also discussed.

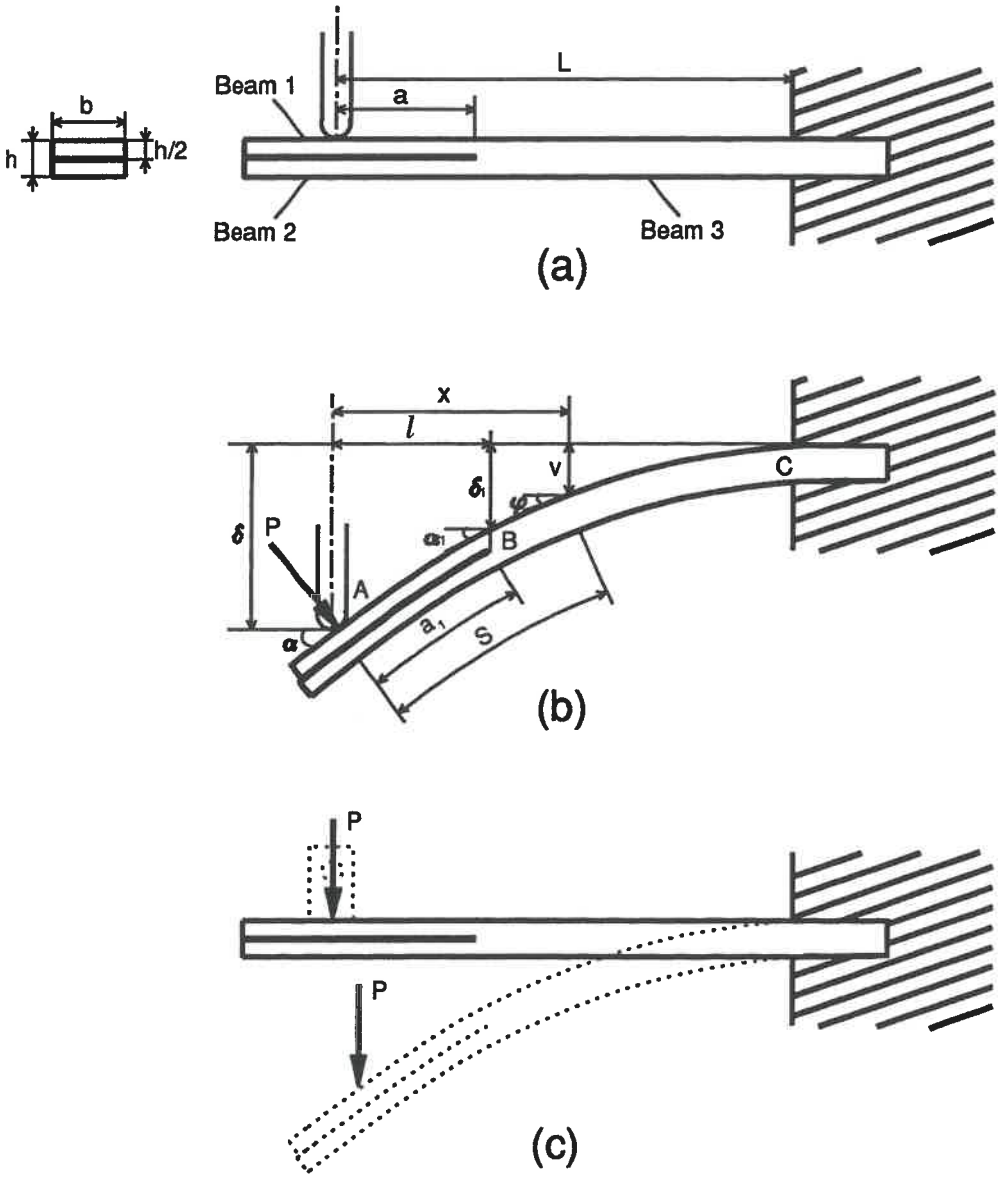

Figure A.1 Geometry of end-loaded-split (ELS) specimen: (a) before deformation; (b) after deformation; (c) modified ELS specimen [98, 100].

A.2 Large Deflection Analysis

A.2.1 Problem Formulation

The ELS specimen in Fig. A.1a can be separated into three parts: the cracked parts (Beams 1 and 2) and the uncracked part (Beam 3). The sample geometry before deformation is defined by the span L, crack length a, width b and total thickness h. The delamination is located at the midplane. The deformed configuration is shown in Fig. A.1b. In the coordinate system assumed, any section of the beam can be determined by the Cartesian coordinate x, the distance from load point S, or the angle of slope φ. The beam deflection is denoted by v. Boundary conditions of the deflected specimen can be specified as follows. At the load point (Point A)

$$x = 0,\ S = 0,\ \varphi = \alpha \ \text{ and } \ v = \delta \tag{A.1}$$

At the crack tip (Point B)

$$x = l,\ S = a_1,\ \varphi = \alpha_1 \ \text{ and } \ v = \delta_1 \tag{A.2}$$

and, at the clamped end (Point C)

$$x = L,\ S = L + (a_1 - a),\ \varphi = 0 \ \text{ and } \ v = 0. \tag{A.3}$$

If the friction between the load nose and beam surface is neglected, load P acts normally to the contact point. The bending moment at any section of the specimen can be expressed as

$$M = - P\,[x \cos\alpha + (\delta - v) \sin\alpha] \tag{A.4}$$

The bending moment in the uncracked part: $M_3 = M$, and in the cracked parts: $M_1 + M_2 = M$.

For slender beam specimens, the deformation is mainly due to bending. It is also assumed that the beam is under small strain level and the material obeys linear elastic stress-strain relation. Consequently, the elementary beam equation holds, i.e.

$$\frac{1}{R} = \frac{M}{E_f I} \tag{A.5}$$

where R is the radius of curvature of the deflected beam axis, E_f is the effective flexural modulus (72) and I is the area moment of inertia of the beam section. For the uncracked part: $I = bh^3/12$, while for the cracked parts: $I_1 = I_2 = I/8$.

Eq. A.5 is generally nonlinear in the large deflection situation. Freeman (102) proposed a method for solving Eq. A.5 by using the angle of slope φ as the basic variable. The method has been applied to analyzing the cracked beam specimens in (100). Consider a small beam element dS as shown in Fig. A.2, the increment of beam parameters may be expressed in terms of φ, i.e.

$$dS = R\, d\varphi \tag{A.6}$$

$$dx = R \cos\varphi\, d\varphi \tag{A.7}$$

$$dv = -R \sin\varphi\, d\varphi \tag{A.8}$$

and from the latter two equations

$$\frac{dv}{dx} = -tg\varphi \tag{A.9}$$

It is worth noting that the sign of each term in the above equations must be correctly

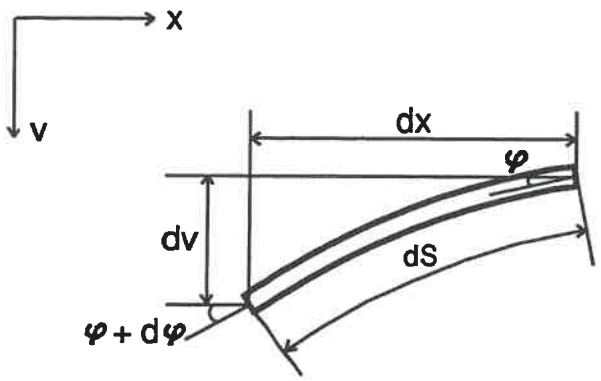

Figure A.2 Geometry of a beam element.

specified with respect to the coordinate system assumed. With $R < 0$ in the present case, $d\varphi > 0$ corresponds to $dS < 0$, $dx < 0$ and $dv > 0$, being consistent with Eqs. A.6 to A.9.

A.2.2 Solution to the Cracked Parts

Consider the cracked parts of the specimen. Under bending, deflections of the two arms are compatible with each other, so the same curvature exists in both arms. According to Eq. A.5, the same bending moment must act in both arms, i.e. $M_1 = M_2 = M/2$. Therefore it is only necessary to study Beam 1.

Eq. A.5 can be written for Beam 1 in the form

$$\frac{1}{R_1} = -\frac{P}{2E_f I_1}[x\cos\alpha + (\delta - v)\sin\alpha] \tag{A.10}$$

By differentiating Eq. A.10 with x and then substituting Eq. A.9, we can express R_1 using φ as the basic variable, i.e.

$$\frac{1}{R_1^2}\frac{dR_1}{dx} = \frac{P}{2E_f I_1}[\cos\alpha + \sin\alpha\, tg\varphi] \tag{A.11}$$

Eq. A.11 is then integrated to give

$$\frac{1}{R_1^2} = \frac{1}{R_1^2(A)} + \frac{P}{E_f I_1}\sin(\alpha - \varphi) \tag{A.12}$$

At the load point, $1/R_1(A) = 0$, because $M_1(A) = 0$. Consequently,

$$R_1 = -\sqrt{\frac{E_f I_1}{P}}\,\frac{1}{\sqrt{\sin(\alpha - \varphi)}} \tag{A.13}$$

where $\alpha_1 < \varphi < \alpha$. The minus sign is taken in Eq. A.13 in order to be consistent with Eq. A.10. At the crack tip, a useful relation is obtained by substituting Eq. A.13 into Eq. A.10

$$l\cos\alpha + (\delta - \delta_1)\sin\alpha = 2\sqrt{\frac{E_f I_1}{P}}\,\sqrt{\sin(\alpha - \alpha_1)} \tag{A.14}$$

Now, with R_1 given by Eq. A.13, all beam parameters in Beam 1 (and Beam 2) may be obtained by integrating Eqs. A.6 to A.8 with respect to φ. For a beam element dS_1

$$dS_1 = -\sqrt{\frac{E_f I_1}{P}}\,\frac{d\varphi}{\sqrt{\sin(\alpha - \varphi)}} \tag{A.15}$$

its coordinates and deflection are given as

$$x = \sqrt{\frac{E_f I_1}{P}}\int_{\varphi}^{\alpha}\frac{\cos\xi\, d\xi}{\sqrt{\sin(\alpha - \xi)}} \tag{A.16}$$

$$S = \sqrt{\frac{E_f I_1}{P}}\int_{\varphi}^{\alpha}\frac{d\xi}{\sqrt{\sin(\alpha - \xi)}} \tag{A.17}$$

$$v = \delta - \sqrt{\frac{E_f I_1}{P}}\int_{\varphi}^{\alpha}\frac{\sin\xi\, d\xi}{\sqrt{\sin(\alpha - \xi)}} \tag{A.18}$$

where $\alpha_1 < \varphi < \alpha$. At the crack tip in particular, Eq. A.2 results in

$$a_1 = \sqrt{\frac{E_f I_1}{P}} \int_{\alpha_1}^{\alpha} \frac{d\varphi}{\sqrt{\sin(\alpha - \varphi)}} \tag{A.19}$$

$$l = \sqrt{\frac{E_f I_1}{P}} \int_{\alpha_1}^{\alpha} \frac{\cos\varphi \, d\varphi}{\sqrt{\sin(\alpha - \varphi)}} \tag{A.20}$$

$$\delta - \delta_1 = \sqrt{\frac{E_f I_1}{P}} \int_{\alpha_1}^{\alpha} \frac{\sin\varphi \, d\varphi}{\sqrt{\sin(\alpha - \varphi)}} \tag{A.21}$$

A.2.3 Solution to the Uncracked Part

Similar analysis can be made for the uncracked part. Eq. A.5 is integrated for Beam 3 to give

$$\frac{1}{R_3^2} = \frac{1}{R_3^2(B)} - \frac{2P}{E_f I} [\sin(\alpha - \alpha_1) - \sin(\alpha - \varphi)] \tag{A.22}$$

where $1/R_3(B)$ can be determined from the bending moment at the crack tip. With Eqs. A.4 and A.14, it is found that

$$\frac{1}{R_3^2(B)} = \frac{P}{2E_f I} \sin(\alpha - \alpha_1) \tag{A.23}$$

Hence

$$R_3 = -\sqrt{\frac{2E_f I}{P}} \frac{1}{\sqrt{4\sin(\alpha - \varphi) - 3\sin(\alpha - \alpha_1)}} \tag{A.24}$$

A set of relations similar to Eqs. A.15 to A.18 are also obtained for the uncracked part of the specimen. These include

$$dS_3 = -\sqrt{\frac{2E_f I}{P}}\,\frac{d\varphi}{\sqrt{4\sin(\alpha - \varphi) - 3\sin(\alpha - \alpha_1)}} \tag{A.25}$$

$$x = l + \sqrt{\frac{2E_f I}{P}}\int_{\varphi}^{\alpha_1} \frac{\cos\xi\, d\xi}{\sqrt{4\sin(\alpha - \xi) - 3\sin(\alpha - \alpha_1)}} \tag{A.26}$$

$$S = a_1 + \sqrt{\frac{2E_f I}{P}}\int_{\varphi}^{\alpha_1} \frac{d\xi}{\sqrt{4\sin(\alpha - \xi) - 3\sin(\alpha - \alpha_1)}} \tag{A.27}$$

$$v = \delta_1 - \sqrt{\frac{2E_f I}{P}}\int_{\varphi}^{\alpha_1} \frac{\sin\xi\, d\xi}{\sqrt{4\sin(\alpha - \xi) - 3\sin(\alpha - \alpha_1)}} \tag{A.28}$$

where $0 < \varphi < \alpha_1$.

From the above solutions, the boundary conditions at the clamped end, Eq. A.3, may be expressed as

$$L - a = \sqrt{\frac{2E_f I}{P}}\int_{0}^{\alpha_1} \frac{d\varphi}{\sqrt{4\sin(\alpha - \varphi) - 3\sin(\alpha - \alpha_1)}} \tag{A.29}$$

$$L = \sqrt{\frac{2E_f I}{P}}\int_{0}^{\alpha_1} \frac{\cos\varphi\, d\varphi}{\sqrt{4\sin(\alpha - \varphi) - 3\sin(\alpha - \alpha_1)}} + \sqrt{\frac{E_f I}{8P}}\int_{\alpha_1}^{\alpha} \frac{\cos\varphi\, d\varphi}{\sqrt{\sin(\alpha - \varphi)}} \tag{A.30}$$

$$\delta = \sqrt{\frac{2E_f I}{P}}\int_{0}^{\alpha_1} \frac{\sin\varphi\, d\varphi}{\sqrt{4\sin(\alpha - \varphi) - 3\sin(\alpha - \alpha_1)}} + \sqrt{\frac{E_f I}{8P}}\int_{\alpha_1}^{\alpha} \frac{\sin\varphi\, d\varphi}{\sqrt{\sin(\alpha - \varphi)}} \tag{A.31}$$

The first two equations imply that, for a given α, P and α_1 are determined by the geometry conditions that require a constant distance between the load line and the clamped end, and a constant length of the uncracked part of the specimen. All other parameters of the deflected beam may be calculated from α, α_1 and P using Eqs. A.15 to A.18 and A.25 to A.28. Therefore Eqs. A.29 and A.30 are the controlling equations of the problem.

In the case of small deflections, the following approximations exist: $sin\varphi \approx \varphi$, $cos\,\varphi \approx 1$. The integrals in Eqs. A.29 to A.31 may be evaluated explicitly. It is found that

$$\alpha_1 = \frac{P(L^2 - a^2)}{2E_f I} \tag{A.32}$$

$$\alpha = \frac{P(L^2 + 3a^2)}{2E_f I} \tag{A.33}$$

Substitution of these relations to Eq. A.31 results in the compliance expression by linear beam theory, Eq. 8.3.

In the case of large deflections, α_1 can be considered as the basic unknown. Eqs. A.29 and A.30 are combined to eliminate P, and α_1 is determined using the Newton-Raphson method (103). The integrals are evaluated numerically. Since an integratable singularity exists at $\varphi = \alpha$ in the integrands with $1/\sqrt{sin(\alpha - \varphi)}$, the following quadrature was used (104)

$$\int_{-1}^{1} f(x)dx = \frac{\pi}{n}\sum_{k=1}^{n} sin(\frac{2k-1}{2n}\pi)\, f[cos(\frac{2k-1}{2n}\pi)] \tag{A.34}$$

In addition, the following dimensionless parameters are introduced in the solution

procedure:

$$\bar{a} = \frac{a}{L} \ , \quad \bar{P} = \frac{PL^2}{E_f I} \ , \quad \bar{\delta} = \frac{\delta}{L} \ . \tag{A.35}$$

A.3 Large Deflection Response

Fig. A.3 shows the load-deflection response of an ELS specimen with $a/L = 0.5$. The test measurement on APC-2 composite, Fig. 8.2b, is also plotted for comparison. The load is normalized by $L^2/E_f I$ and the deflection by L. The close agreement between test data and predicted curve verifies the analysis. Also shown in the figure are $\bar{P}_x$ and $\bar{P}_y$, the horizontal and vertical components of $\bar{P}$. $\bar{P}_y$ follows $\bar{P}$ at first and it gradually deviates from $\bar{P}$ and declines as the sample deflects. $\bar{P}_x$ gradually builds up from zero and approaches $\bar{P}$ with increasing deflection. At $\alpha = \pi/2$, $\bar{P}_y = 0$ and $\bar{P}_x = \bar{P}$, i.e. the beam axis becomes vertical at the load point and the load is applied laterally in the x-direction. It is significant to note this point because, during testing, the load cell is more sensitive to $\bar{P}_y$ and much less so to $\bar{P}_x$, thus the load may not be reliably measured if the specimen deflects well into the nonlinear range. For the APC-2 specimen, the load follows $\bar{P}$ up to fracture. So the critical load P_{cr} has been used in Chapter 8 for toughness calculation. It could be expected that, in testing composites with tougher matrix and less rigid reinforcement, the deflection at fracture δ_{cr} may be so large that P_{cr} could not be correctly measured. In that case, using δ_{cr} for toughness calculation may be a suitable approach.

Previous studies (105) have shown that the bending moment at crack tip, $M(l)$, determines the strain energy release rate. In small deflection situations, the moment is

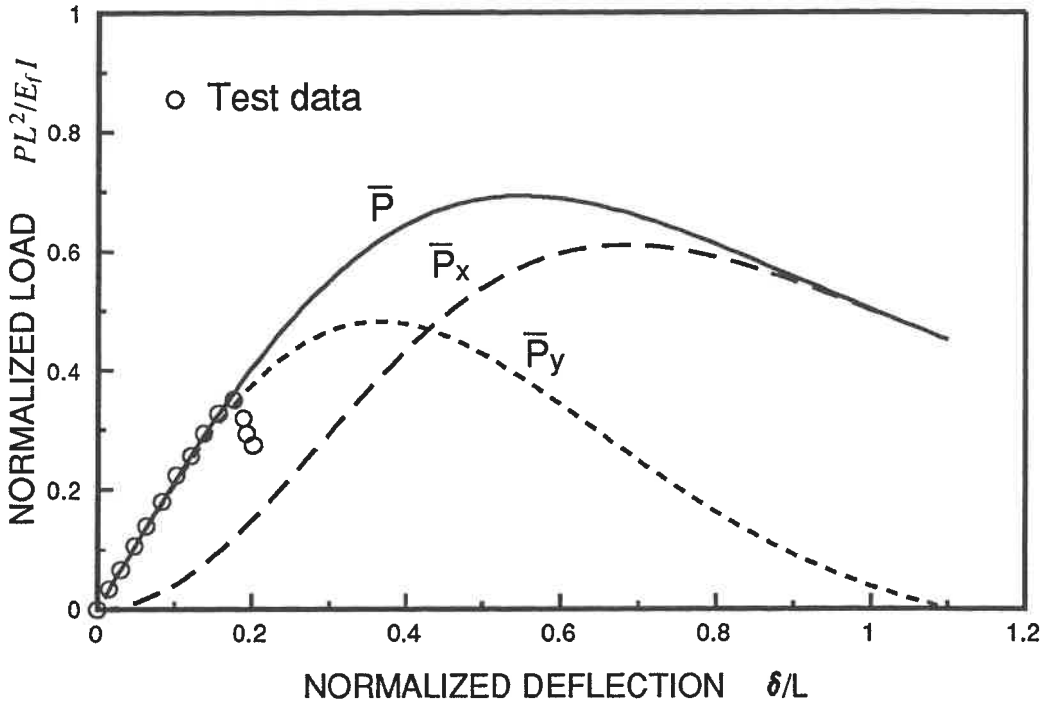

Figure A.3 Load-deflection response of ELS specimen ($a/L = 0.5$).

determined from the vertical load and the original crack length, i.e.

$$M_s(a) = Pa \tag{A.36}$$

In large deflection situations, the moment includes the contributions from both $\bar{P}_x$ and $\bar{P}_y$. Using Eqs. A.4 and A.14, $M(l)$ can be expressed as

$$M(l) = \sqrt{\frac{PE_f I}{2}} \sin(\alpha - \alpha_1) \tag{A.37}$$

Fig. A.4 compares $M(l)$ and $M_s(a)$, both are normalized by $(E_f I/L)$. Under a given load, $M(l)$ is underestimated by the linear analysis.

Fig. A.5 shows the actual crack length a_1 versus deflection for a/L = 0.2, 0.5 and 0.8. The crack length, and thus the beam length under load, increases with increasing deflection. The variation also depends on the initial crack length. Therefore, when the crack extends in the deflected configuration, the system becomes non-constant in the sense that the beam length under load varies.

A.4 Strain Energy Release Rate

The above analyses reveal that the ELS specimen is nonlinear and non-constant when the crack grows at a large deflection. According to Griffith's energy theory of fracture, the strain energy release rate G of a cracked solid is defined as the energy released by the system when the crack extends to create a unit area of fracture surface (59). Therefore, G may be determined by differentiating the strain energy U with respect to crack length at a fixed deflection, i.e.

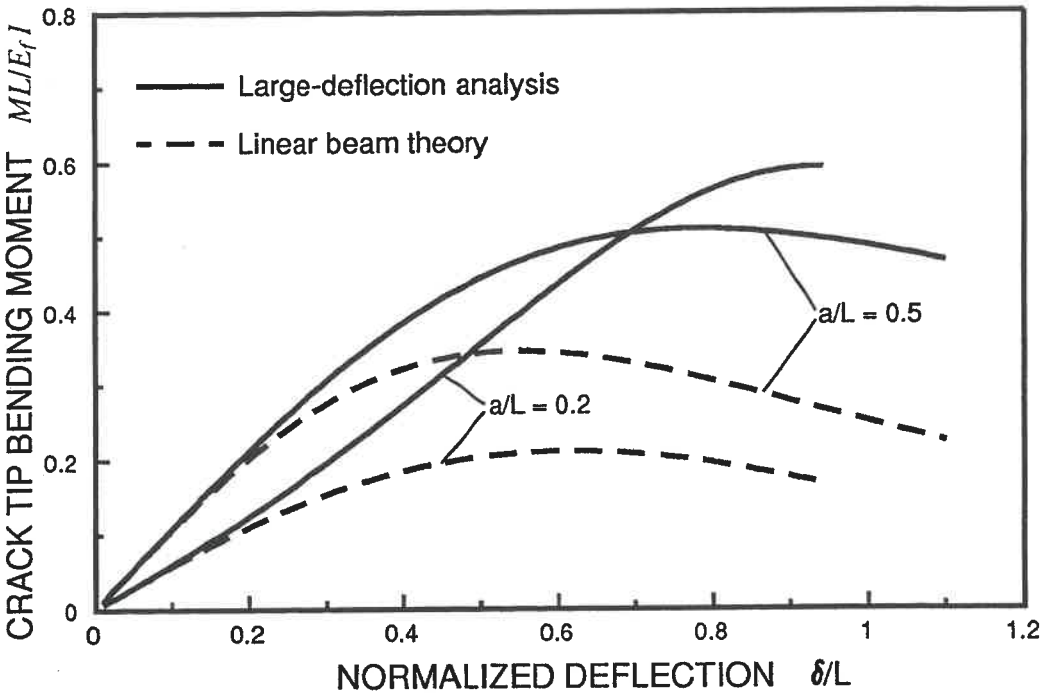

Figure A.4 Comparison of crack tip bending moments predicted by linear and nonlinear beam theories.

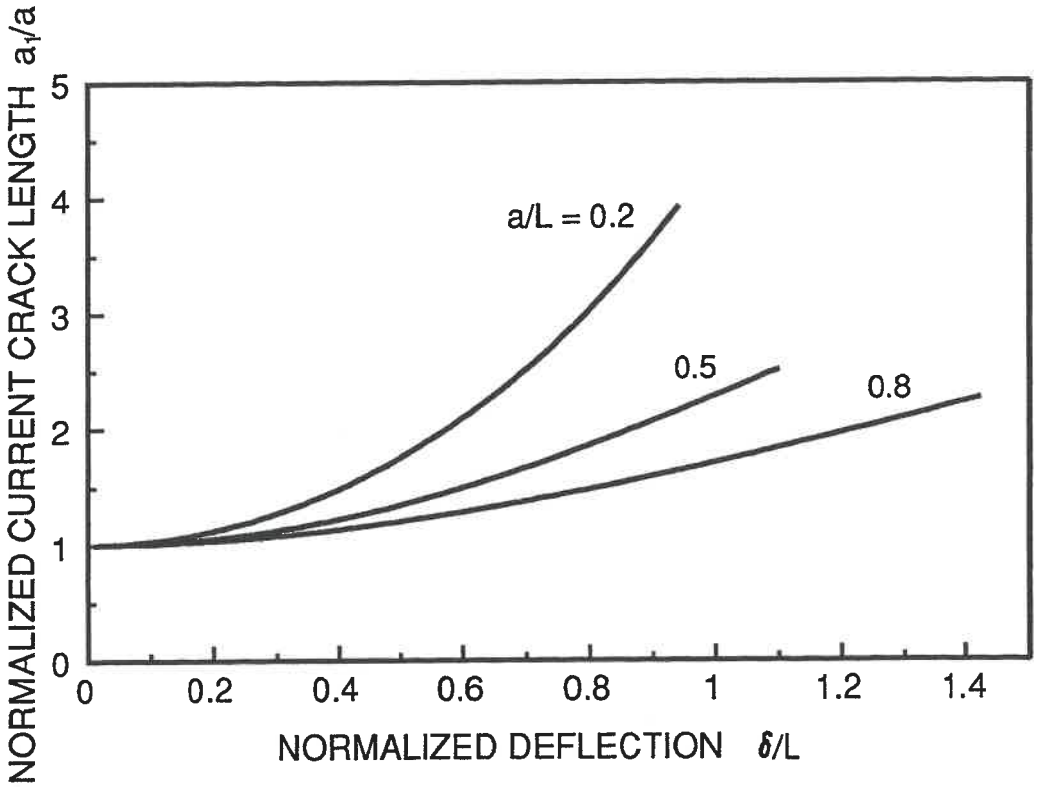

Figure A.5 Current crack length (from load point to crack tip at deflected configuration) as a function of specimen deflection.

$$G = -\frac{1}{b}\frac{\partial U}{\partial a}_{(\delta = \text{constant})} \tag{A.38}$$

where the beam width b is uniform throughout the specimen.

For a beam element dS, the strain energy due to bending deformation is given by

$$dU = \frac{M^2}{2E_f I} \tag{A.39}$$

So the total energy U is obtained by integrating Eq. A.39 over each part of the ELS specimen. U can be expressed as

$$U = \int_0^{a_1} \frac{2M^2}{E_f I}\, dS_1 + \int_{a_1}^{L+a_1-a} \frac{M^2}{2E_f I}\, dS_3 \tag{A.40}$$

where dS_1 and dS_3 are given in Eqs. A.15 and A.25. Therefore the Mode II strain energy release rate G_{II} may be determined by evaluating the increment in U associated with a crack extension Δa, i.e.

$$G_{II} = -\frac{1}{b}\frac{U(a+\Delta a) - U(a)}{\Delta a} \tag{A.41}$$

Numerical analyses show that $\Delta a = 0.001a$ gives convergent results.

Williams (98, 100, 105) suggested a "local moment method" for calculating the strain energy release rate. The method is based on the energy change due to crack growth in a small beam element ahead of the crack tip. In a cracked beam specimen under bending, G_{II} is found to depend on the crack-tip bending moment $M(l)$. When the crack is placed at midplane, G_{II} is generally given in the form:

$$G_{II} = \frac{3M^2(l)}{2bE_f I} \tag{A.42}$$

For the ELS specimen under small deflections,

$$G_{II}^s(P) = \frac{3P^2a^2}{2bE_f I} \tag{A.43}$$

When $P = P_{cr}, G_{II}^s(P)$ is identical to Eq. 8.4. Under large deflections,

$$G_{II} = \frac{3P\ sin(\alpha - \alpha_1)}{4b} \tag{A.44}$$

The local moment method considers only the energy change at the crack tip. It needs to be verified for the ELS specimen because the beam length varies during crack growth, which also changes the stored energy.

Table A.1 Comparison of strain energy release rate calculation methods

$a/L = 0.5$		
α (deg)	$G_{II}\,bL^2/E_f I$ (Eq. A.41)	$G_{II}\,bL^2/E_f I$ (Eq. A.44)
10	0.0148	0.0148
20	0.0576	0.0576
30	0.1233	0.1232
40	0.2030	0.2029
50	0.2841	0.2838
60	0.3506	0.3497
70	0.3862	0.3851
80	0.3789	0.3777
90	0.3269	0.3261

Table A.1 compares the strain energy release rate calculated from the total bending energy by Eq. A.41 and that from the local moment method by Eq. A.44. For the typical case ($a/L = 0.5$), G_{II} is slightly underestimated by the local moment method. But the error is negligibly small. The same observation is true for other crack lengths. So the local moment method can be used for the ELS specimen under large deflections.

Another point requiring verification is that only the bending strain energy is considered in the G_{II} calculation. Fig. A.6 compares the measured strain energy and the bending energy predicted by Eq. A.40. The test data follow closely the prediction but seem to be slightly underestimated. This may be attributed to neglecting the shear and stretching energies in Eq. A.40. It has been demonstrated (72) that the shear energy does not contribute to the energy release rate during crack growth because it is not related to the crack length. In the present study, this is verified by measuring the energy variation over a range of crack length at a constant deflection. As shown in Fig. A.7, the energy data agree very well with the curve that is shifted by a constant from the predicted bending energy. Therefore, within the assumption of beam theory, it is appropriate to calculate G_{II} from the bending strain energy.

It should be noted that, although the shear strain energy estimated by beam theory is not associated with crack growth (72), the significant shear deformation at the crack tip is (58). Such local effects can be accounted for by using advanced stress analysis techniques (58). This is beyond the scope of the present study.

Fig. A.8 compares the strain energy release rate by nonlinear beam theory to that by linear theory. For $a/L > 0.3$, G_{II} is underestimated by Eqs. A.43 or 8.4 using load for the calculation, while it is overestimated by Eq. 8.5 using deflection. For a shorter crack length, however, linear theory underestimates G_{II} using either load or

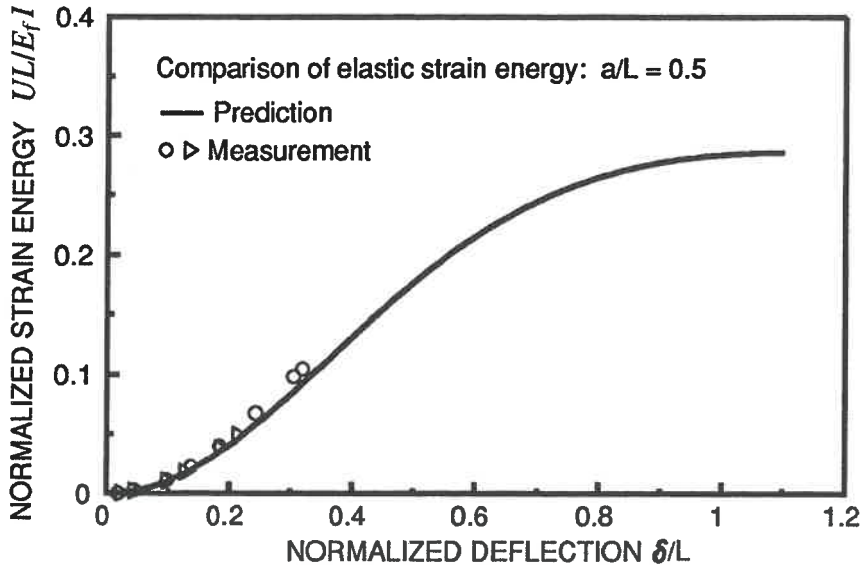

Figure A.6 Strain energy in PEEK/Carbon (APC-2) ELS specimens as a function of deflection.

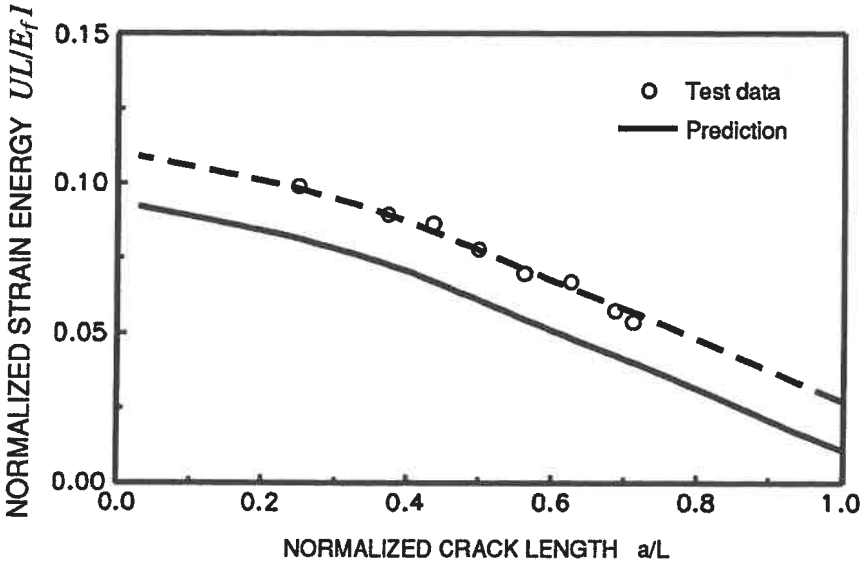

Figure A.7 Strain energy in a PEEK/Carbon (APC-2) ELS specimen as a function of crack length (under a given deflection).

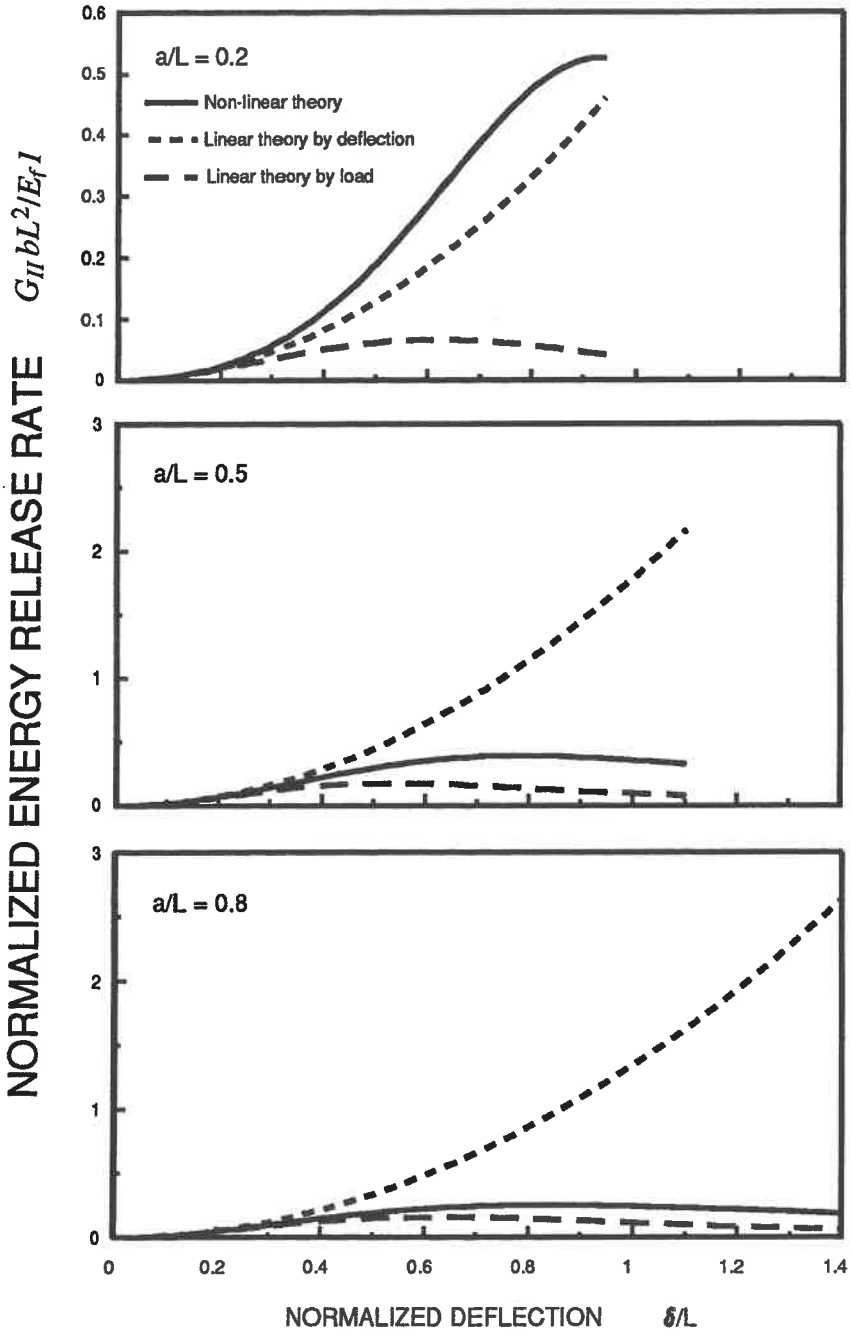

Figure A.8 Comparison of strain energy release rates in ELS specimen calculated by linear and non-linear beam theories.

deflection in the calculation. In all cases, it is significant to correct the strain energy release rate by linear beam theory if the specimen is subject to a large deflection.

A.5 Large Deflection Correction Factor

Large deflection effects on strain energy release rate can be eliminated by providing corrections to the linear theory results. When load is used for calculating G_{II}, the correction factor is defined as

$$F_P = \frac{G_{II}}{G_{II}^s(P)} \tag{A.45}$$

If deflection is used for the calculation, the correction factor is

$$F_\delta = \frac{G_{II}}{G_{II}^s(\delta)} \tag{A.46}$$

where $G_{II}^s(\delta)$ is given by Eq. 8.5. The correction factors F_P and F_δ have been plotted in Figs. 8.3 and 8.4 respectively for different crack lengths. The values are also tabulated in Appendix B for reference.

It is noted that the correction factor for Eqs. A.43 or 8.4 has been proposed in (98) for the modified ELS specimen (Fig. A.1c). The correction factor was given in explicit form for two limiting cases, assuming zero height of the end block, i.e.

$$F_p^* \approx cos^2\alpha \quad (a/L \to 0) \tag{A.47}$$

$$F_p^* \approx 1 - \frac{15 + 50(a/L)^2 + 63(a/L)^4}{1 + 6(a/L)^2 + 9(a/L)^4} \frac{3}{20} \left(\frac{\delta}{L}\right)^2 \quad (a/L \to 1) \tag{A.48}$$

Fig. A.9 compares F_p^* with F_p in the typical cases. The difference between F_p^* and F_p

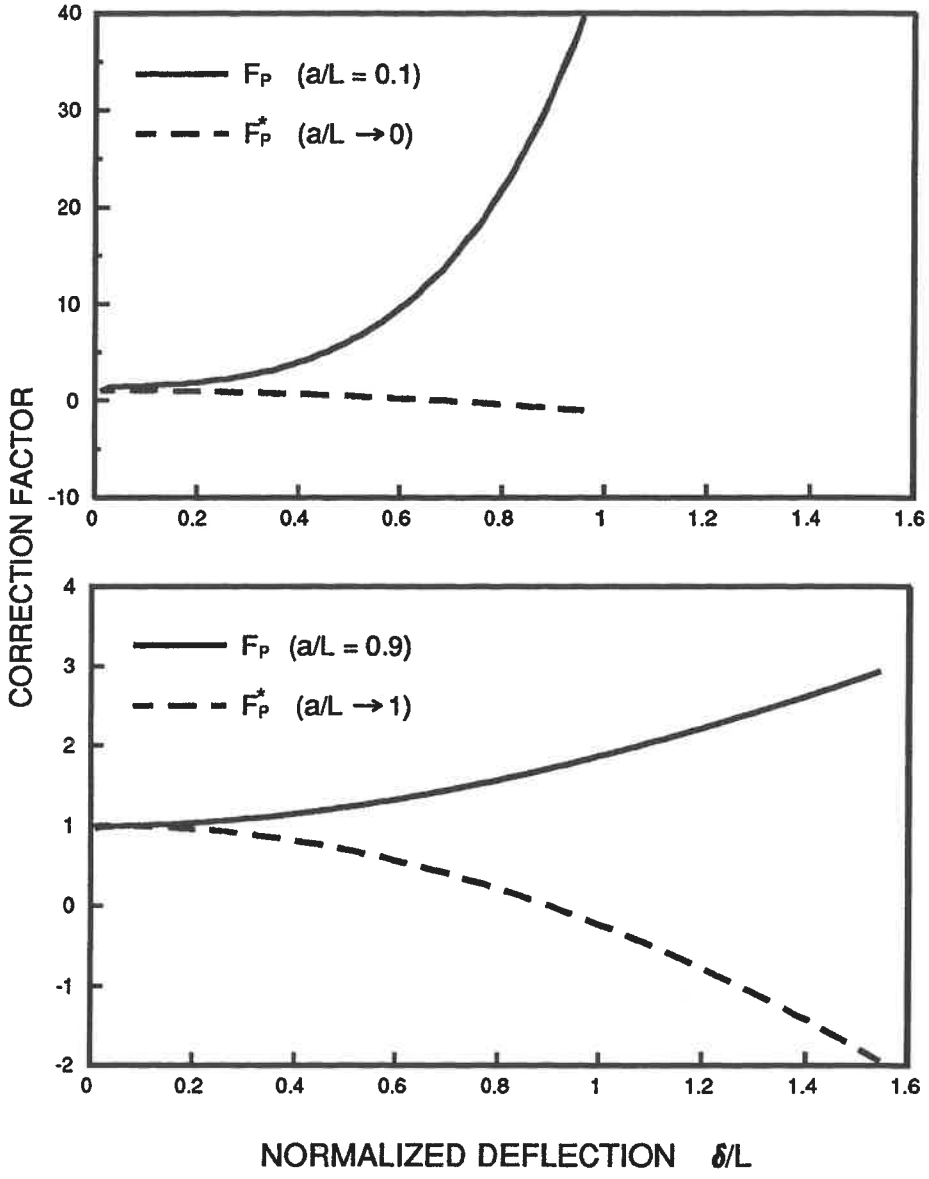

Figure A.9 Comparison of large deflection correction factors for strain energy release rate:

F_P for the original ELS specimen (Fig. A.1a);

F_P^* for the modified ELS specimen (Fig. A.1c).

in the tendency of variation suggests that F_p^* cannot be used for the original ELS specimen. The difference may be explained by considering the deformed geometry and the bending moment at the crack tip section. In the modified ELS specimen (Fig. A.1c), the crack-tip moment decreases with deflection because the load was assumed to be constant in (98, 100) while the horizontal distance between the load line and the crack tip reduces as the sample deflects. In the original ELS specimen, on the contrary, the bending moment increases with deflection as shown in Fig. A.4.

A.6 Fracture Stability

Fracture stability may be approximately estimated by examining the variation of strain energy release rate over crack length (98). The fracture may be unstable (stable) if G_{II} increases (decreases) with the crack growth. For the ELS specimen in the displacement controlled test condition (Fig. A.1a), analysis by linear beam theory indicates that the fracture is stable when $a/L > 0.55$ and is unstable at a shorter crack length. In large deflection situations, the G_{II} variation over crack length is shown in Fig. A.10. As compared to that predicted by linear beam theory, the crack stability depends not only on the crack length but also on deflection of the sample. The large deflection effect tends to result in stable fracture at a crack length shorter than $a/L = 0.55$. This effect has been observed in Chapter 8 in testing the APC-2 composite.

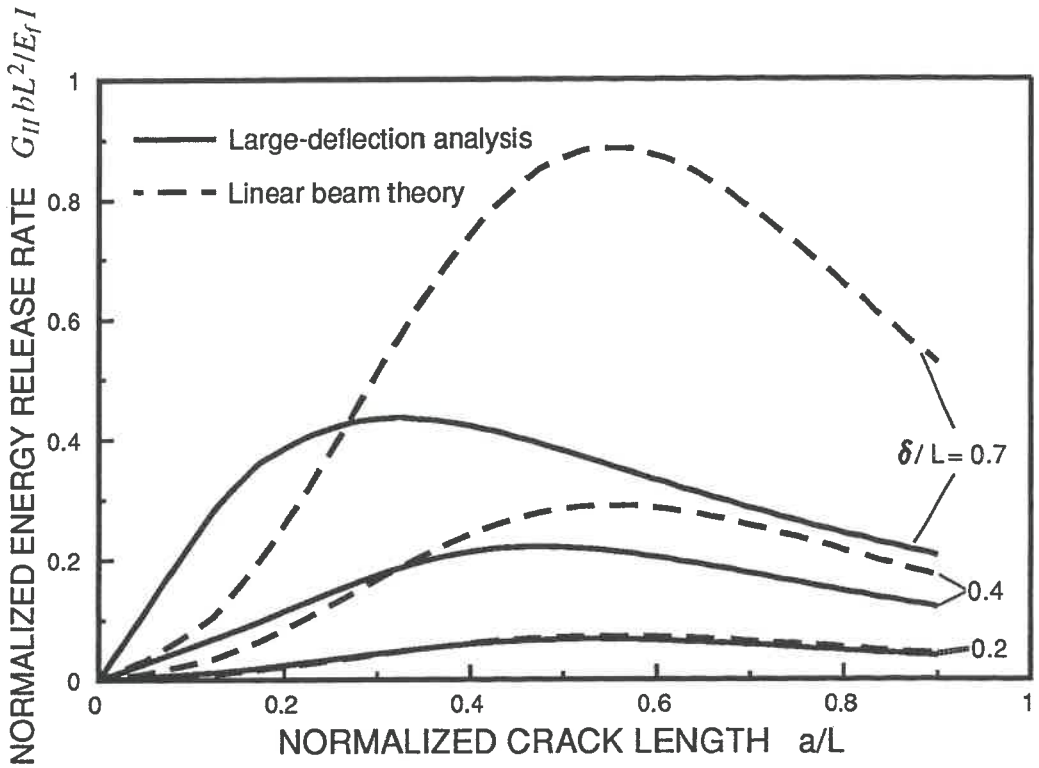

Figure A.10 Variation of strain energy release rate as a function of crack extension in ELS specimen at a given deflection: comparison between linear and non-linear beam theories.

Appendix B

Large Deflection Correction Factors for End-Loaded-Split Fracture Test

$a/L = 0.1$

α (deg.)	α_1 (deg.)	$\bar{\delta}$ ($\bar{\delta} = \delta/a$)	$\bar{P}$ ($\bar{P} = PL^2/E_f I$)	F_P	F_δ
10	9.56	1.1350	0.3345	1.466	1.424
20	18.76	2.2710	0.6326	2.002	1.737
30	27.19	3.4020	0.8663	3.023	2.191
40	34.37	4.5180	1.0230	4.904	2.812
50	39.90	5.6060	1.1070	8.033	3.499
60	43.52	6.6590	1.1290	12.720	4.090
70	45.04	7.6720	1.1050	19.230	4.460
80	44.34	8.6420	1.0450	28.150	4.597
90	41.34	9.5870	0.9516	39.610	4.362

$a/L = 0.2$

α (deg.)	α_1 (deg.)	$\bar{\delta}$ ($\bar{\delta} = \delta/a$)	$\bar{P}$ ($\bar{P} = PL^2/E_f I$)	F_P	F_δ
10	8.50	0.5316	0.3064	1.0690	1.0340
20	16.56	1.0610	0.5805	1.3030	1.1350
30	23.78	1.5870	0.7984	1.7020	1.2550
40	29.77	2.1070	0.9488	2.3640	1.3960
50	34.22	2.6200	1.0320	3.3060	1.4940
60	36.91	3.1270	1.0550	4.6580	1.5440
70	37.66	3.6320	1.0260	6.5340	1.5200
80	36.36	4.1480	0.9528	9.0690	1.3940
90	33.01	4.7120	0.8360	12.5500	1.1510

$a/L = 0.3$

α (deg.)	α_1 (deg.)	$\bar{\delta}$ ($\bar{\delta} = \delta/a$)	$\bar{P}$ ($\bar{P} = PL^2/E_f I$)	F_P	F_δ
10	7.10	0.3301	0.2704	1.0460	1.0140
20	13.79	0.6598	0.5146	1.1760	1.0320
30	19.71	0.9893	0.7120	1.4040	1.0490
40	24.53	1.3190	0.8510	1.7520	1.0510
50	27.99	1.6520	0.9284	2.2550	1.0280
60	29.87	1.9910	0.9467	2.9560	0.9643
70	30.05	2.3460	0.9106	3.9240	0.8531
80	28.50	2.7370	0.8251	5.2660	0.6904
90	25.35	3.2100	0.6949	7.2180	0.4880

$a/L = 0.4$

α (deg.)	α_1 (deg.)	$\bar{\delta}$ ($\bar{\delta} = \delta/a$)	$\bar{P}$ ($\bar{P} = PL^2/E_f I$)	F_p	F_δ
10	5.62	0.2344	0.2323	1.0310	0.9990
20	10.90	0.4700	0.4436	1.1200	0.9844
30	15.54	0.7081	0.6163	1.2720	0.9505
40	19.25	0.9510	0.7389	1.5040	0.8961
50	21.82	1.2020	0.8060	1.8340	0.8131
60	23.09	1.4690	0.8170	2.2990	0.7018
70	22.98	1.7630	0.7752	2.9470	0.5624
80	21.54	2.1070	0.6865	3.8760	0.4061
90	18.96	2.5470	0.5601	5.2660	0.2512

$a/L = 0.5$

α (deg.)	α_1 (deg.)	$\bar{\delta}$ ($\bar{\delta} = \delta/a$)	$\bar{P}$ ($\bar{P} = PL^2/E_f I$)	F_p	F_δ
10	4.24	0.1832	0.1966	1.0230	0.9896
20	8.22	0.3684	0.3759	1.0880	0.9516
30	11.69	0.5580	0.5230	1.2010	0.8868
40	14.43	0.7553	0.6272	1.3750	0.7968
50	16.28	0.9653	0.6823	1.6260	0.6825
60	17.13	1.1960	0.6870	1.9760	0.5481
70	16.95	1.4600	0.6443	2.4740	0.4049
80	15.82	1.7810	0.5612	3.1980	0.2669
90	13.89	2.2010	0.4490	4.3130	0.1508

$a/L = 0.6$

α (deg.)	α_1 (deg.)	$\bar{\delta}$ ($\bar{\delta} = \delta/a$)	$\bar{P}$ ($\bar{P} = PL^2/E_f I$)	F_p	F_δ
10	3.04	0.1541	0.1654	1.0140	0.9797
20	5.89	0.3108	0.3163	1.0680	0.9275
30	8.37	0.4731	0.4400	1.1600	0.8414
40	10.31	0.6450	0.5269	1.3020	0.7284
50	11.60	0.8319	0.5713	1.5040	0.5949
60	12.17	1.0420	0.5720	1.7920	0.4524
70	12.03	1.2890	0.5321	2.2030	0.3147
80	11.23	1.5950	0.4589	2.8110	0.1951
90	9.88	1.9990	0.3632	3.7570	0.1040

$a/L = 0.7$

α (deg.)	α_1 (deg.)	$\bar{\delta}$ ($\bar{\delta} = \delta/a$)	$\bar{P}$ ($\bar{P} = PL^2/E_f I$)	F_p	F_δ
10	2.04	0.1370	0.1392	1.0080	0.9720
20	3.95	0.2770	0.2662	1.0540	0.9086
30	5.61	0.4233	0.3700	1.1330	0.8077
40	6.90	0.5802	0.4423	1.2530	0.6796
50	7.77	0.7533	0.4782	1.4270	0.5367
60	8.16	0.9509	0.4769	1.6740	0.3930
70	8.07	1.1860	0.4414	2.0290	0.2624
80	7.55	1.4800	0.3786	2.5590	0.1564
90	6.67	1.8690	0.2981	3.3920	0.0805

$a/L = 0.8$

α (deg.)	α_1 (deg.)	$\bar{\delta}$ ($\bar{\delta} = \delta/a$)	$\bar{P}$ ($\bar{P} = PL^2/E_f I$)	F_p	F_δ
10	1.22	0.1268	0.1178	1.0030	0.9660
20	2.36	0.2568	0.2250	1.0440	0.8948
30	3.35	0.3934	0.3125	1.1130	0.7841
40	4.13	0.5409	0.3730	1.2180	0.6469
50	4.65	0.7050	0.4025	1.3710	0.4991
60	4.89	0.8940	0.4005	1.5900	0.3562
70	4.86	1.1200	0.3697	1.9070	0.2320
80	4.56	1.4040	0.3162	2.3820	0.1349
90	4.05	1.7810	0.2483	3.1300	0.0680

$a/L = 0.9$

α (deg.)	α_1 (deg.)	$\bar{\delta}$ ($\bar{\delta} = \delta/a$)	$\bar{P}$ ($\bar{P} = PL^2/E_f I$)	F_p	F_δ
10	0.55	0.1206	0.1003	1.0000	0.9626
20	1.06	0.2444	0.1915	1.0360	0.8861
30	1.51	0.3749	0.2658	1.0980	0.7686
40	1.86	0.5163	0.3170	1.1920	0.6263
50	2.10	0.6742	0.3418	1.3300	0.4762
60	2.22	0.8567	0.3396	1.5280	0.3345
70	2.21	1.0760	0.3132	1.8160	0.2144
80	2.09	1.3510	0.2675	2.2460	0.1227
90	1.86	1.7170	0.2098	2.9320	0.0611